

2017

## Interactions of Buoyant Upwellings with Subduction Induced Mantle Wedge Flow

Richard Tucker Sylvia  
*University of Rhode Island*, [proception@uri.edu](mailto:proception@uri.edu)

Follow this and additional works at: <https://digitalcommons.uri.edu/theses>

---

### Recommended Citation

Sylvia, Richard Tucker, "Interactions of Buoyant Upwellings with Subduction Induced Mantle Wedge Flow" (2017). *Open Access Master's Theses*. Paper 1146.  
<https://digitalcommons.uri.edu/theses/1146>

This Thesis is brought to you by the University of Rhode Island. It has been accepted for inclusion in Open Access Master's Theses by an authorized administrator of DigitalCommons@URI. For more information, please contact [digitalcommons-group@uri.edu](mailto:digitalcommons-group@uri.edu). For permission to reuse copyrighted content, contact the author directly.

INTERACTIONS OF BUOYANT UPWELLINGS WITH  
SUBDUCTION INDUCED MANTLE WEDGE FLOW

BY

R. TUCKER SYLVIA

A THESIS SUBMITTED IN PARTIAL FULFILLMENT OF THE  
REQUIREMENTS FOR THE DEGREE OF

MASTER OF SCIENCE

IN

OCEANOGRAPHY

UNIVERSITY OF RHODE ISLAND

2017

MASTER OF SCIENCE THESIS

OF

R. TUCKER SYLVIA

APPROVED:

Thesis Committee:

Major Professor      Chris Kincaid

Steve Carey

Dawn Cardace

Nasser H. Zawia  
DEAN OF THE GRADUATE SCHOOL

UNIVERSITY OF RHODE ISLAND  
2017

## ABSTRACT

One of the primary modes of thermal-chemical transport in subduction zones controlling the growth of crust and the evolution of ocean-atmosphere system through geologic time is buoyant upwellings or diapirs. Typical process models developed from surface data depict vertical ascent paths in two-dimensional cross-sections through convergent margins. In this investigation we show that compositionally buoyant diapirs sourced from the slab-wedge interface have significantly more complex communication pathways as they interact with three-dimensional, time-varying mantle circulation driven by plates. Analogue fluid dynamical laboratory experiments, capable of representing the needed range in length scales ( $10^6$  orders of magnitude), are used to characterize diapir dynamics for a range in plate-driven and buoyancy-driven parameters. Circulation patterns are recorded in traditional cross-sectional and map-view planes using photogrammetry to measure deflections from vertical ascent and parallel to the strike of the trench imposed by the creeping wedge flow. Results show a) the style of plate subduction produces different diapir paths, with spatial-temporal complexity (95% non-vertical paths) b) up-slab and down-slab buoyancy fluxes lead to three basic surfacing modes in arcs and c) three-dimensionality of subduction-driven wedge flow, specifically trench-parallel motion, leads to complex diapir-conduit interaction scenarios, with strong implications for geochemical models of arc volcanics. Diapir thermal models produce a complex range of evolution scenarios, from no-melt, to partial-melt and to full-melt outcomes depending on individual paths.

## ACKNOWLEDGMENTS

I would first like to thank my advisor, Dr. Christopher Kincaid, for his unwavering support throughout my time at the University of Rhode Island and Graduate School of Oceanography. Without his interest in supporting students from diverse educational backgrounds I would never have even applied for a research based graduate degree program. His patient guidance led me through more than three great years of intense and unfettered learning for which I am forever grateful. His passion and excitement for exploring various problems at all scales using a myriad of complimentary techniques (the three legged stool) is truly inspiring for researchers and students alike. Thank you Chris, I really appreciate it.

I would also like to thank my thesis committee members, Dr. Steven Carey and Dr. Dawn Cardace, whose suggestions and insight helped steer this project from inception and significantly increased the soundness and quality of the work.

Additionally I would like to acknowledge my lab mates: Sara Szwaja, Christina Wertman, Kevin Rosa, and Loes van Dam, for countless discussions, suggestions, and sanity checks. Conversations with Rob Pockalny, Brian Savage, Aaron Hirsch and WHOI collaborators Mark Behn and Nan Zhang greatly influenced the outcome of this work.

Finally I must express the utmost thanks and appreciation to my friends and family, especially Mackenzie for sticking with me and seeing this through to the end.

## **PREFACE**

This thesis is presented in the manuscript style in accordance with the University of Rhode Island thesis preparation guidelines. The manuscript is intended to be submitted to *Geophysical Journal International*. Preliminary versions of this work have been presented in poster format at the AGU Fall Meeting 2014, an invited oral presentation at the AGU Fall Meeting 2015, and an oral presentation at the AGU Fall Meeting 2016. This work was funded in part by the National Science Foundation, Grant # EAR-1316310.

## TABLE OF CONTENTS

<b>ABSTRACT.....</b>	<b>ii</b>
<b>ACKNOWLEDGMENTS.....</b>	<b>iii</b>
<b>PREFACE.....</b>	<b>iv</b>
<b>TABLE OF CONTENTS.....</b>	<b>v</b>
<b>LIST OF TABLES.....</b>	<b>vi</b>
<b>LIST OF FIGURES.....</b>	<b>vii</b>
<b>MANUSCRIPT .....</b>	<b>1</b>
INTRODUCTION.....	2
METHODS.....	7
RESULTS.....	15
IMPLICATIONS.....	32
CONCLUSIONS.....	37
REFERENCES.....	40
<b>APPENDICES.....</b>	<b>76</b>

## LIST OF TABLES

TABLE	PAGE
Table 1. Listing of experimental parameters.....	74
Table 2. Summary of measured experimental outcomes .....	75

## LIST OF FIGURES

FIGURE	PAGE
<p>Figure 1. a) Photograph of laboratory setup. The tank sits on a table with the subduction apparatus fully submerged within the analogue working fluid. The subduction apparatus and camera systems translate together along the migration superstructure. b) Oblique view of the region of interest (ROI) showing fluid surface relative to the subduction apparatus, trench, and slab segments. <math>U_t</math> is trench migration vector and <math>U_d</math> is down-dip convergence vector. Cartesian coordinate axes denoted in bottom left.....</p>	45
<p>Figure 2. a) Annotated top-view from a rigid sphere experiment showing initial distribution of diapirs at depth embedded in viscous boundary layer of slab-wedge interface (SWI). <math>U_d</math> is down-dip convergence vector. Coordinate axes in bottom left. b) Annotated side-view from a dry ethanol experiment taken from the south looking north through the ROI. Diapirs and tails highlighted. Injection point sources is at <math>\sim 100</math> km depth. Coordinate axes in bottom left.....</p>	46
<p>Figure 3. a) Simplified schematic diagram of the subduction apparatus ROI. Trench migration and convergence vectors are indicated by <math>U_t</math> and <math>U_d</math> respectively. Curved arrows are simplified representations of major modes of flow, corner flow forced by viscous coupling of the analogue fluid to the slab surface and a toroidal flow component forced by trench migration. b) Free-body diagram of forces acting upon a diapir. Drag force is dashed because it is variable in both magnitude and direction, while buoyancy force maintains vertical orientation. ....</p>	47

Figure 4. Ideal Stoke's terminal ascent velocity curves for the buoyant diapir fluids utilized in this study and single markers for rigid spheres tested. Largest diapirs observed experimentally had radii of approximately 1 cm. Range of free ascent velocities shown are on same order as convergence and migration velocities tested, meaning none are negligible and strong interaction is expected. ....48

Figure 5. Side-view long exposure image showing flow stream lines in cross section. Long white features are finite-strain markers (whiskers) that align with flow. ....49

Figure 6. Side-view plot from Szwaja, 2015 showing velocity magnitude of Lagrangian parcels moving into the shallow wedge and downward above subducting plate with rollback. Velocity magnitude (UM) (color bar) is given as a dimensionless percentage of the downdip plate speed (UD). Warmer colors show the velocity boundary layer (VBL) above the slab into which diapir material is released. Diapirs encounter three flow regimes: 1: The rapid downward VBL, 2: Sluggish descending flow through central wedge, 3: Intermediate speed flow towards the sub-arc and trench. Shallow flow rate varies between 30-50% of UD depending on diapir release/source location above slab (e.g., Figure 9). Hypothetical fluid diapir shown in red being drawn down within VBL. ....50

Figure 7. Cross section of average velocity magnitude with streamlines plotted for experiment ED\_7. In the time averaged flow vertical perturbations from diapir ascent are eliminated and the flow resembles the sparsely measured standard corner flow reported by previous authors. ....51

Figure 8. Top-view faux long-exposure image produced by image stacking and averaging across ~15 frames. Streamlines show material being drawn inward from the

sides toward the slab centerline. The saddle point with no apparent motion relative to the trench is very clear at the right of the image (star shape). This point migrates with the trench and demonstrates why frame of reference is so important when considering rollback style subduction. Material that appears to be translating to the left is actually still moving to the right slower than the trench migration rate.....52

Figure 9. Map-view plot from MacDougall et al., 2014 showing velocity magnitude of Lagrangian parcels moving in the shallow wedge for the same belt drive subduction apparatus for a case of simple downdip-only subduction (50° dip). The trench location is represented with black triangles. Velocity magnitude (color bar) is given as a dimensionless percentage of the downdip plate speed. Zones are marked that highlight spatial variability in source regions supplying sub-arc region of subduction zone.....53

Figure 10. Map-view plot from Szwaja, 2015 showing velocity magnitude of Lagrangian parcels moving in the shallow wedge for the same belt drive subduction apparatus for a case of rollback subduction. The trench location is represented with black triangles. Velocity magnitude (UM) (colorbar) is given as a dimensionless percentage of the downdip plate speed (UD). Plots show how toroidal flow around retreating slab brings material along trench-parallel paths towards the wedge centerline far from the trench, before turning trench-normal. Shallow flow to the sub-arc is along curved paths, roughly similar to downdip only cases. Diapirs rising from different parts of the slab will experience different shallow return flow speeds and magnitudes (highlighted by hypothetical red diapirs). .....54

Figure 11. Map-view (a-d) and side-view (e-h) images of rigid diapirs (Case D\_15,

Tables 1, 2) rising into the most simple plate-flow scenario, or downdip-only slab motion. a) and e): Initial conditions for two rows of 6 diapirs distributed in a trench-parallel orientation within the velocity boundary layer (VBL) above the sinking plate. The use of two rows roughly represents the buoyancy input proposed for different fluid-release mineral phase changes, a sub-arc and a rear-arc output (Ringwood, 1982). Red circles in frames b-d, f-h highlight surfacing diapirs and locations of expected melt delivery to the base of the plate. Near-surface, plate-driven 3-D return flow towards the trench has a significant trench-parallel component, producing a clump of diapirs in the central 3<sup>rd</sup> of trench, in the sub-arc region. The second rank of diapirs surfaces in the back-arc, as an arcuate shaped, trench-parallel feature. Trench location indicated by white triangles in upper panels. ....55

Figure 12. Map-view (a-d) and side-view (e-h) images of rigid diapirs (Case D\_17, Tables 1,2) rising into a mantle wedge flow responding to rollback subduction.

Circulation now involves toroidal flow around the slab, from the ocean-side to wedge-side of the system (left to right). a) and e): Initial conditions for three rows of diapirs distributed in a trench-parallel orientation, in the velocity boundary layer above the sinking plate. Red circles in frames b-d, f-h highlight surfacing diapirs and locations of expected melt delivery to the base of the plate. Sub-arc patterns are similar to downdip-only cases, whereas rollback flow delivers rising diapirs towards the central, symmetry axis of the wedge. Surface melt delivery is linear in a trench-normal orientation near the end of the experiment (d and h). ....56

Figure 13. Sequence of map-view images from an experiment with downdip subduction with a gap between slab segments of 55° dip (left belt) and 45° (right belt)

(Case D\_10, Tables 1,2) . a) The initial placement of rigid sphere diapirs is shown, where 4 diapirs are distributed in a trench-parallel orientation along each slab segment. As in prior cases, diapirs are initially placed in the VBL above the subducting plate. Colored circles are used to construct distinct diapir pathlines for those initiating above the steep belt (b) and shallow belt (c). (b) Patterns clearly show that flow/diapir transport is from the deep wedge above the steep slab segment to the sub-arc region above the inner edge of the shallow slab segment. c) Without rollback, diapirs sourced from the shallower slab also return to the sub-arc of this plate through curved ascent paths (1. slightly up and away from the trench, 2. near-vertical through mid-wedge, 3. strongly deflected sub-horizontal and toward the trench in shallow wedge). Grey shaded circles represent starting points along diapir particle paths. Trench location represented with white triangles. Frame numbers noted are 0, 20, 40, 60, and 80 corresponding to times of 0, 7.7, 15.5, 23.2, and 30.9 Myr respectively.....57

Figure 14. Map-view images from experiment D\_22 including rollback subduction, a no-slip surface under the back-arc plate, and a gap between slab segments of 55° dip (left belt) and 40° (right belt). a) The initial placement of rigid sphere diapirs distributed in two rows in a trench-parallel orientation along each slab segment. (b) Patterns showing extreme trench-parallel focusing of steep plate diapirs toward the sub-arc region of the shallower plate. Start locations shown as shaded circles. Sense of strong trench-parallel flow is highlighted with gray arrow. c) With rollback, diapirs from the shallow slab are left behind by migrating trench/slab, and combine with toroidal flow to surface in a linear (trench-normal) pattern. Trench location represented with white triangles. Black line with white dashes shows location of

back-arc ridge where Mylar is laid down at the trench migration rate to create a no-slip condition on horizontal surface velocity (on plot, region below the line, or beneath the back-arc section of plate). Frame numbers referenced are 0, 20, 40, 56 corresponding to times of 0, 7.5, 14.9, 20.9 Myr respectively.....58

Figure 15. Cross-sectional image through wedge for case E\_13, with downdip-only subduction and diapirs of (dry) ethanol. a) (time 10 Myr) This frame shows typical examples of distinct diapirs evolving within the velocity boundary layer (VBL) above the slab. A single buoyancy source feeds a growing diapir head as it moves down-slab, trailing a narrow conduit structure that connects back to the source. b) (time 15.8 Myr) The diapirs exit the VBL and rise upward through the sluggish mid-wedge, along arcuate paths (first away from the trench, and then back towards the trench). Conduits trail behind the diapirs and can (1) be long and distended, (2) remain connected to the source or (3) be short and severed. c) (time 20 Myr) Despite constant buoyancy flux and simple downdip-only subduction, three different paths occur, with three different trench-normal surfacing distances ranging from sub-arc (blue triangle) to back-arc (red triangle). .....59

Figure 16. Similar cross-sectional image through wedge as Figure 15, but for case E\_14, with rollback subduction and diapirs of (dry) ethanol. a) Frame shows a diapir that has risen from VBL into the mid-wedge, with a trailing conduit that has severed from source region and two smaller unsuccessful diapirs being entrained out of the ROI. b) As the diapir rises through the mid-wedge, the tail is drawn downward with background flow and is severed from the source. c) The diapir head impacts the base of plate at an intermediate trench-normal distance. Times are a) 12.8 Myr, b) 16 Myr,

c) 17.9 Myr. ....60

Figure 17. a) Cross-section through wedge for case E\_7 (ethanol-dry diapir, downdip-only slab, 45° dip, 1 diapir source). Lines marked by colored circles show digitized paths of diapirs sourced from the same location. Paths highlight the extreme range in path shapes/lengths through the wedge (heating) and surfacing locations (volcanic output), discussed as three ascent modes (I, II, III). b) Green paths represent spaced out diapirs lacking interaction with other buoyancy sources in the VBL or central wedge (Mode I). These intermediate surfacing locations range are ~350 km from trench. Mode II (blue) and Mode III type diapir paths are shown in subsequent figures.....61

Figure 18. Cross-sections with diapir paths for case E\_7 as in Figure 14. (ethanol-dry diapir, downdip-only slab, 45° dip, 1 diapir source) highlighting a second mode of evolution/ascent. Paths are shown in blue for three distinct Mode II diapirs. These upwellings have received buoyant fluid from both up-slab and down-slab conduits while in the VBL, achieving a larger volume and rise velocity. Surfacing locations are ~150 km closer to the trench than Mode I (green paths shown for reference). A remnant down-slab conduit is seen as a bright tail in (b), trailing the second high volume (Mode II) diapir to surface in this E7 experiment.....62

Figure 19. Cross-section through wedge for case E7 as in figures 17 and 18 highlighting the third mode of diapir interaction/ascent from slab to surface (shown as red circle paths). a) A repeatable pattern in these cases is that small diapirs separate more slowly from the VBL, and are dragged deeper into the system. Single diapirs stall here, where upward buoyancy balances downward drag. b) Accumulated

smaller diapirs rise together at a greater ascent rate, along nearly vertical paths. c) Diapir clumps surface at the greatest distance from the trench, ~75 km further from the trench than reference (green Mode I) non-interacting diapirs. d) An interesting (repeatable) result is that inner diapirs in the clump can be delayed in surfacing (yellow path) by being held beneath their partners. ....63

Figure 20. Map-view images from experiment V\_7 (downdip-only subduction), using vodka as the diapir fluid, that allows for merging of distinct flow structures. Four diapir sources are modeled, with identical constant buoyancy fluxes, and are labeled in panel (a) (1: mid-slab – 4. slab-edge). Frames cropped to focus on the southern slab segment. a) In 3-D experiment, even simple downdip-only subduction generates wedge flow (above the VBL) with a trench-parallel component that carries material from the slab edge towards the wedge centerline (see Figure 9). b) Diapirs moving in the trench-parallel direction interact with new buoyancy sources. c) In the 5 second (167 kyr) interval between frames the deeper diapir from source 4 merges upward into the shallower diapir from source 3. Volume and rise rate increase markedly and ascent becomes near vertical.....64

Figure 21. Map-view images from experiment V\_7 (downdip-only subduction), using vodka as the diapir fluid, that allows for merging of distinct flow structures. a) Trench-parallel drift of diapirs from different source locations produces a vertically aligned column of diapirs originating from three different source locations. b) In the 5 seconds (167 kyr) between images, the deepest diapir from source 4 has merged upwards into the mid-level diapir from source 3. c) In the 5 second (167 kyr) interval between subsequent frames the newly enlarged combined mid-level diapir accelerates

and merges upward into the diapir from source 2 making one high-volume near-surface diapir containing material from sources 4, 3, and 2.....65

Figure 22. Side-view, trench-normal cross-sections through the wedge for experiment V\_7 (downdip subduction, 4 vodka sources). a) Three distinct diapirs have moved into the mid-wedge, where they drift with a trench-parallel component of motion (into the page). b) One time-step later a deeper diapir from a different source is moving upward and into the page through the tail of the overriding diapir. c) Five seconds further in time the two diapirs have fully merged.....66

Figure 23. Side-view, trench-normal cross-sections through the wedge for experiment V\_7 (downdip subduction, 4 vodka sources). a) An array of diapirs are evolving at different trench-parallel locations (into the page). b) Deep diapir fluid encounters a conduit structure and begins rapid ascent. c) Five seconds ( 167 kyr) further in experiment time, the deeper is merging upward into the shallower diapir originating from one source closer to the centerline. c) After another five second (167 kyr) time-step, the newly merged diapir is beginning to merge upwards into the stalled diapir above. The deeper diapir fluid from (b) transits ~200km in 0.4 Ma, 12 seconds of lab time, yielding an average rise rate of 50 km / 100 kyr.....67

Figure 24. Map-view images from experiment V\_9 (downdip subduction, 35° dip, 4 vodka diapir fluid sources, fixed upper surface). a) Dramatic example of rapid vertical transport due to 3-D vertical shear in wedge combining with vertically rising diapirs to produce vertical columns of buoyant morphologies that are able to merge and nearly connect source to surface. Here fluid at the base of the wedge in the VBL is feeling diapirs passing overhead and about to merge upwards. b) In 25 seconds of

elapsed experiment time (1.7 Myr), the fluid from all depths in the wedge is merged into a near-surface patch of diapir fluid trapped beneath the overriding plate.....68

Figure 25. Map-view images from experiment V\_8 (rollback subduction, 35° dip, 4 vodka diapir fluid sources, free surface boundary). The interaction scenarios are a complex balance of downward entrainment in the VBL and advection with the slab, vertical rise due to buoyancy flux and trench-parallel drift due to three-dimensionality of mid- to shallow-wedge return flow towards the sub-arc wedge apex and slab centerline. a) The middle of the three established diapirs is still connected to source 1, growing and taking in fluid from below. b-c) Three distinct diapirs are fully detached from their respective sources and are advected towards the wedge apex without further interacting with deeper diapir fluid. ....69

Figure 26. Side-view, trench-normal cross-sections through the wedge for experiment V\_8 (rollback subduction, 4 vodka sources, free surface). Example of shallower diapir moving with strong trench-parallel motion and interacting with multiple, deeper diapirs arrayed along-strike. a) Mid-level diapir (outlined) is moving into page. b) (15 seconds elapsed from frame a) Deeper, growing diapir in VBL moves rapidly upward into overlying diapir. c) (15 seconds elapsed from frame b) The mid-level feature has moved in a trench-parallel direction over the next deep growing diapir (outlined). d) (5 seconds elapsed from frame c) Deeper buoyant fluid has begun rapid upward assimilation into overlying feature. e) Large volume diapir is impacting underside of plate after accumulating deep fluid from multiple sources in ~200 km of along-trench motion. ....70

Figure 27. Side-view, trench-normal cross-sections through the wedge for experiment

V\_10 (rollback subduction, 4 vodka sources, no-slip overriding, back-arc plate). a) An array of diapirs are evolving at different trench-parallel locations. The presence of a no-slip condition under the back-arc plate causes return flow pathways to deepen in the wedge. b-c) Deep diapir fluid encounters a conduit structure and begins ascent, assimilating into overlying diapir. d) The large volume diapir develops a larger ascent velocity. An enhanced trailing conduit provides a drifting pathway for much deeper fluid to ascend to the surface rapidly (~200 km in ~0.3 Ma (5-10 seconds)).....71

Figure 28. Multiple still frames from experiment D\_14, left panels are top view and right panels are side view. The diapir highlighted in magenta moved very slowly during this part of the experiment translating and rising only ~100 km over 15.3 Myr shown here, while its neighbors highlighted in blue and orange were advected much farther. This is because of the interaction of the magenta diapir and the pocket of material being extruded from between the opening slab tear (white dashed region). 72

Figure 29. Map-view plot of along-strike transport paths and diapir positions relative to the trench. Markers are colored and sized by time. Spacing between markers is indicative of translational velocity (farther = faster). Black stars mark initial positions of rigid spheres at the slab-wedge interface, cyan stars mark position halfway along path, and red stars indicate final surfacing position. Note greater velocities at depth while diapirs are proximal to the kinematic forcing of the slab, and increased along-strike displacements for diapirs originating farther from the slab centerline. 4 diapirs surfaced along the centerline but took very different paths to get there.....73

**MANUSCRIPT**

Interactions of buoyant upwellings with subduction induced mantle wedge flow

By

R. Tucker Sylvia and Christopher Kincaid\*

*Graduate School of Oceanography, University of Rhode Island  
Narragansett, Rhode Island*

A manuscript in preparation for submission to Geophysical Journal International

\*

Corresponding author:  
Christopher Kincaid  
Graduate School of Oceanography  
University of Rhode Island  
215 South Ferry Road  
Narragansett, RI, 02882, USA  
Phone: +1-401-874-6571  
Email: kincaid@uri.edu

## 1. Introduction

Subduction is a primary mechanism of mass and heat transfer between Earth's surface and interior and a major driver of large-scale mantle flow patterns. Subduction also drives processes ranging from planetary resurfacing, the opening and closing of ocean basins, and the differentiation and accretion of continental crust. Tectonics and subduction play key roles in regulating the global carbon cycle and climate on geologic timescales. On shorter timescales, more relevant to humans, subduction is a large concern as it is intimately linked to destructive geologic hazards including large mega-thrust earthquakes, tsunamis, and explosive volcanism [*Stern, 2002; Rosen, 2016*]. Much of the global population is concentrated along the continental margins and consequently in close proximity to subduction zones.

We investigate the interactions that buoyant mantle upwellings have with subduction-induced circulation in the mantle wedge using analogue laboratory models. Here mantle wedge is used to describe the region between the down-going slab and the overriding plate, which itself contains a sub-arc plate (closer to the trench) and a back-arc plate (farther from the trench). This study focuses on the origin of volcanic material in subduction zones, and building improved connections for how material moves from the deep slab-wedge interface (SWI) to beneath both sub-arc and back-arc plates. This work aims to expand on our understanding of where source material for volcanic arc magmas originates, the lengths and shapes of ascent paths, time of ascent, and thermal implications for different ascent paths.

One means of transporting subducted material from the SWI to the lithosphere-asthenosphere boundary (LAB) at depth is buoyant upwelling or diapirism. Diapirism

within the mantle has been proposed for years within the literature, for example [Berner *et al.*, 1972; Whitehead and Luther, 1975; Oxburgh *et al.*, 1978; Marsh, 1979; Olson and Singer, 1985; Olson and Nam, 1986; Weinberg and Podladchikov, 1995; Kelly *et al.*, 1997; Manga, 1997; Hall and Kincaid, 2001; Gerya and Yuen, 2003; Hasenclever *et al.*, 2011; Marschall and Schumacher, 2012; Miller and Behn, 2012], and is an elegant solution encompassing the episodic nature of surface volcanism consistent with the material transport mechanism. The diapir model is a parsimonious answer to the question of how to move relatively large volumes of material around in a complex and dynamic tectonic setting.

The physics of producing diapiric structures is relatively well understood and described analytically by the Rayleigh-Taylor instability and has been investigated experimentally and numerically [Rayleigh, 1882; Nettleton, 1934; Taylor, 1950]. Diapirism culminates with the detachment and subsequent ascent of a buoyant spheroidal body from an unstable fluid interface. Any layered system containing a fluid overlain by another, denser one is unstable. Small perturbations at the material interface between the two fluids result in imperfections and opportunities for the less dense underlying material to grow rapidly and rise through the overburden.

The nature of the density contrast between the two fluids may be thermal, as is the case for classical stove-top or Rayleigh-Benard convection; compositional as is the case for crustal salt diapirism; or a combination of the two such as a “lava lamp”, which may be the most appropriate and accessible analogue available for demonstrating mantle convection processes. In natural subduction zones, the density contrast between buoyant diapir material and ambient mantle wedge asthenosphere

will be both thermal and compositional in nature. In this study we investigate purely compositional density differences.

Buoyant ascent of a diapir through a quiescent homogeneous fluid is vertical if no external forces act upon it as a result of the vertical orientations of the gravitational and buoyancy forces (Figure 3b). The only variable force in this system, both in magnitude and direction, is the viscous drag exhibited on a buoyant parcel within the forced mantle wedge flow. The experiments presented here test for the plausibility of a purely vertical mass transport mechanism of buoyant material sourced near the melt generation region at the SWI to the LAB. In this vertically-connected framework, the volcanic arc is assumed to be positioned directly above the melt generation zone. Melt is proposed to ascend rapidly and vertically, having little interaction with the creeping mantle wedge flow. Many figures or schematic diagrams of the mantle wedge include a depiction of the convecting asthenosphere yet still draw vertical melt pathways [Stern, 2002; Tamura *et al.*, 2011]. For some observations and scales of this vertically connected framework may be a good first order approximation, but for large-scale coherent features like diapirs it is not.

This paper presents the results from a suite of physical tectonic-fluid dynamic analogue laboratory experiments that introduce buoyant material into a kinematically-forced mantle wedge flow field (Figures 2 and 3a). Laboratory models are particularly valuable for the problem of subduction-driven flow interacting with buoyant morphologies in the wedge because the use of a real continuous fluid allows for representing the extreme range in relevant length scales of six orders of magnitude. The prior laboratory modeling work looking at mantle flow – diapir interactions of

Hall and Kincaid (2001) considered a constant buoyancy flux introduced along the centerline or symmetry axis of the subducting plate, but only for the simplest subduction style, or downdip motion of a constant dip slab, and with no consideration for the influence of along-trench, or trench-parallel flow or source locations on ascent trajectories. We expand on the prior work in three important ways: 1) We first limit the inherent complexity of time-continuous source buoyancy flux and diapir morphologies with heads and tails in order to focus on the role of subduction style (downdip and rollback subduction) and along-slab changes in dip (slab gaps or windows) on simple diapirs (no tails, constant buoyancy) sourced from multiple locations along the slab surface (Figure 2a). 2) A second set of experiments builds from Hall and Kincaid (2001) by recreating the continuous buoyancy release along a narrow region above the centerline of the subducting slab, but now including both downdip and rollback modes of subduction (Figure 2b). In these cases we begin with the simplest mode of diapirs with heads and tails by using dry ethanol (described below) that is capable of producing both head and conduit morphologies, but without complex mixing/interaction scenarios between diapirs. 3) A third, and final, set of experiments explores an additional, essential aspect of 3-D subduction. For a similar spectrum of subduction styles, an array of buoyancy sources is spaced in a trench-parallel orientation to show along-trench interactions between background wedge flow and rising diapirs (Figure 20). A wet ethanol solution (vodka), following Hall and Kincaid (2001), is used to allow for diapir-diapir interactions and coalescence by incorporating rheological weakening of the matrix fluid. Our models make use of a subduction apparatus that is well tested, and includes capabilities for both downdip and rollback

subduction styles for a complete range of fixed dip angles [*Kincaid et al.*, 2013; *MacDougall et al.*, 2014; *Szwaja and Kincaid*, 2015]. This apparatus (Figures 1, 2, and 3a) also has the ability to characterize 4-D wedge circulation and related diapir ascent pathways when the geometry of the subduction zone varies through along-trench changes in dip angle producing slab gaps that are fixed or can vary through time.

Our experiments are designed to explore the deflections of diapir paths caused by variations in diapir parameters (buoyancy, morphology, source spatial patterns) and plate-driven background flow regimes (subduction rate, style, geometry). The experiments demonstrate that there is interaction between diapirs and the creeping mantle wedge over this broad parameter space. Downdip subduction, rollback subduction and along-trench dip changes all significantly alter the shapes and timing of diapir ascent pathways. Nearly all pathways are non-vertical, and experiments reveal conditions that favor significant trench-parallel offsets between the diapir source and surfacing locations, adding to the challenge of rectifying geochemical data within a geodynamical framework. Results for cases with diapirs evolving from a continuous source of buoyancy reveal fundamental modes of diapir head/conduit evolution that produce distinct and repeatable trench-normal surfacing locations. Similar experiments with multiple along-trench buoyancy sources highlight the rich complexity of diapir-diapir interactions and ascent trajectories that result from shallower buoyant morphologies drifting over top of the deeper, continuous sources. Results show that diapirs arriving beneath the volcanic arc can be influenced by chemical inputs from multiple locations across the surface of a heterogeneous down-going slab.

## 2. Methods

### 2.1 Tank and Boundary Conditions

Figure 1 depicts the experimental setup used to simulate the ambient mantle in this setting, contained within a large (L:150 [cm] x W:75 [cm] x H:38 [cm] x 1.5 [cm] thick) acrylic tank. The trench normal boundaries (long walls) of the tank are one full slab width (25 [cm]) away from the edge of the region of interest (ROI). This places a far-field no slip condition away from the ROI giving it essentially open boundaries. The end walls are even farther from the mantle wedge ROI.

### 2.2 Ambient Working Fluid and Glucose Rheology

The creeping asthenosphere is modeled using highly viscous (96 wt% solids) glucose syrup as the primary working fluid following similar studies [*Kincaid and Olson, 1987; Bellahsen et al., 2005; Piromallo et al., 2006; Kincaid et al., 2013; Druken et al., 2014; MacDougall et al., 2014; Szwaja and Kincaid, 2015*]. The viscosity of glucose syrup is primarily a function of temperature and water content and follows an Arrhenius type function [*Schellart, 2011*]. Both of these parameters are held constant throughout the duration of a single experiment and between different individual experimental runs. At the small strain rates considered in these experiments any stress dependence of the glucose rheology is considered negligible.

### 2.3 Externally-Forced Kinematic Approach

Flow within the working fluid is induced kinematically through the use of a belt drive system (Figures 1b, 3a). Two continuous rubber belts representing infinitely strong subducting slab segments are driven by high torque variable speed DC electric gear motors. Flow in the wedge is achieved by viscous coupling of the working fluid

to these belts, facilitating the development of a thin viscous velocity boundary layer (VBL) at the SWI. This system has been shown to reproduce mantle wedge flow fields that have been observed in fully dynamic (internally forced) analogue models [Kincaid and Olson, 1987; Richards and Griffiths, 1988; Kincaid and Griffiths, 2003; Funicello et al., 2006; Kincaid et al., 2013; Druken et al., 2014]. The benefit of kinematically prescribing plate rates is an increase in experimental reproducibility, minimizing the variability between identical runs that internally forced dynamic analogue models suffer from.

Given that plate rates are the most well-constrained parameter of the subduction system in comparison with rheology, composition, and structure, an externally-forced kinematic modeling approach is justified. A maximum bound for the amount of energy put into driving this system can be derived from the maximum electrical draw of the drive motors, which is about  $4.6 \times 10^3$  Joules for the duration of a typical experiment.

## **2.4 Degrees of Freedom**

The custom-built subduction apparatus (Figure 1) allows for control of two independent slab segments and their respective convergence rates (downdip motion is referenced by the variable  $U_d$ ). Because the two belts are controlled independently there is an added capability of modeling along-strike dip changes, either fixed or varying over time (i.e. slab steepening or the opening of slab gaps). Deep belt rollers at the equivalent of the upper-lower mantle transition zone (~400 km depth) migrate forward or backward relative to a stationary roller (representing a fixed trench) to produce either slab shallowing or steepening. There is also control for variable trench

migration or rollback speed and position. This becomes important for producing a toroidal flow component around plate edges (Figures 8, 10), significant for trench-parallel material transport along-strike. The upper surface boundary of the overriding plate can be left free, fixed relative to the trench using a small rigid sheet of acrylic, or prescribed kinematically using driven rolls of mylar sheeting to simulate back-arc extension. Experimental parameters for individual experiments are listed in Table 1.

## **2.5 Diapir Materials and Properties**

A variety of materials were tested to model “cold” compositionally buoyant diapirs, see Table 1 for listing of experimental parameters and Table 2 for summary of measured experimental observations. The three distinct sets of experiments discussed above utilize three types of diapir material. The first experiments utilized arrays of solid rigid spheres. Buoyancy of individual diapirs was varied by utilizing various hollow and solid plastics and polystyrene foams ( $100\text{-}500\text{ kg m}^{-3}$ ) in a range of sizes (0.5-1 cm (15-30 km) radius). The primary motivation for this phase was to more fully map flow, especially near plate edges and the boundaries of the ROI, with variable mantle wedge geometries and convergence rates. This phase was also informative in assessing which regions would be conducive to successful diapir formation and detachment in subsequent fluid injection experiments and determining the optimal location for the injection point source. Solid rigid spheres were ideally suited for this phase, minimizing experimental waste before moving to more dynamically-realistic and experimentally-challenging fluid diapirs. These rigid spheres also eliminate the effect of diapir deformation or deviation from spherical shape that malleable fluid diapirs experience.

Regularly spaced arrays of the rigid spheres were embedded in the viscous boundary layer before entering the trench and subducted to diapir initiation and detachment depth (Figure 2a) [Miller and Behn, 2012]. Slab motion was then briefly paused to allow for a small amount of buoyant ascent and detachment of the rigid spheres from the viscous boundary layer at the SWI to initiate before subduction and instantaneous mantle wedge response was continued. Without the brief pause in plate motion rigid spheres remain embedded in the viscous boundary layer and fail to detach from the SWI and are not successful in ascending to the surface. This mapping phase allowed for the examination of the effects of initial position on diapir trajectory and surfacing location as well as determination of where probable diapir initiation and detachment may occur within the tank, as the potential depth range for diapir initiation (30-70 km) and detachment (90-170 km) reported in the literature are not well-constrained [Hall and Kincaid, 2001; Gerya and Yuen, 2003; Miller and Behn, 2012].

In the second and third sets of experiments, diapirs are introduced as buoyant fluid injected continuously from point sources (Figure 2b, 20). Diapir injection is accomplished through the use of syringe pumps with highly precise control of the volumetric flow rate (maximum resolution  $0.2 \text{ microliters hr}^{-1}$ ) exiting a steel tube with internal diameter of  $\sim 0.1 \text{ mm}$  (Figure 2b, 20). Two fluids were utilized in this continuous injection mode: pure anhydrous ethanol (dry), and a hydrous ethanol solution containing 60% water by volume (wet). Cases using ethanol tested the behavior of buoyant fluids released from a single point source located along the slab centerline (Figure 2b).

Anhydrous, 100% pure ethanol was chosen in part because it does not diffuse chemically and is immiscible with the glucose working fluid over experimental laboratory timescales, minimizing contamination of the working fluid. This immiscibility also has important dynamic effects of interest; because the materials do not mix there is no heterogeneity incorporated into the wedge and thus no preferential weak zones or conduit features, such as those reported by Hall and Kincaid (2001), develop. Ethanol is also readily available at low cost with few negative environmental and disposal hazards. The density of pure ethanol is  $789 \text{ kg m}^{-3}$ , resulting in a density contrast within the working fluid of  $-631 \text{ kg m}^{-3}$ , or 44.4%. These ethanol diapirs have a similar ideal Stokes rise velocity as the other materials tested,  $\sim 5.5 \text{ cm min}^{-1}$  for 1 cm radius (Figure 4).

In the third set of experiments a hydrous ethanol solution containing 40% alcohol by volume is used which has a density of  $916 \text{ kg m}^{-3}$ , yielding a density contrast of  $-504 \text{ kg m}^{-3}$ , or 35.5%. This is the closest density contrast to actual mantle values ( $\sim 25\%$  if background mantle density of  $3300 \text{ kg m}^{-3}$  and diapir density of  $2500 \text{ kg m}^{-3}$  are assumed)(Figure 4).

Air was also used, but is not reported here, see Appendix 1. Air in the lab has a density of approximately  $1.180 \text{ kg m}^{-3}$  given a temperature of  $23 \text{ }^\circ\text{C}$ , 25 m elevation above sea level, and 70% relative humidity. The glucose working fluid has a density of  $\sim 1420 \text{ kg m}^{-3}$ , yielding a density contrast of  $-1418.82 \text{ kg m}^{-3}$ , or nearly 100%. This large density contrast was explored as an end member most likely to produce ideal vertical ascent. The calculated ideal terminal Stokes velocity of a spherical air diapir with a 5 mm radius in quiescent fluid is about  $3 \text{ cm min}^{-1}$  (Figure 4).

It is essential that diapir fluid is not able to contaminate the large volume of working glucose fluid, as the changing of such a large volume of highly viscous fluid is a major undertaking. A glucose vacuum system was developed for removing diapir fluid that utilizes a heated wand to precisely remove the lower viscosity material. A procedure was developed whereby all weakened material was removed between experimental runs and the tank and wedge ROI were allowed to homogenize and equilibrate.

Diapirs are tracked throughout an experiment, from introduction until they either successfully surface through the wedge or become entrained deep into the working fluid exiting the ROI. A diapir is deemed successful if it forms, detaches, and transits the entirety of the mantle wedge from the slab-wedge interface to the lithosphere-asthenosphere boundary. Unsuccessful diapirs are therefore those that fail to form, detach, or overcome the advection of the background wedge flow and become entrained in it. We do not report on the fate of unsuccessful diapirs here unless otherwise noted for exceptional results.

## 2.6 Scaling

Scaling between the analogue experiments and the mantle of the Earth is achieved through the dynamical similarity of the Péclet and Prandtl numbers of the two systems [Kincaid and Olson, 1987; Kincaid and Sacks, 1997; Kincaid and Griffiths, 2003; Kincaid et al., 2013; Druken et al., 2014; MacDougall et al., 2014; Szwaja and Kincaid, 2015]. The Péclet number is a dimensionless ratio defined by the relative contributions of advective to diffusive heat transport (eq. 1). The Péclet number of both the laboratory and natural systems is on the order of  $\sim 15$ , suggesting

advection is slightly more important than diffusive heat transport, but the scales of the two competing transport mechanisms are not disparate enough to warrant eliminating either term. The Prandtl number is defined as the ratio of kinematic viscosity to thermal diffusivity (eq 2.), which is very large for both systems, often being approximated as infinite for the mantle. Constant thermal diffusivity is assumed for both systems,  $1 \times 10^{-2}$  and  $1 \times 10^{-3}$  [ $\text{cm}^2 \text{s}^{-1}$ ] for mantle and lab respectively, and all of these experiments are carried out in an isothermal environment with no external heat added. We choose a characteristic length scale of 750 km to equal the total slab width of 25 cm yielding a length scaling factor of  $30 \text{ km cm}^{-1}$ , a time scale factor  $0.5 \text{ min Myr}^{-1}$ , and velocity scale factor of  $1 \text{ cm min}^{-1}$  to  $1.5 \text{ cm yr}^{-1}$ .

$$\text{eq. 1} - Pe = \frac{\text{AdvectiveHeatTransport}}{\text{DiffusiveHeatTransport}} = \frac{U_0 \cdot L}{\kappa}$$

$$\text{eq. 2} - Pr = \frac{\text{ViscousDiffusionRate}}{\text{ThermalDiffusionRate}} = \frac{\nu}{\alpha}$$

<i>Variable</i>	$U_0$	$L$	$\kappa$	$\nu$	$\alpha$
<i>Definition</i>	<i>Characteristic velocity scale</i>	<i>Characteristic length scale</i>	<i>Thermal conductivity</i>	<i>Kinematic viscosity</i>	<i>Thermal diffusivity</i>

## 2.7 Cameras and Image Processing

Time-lapse photography is used to obtain flow field and diapir displacement data via two orthogonally oriented Ultra High Definition (4288 x 2848 pixels) DSLR cameras (Nikon D90). One camera was positioned at the southern wall facing northward through the wedge in a typical vertical cross sectional view with the slab dipping to the east. The second camera was oriented above the center of the trench looking down in map view (Figure 1a). Both cameras were fixed with the trench

always yielding a fixed trench-centric reference frame. These cameras are interfaced through a computer for control and timing, and raw images are immediately archived to disk for later processing and analysis. We shot at a 5 or 10 second frame interval depending on the specific experimental setup.

Basic image processing techniques are used to extract relative motion between frames and diapir transport paths. A custom image processing pipeline was constructed using freely available open source software, namely Python, the SciPy/NumPy stack, and OpenCV. The pipeline consisted of a linear routine of basic operations (color space transform, histogram equalization, background model estimation, blurring, thresholding, segmentation, feature identification, and tracking).

Within the image processing pipeline we also measure other feature descriptors such as diapir radius, eccentricity, major and minor axis azimuth, rotation, Hu moments (scale, rotation, and translation invariants). These additional parameters help in identifying and keeping track of specific diapirs and dealing with occlusion, as well as filtering out misidentified parcels and other noise. This pipeline can be run in batch on all images from a given experiment producing 4D (x,y,z,t) Lagrangian position vectors for diapirs in each frame. Background mantle wedge flow field velocity structure is obtained using common FFT peak shift and interrogation window based DIC/PIV techniques [*Thielicke et al.*, 2010].

### 3. Results

These experiments represent the complex interactions of two distinct mantle processes, background plate-driven circulation and the buoyant ascent of diapir material. For the latter, the ideal Stokes terminal ascent velocity is calculated for each of the diapir analogue materials used (Figure 4). For the rigid spheres it is constant, being set by their unchanging density and radius. For the fluid diapirs we calculate an ideal terminal velocity curve spanning the range of diapir radii observed. The calculated ascent velocities are of similar order of magnitude as the prescribed convergence rates, around  $5 \text{ cm min}^{-1}$ , depicted in Figure 4. Subduction driven flow is the other major factor. Prior studies have utilized this laboratory apparatus to characterize circulation patterns for the most commonly modeled sinking style, purely downdip motion, and for rollback subduction, where the trench and slab migrate laterally towards the ocean side of the system to the west [MacDougall *et al.*, 2014; Szwaja and Kincaid, 2015].

Three basic regimes are relevant to these results in cross-section, 1) rapid downward flow of wedge material directly above the slab (we refer to this as the velocity boundary layer (VBL)), 2) the relatively sluggish interior of the wedge, far from the upper and lower boundaries, and 3) the shallow return flow of wedge material towards the trench and the upper and extreme inner, or apex region of the wedge, (Figures 6, 7). Flow regime 3 is important because it controls how material is brought to and along the underside of the arc/back-arc plates, exerting an influence on thermal-chemical exchange processes from the mantle to the crust.

Prior 4-D subduction laboratory models [Kincaid *et al.*, 2013; MacDougall *et al.*, 2014; Szwaja and Kincaid, 2015] show that downdip and rollback subduction produce very different shallow return flow patterns. Figure 9 shows the direction and magnitude of shallow return flow for a case of downdip only subduction using particle tracks (Lagrangian paths). Material is drawn in towards the central portion of the trench along primarily trench-normal flow lines. Flow at the edges of the trench is oblique, with roughly equal trench-normal and trench-parallel components.

The situation is different for rollback subduction, where lateral motion of the translating slab produces toroidal flow around the plate. Material enters through the wedge side boundaries with strong trench-parallel components of motion (Figures 8, 10). Despite this difference, in closer to the trench, under the arc portion of the overriding plate, the return flow is not markedly dissimilar to the downdip case. Trench-normal trajectories are seen in a more confined zone, or the central 30% of the trench. Away from this region the wedge apex is still supplied by flow that has components of both trench-parallel and trench-normal flow, but with slightly larger trench-parallel component. Flow magnitudes in this region, measured as a percentage of the downdip convergence rate ( $U_d$ ), are  $\sim 0.4 U_d$ . Figures 6 and 7 show representative cross-sectional views of wedge velocity for cases of rollback and downdip-only subduction respectively. The key points are that the largest velocities occur in the velocity boundary layer (VBL, regime 1) where wedge fluid is adhered to and sheared by the down-going slab. Here the flow is similar for both downdip and rollback cases as fluid moves in a strongly trench-normal, plate-parallel (downward) direction at rates that vary from 0.7-1.0  $U_d$ . Regime 2 is the expansive interior region

of the wedge, where flows are generally weak ( $<0.25 U_d$ ) and oriented either towards the trench along trench-normal, trench-oblique or trench-parallel trajectories in the upper portion of the mid-wedge, or weakly downward with the slab in the lower portion of the mid-wedge. The different background flow patterns combine with ascent velocity of the buoyant fluid to determine transport trajectories (times and temperatures) between source and surfacing locations.

### **3.1 4-D Ascent Paths: Simple Diapir Heads vs. Three Subduction Styles**

An array of rigid diapirs (Figure 11), distributed evenly along-strike of the trench and moving into the wedge under the volcanic arc is used to characterize 3-D interaction patterns for buoyant transport and three styles of plate-driven flow (downdip subduction, rollback subduction and along-trench dip changes). Two initial rows of diapirs representing sub-arc and back-arc buoyancy releases, are shown in Figure 11a, for a case of downdip subduction. The diapirs from the shallower of the two rows move upward, out of the VBL and are entrained in the 3-D flow produced by this simplest mode of slab motion through the mantle. Consistent with flow patterns shown in Figure 9, the rigid spheres move along oblique trench-ward paths, surfacing beneath the arc plate in a confined region occupying the central 3<sup>rd</sup> of the modeled trench segment (red circles in Figure 11b, f). The second row of initially deeper rigid diapirs escape the VBL under the back-arc plate and rise to the surface in an arcuate path, bending in towards the trench along the wedge centerline and outwards further from the centerline (Figure 11d, h). This pattern is consistent with shallow circulation at large trench-normal distance in Figure 9, or slightly weaker oblique return flow away from the centerline and slightly stronger trench-normal flow along the

centerline. Rollback subduction produces a similar diapir transport and surfacing pattern for shallower releases rising into the sub-arc wedge (Figure 12). Diapirs from near the slab edges drift inward with a trench-parallel component of motion and surface in the central 3<sup>rd</sup> of the sub-arc wedge. The rise of the deeper diapirs is distinctly different from the downdip only case. Rollback produces a much stronger trench-parallel component of flow further out from the trench (Figures 8, 10) which carries the rising diapirs into a linear surfacing pattern, oriented normal to the trench (Figure 12d). The age progression in the surfacing, and therefore the volcanic output, would be younging to the east, or away from the trench (Figure 12h).

The most dramatic and repeatable diapir transport and surfacing patterns occur when an along-trench change in slab dip angle is modeled (e.g. a slab gap or window). Figures 13 and 14 show such cases, with downdip and rollback subduction, respectively. For the former case, an along-trench distribution of four rigid diapirs above the steeper dipping slab (Figure 13a) is seen to move downwards within the VBL, escape upwards into the mid-wedge before moving efficiently in a shallow return flow oriented from the steep slab wedge towards the sub-arc wedge above the shallow dipping slab (Figure 13b) (shaded circles show starting locations, open circles show locations along the track, circled rigid diapirs show end positions). Interestingly, the diapirs above the shallow dipping slab segment also follow similar curved paths, first descending with the VBL, rising into the mid-wedge and being entrained towards the extreme inner corner of the wedge (or wedge apex) (Figure 13c). Results show these can also surface at different trench-normal distances producing an apparent linear (trench-normal) trend in volcanic output (Figure 29). This pattern of steep deep-

to-shallow dip ascent trajectories and linear surfacing patterns above the shallow dipping segment at greater trench-normal distances is enhanced when a slab window forms in rollback subduction. Figure 14 shows that toroidal flow around the retreating plate results in a much more confined trench-parallel transport of diapirs from steep-dip wedge to shallow dip wedge (Figure 14b). Similarly, the toroidal flow around the retreating shallow slab results in a very pronounced linear distribution of surfacing diapirs, trending along a trench-normal direction (Figures 14c, 29). Interestingly, the surfacing times in this case do not reflect a simple, unidirectional age progression. Diapir surfacing times reflect the more complex deeper interactions with flow resulting in more spatially heterogeneous surface arrival times to the base of the plate.

### **3.2 Source Processes and Diversity of Diapir Ascent Paths**

A second set of experiments utilizes a continuous release of buoyant fluid into the VBL above the down-going slab to develop relationships between processes operating in this source region and the eventual ascent and surfacing patterns for diapirs. We begin simply, following the method of Hall and Kincaid (2001), focusing on release from a single narrow region above the center of subducting slab. This work extends that of Hall and Kincaid (2001) by testing the influence of both downdip and rollback modes of subduction (Figure 2b). Another simplifying factor is the use of a dry ethanol fluid for diapirs. Ethanol and other compositionally dry buoyant diapirs do not exert any rheological weakening on the wedge as they contain no water or heat to alter the matrix viscosity. There is no preferential fabric imprinted in the wedge matrix or weakened conduit features left behind by these dry diapirs that would allow two separate bodies to physically merge into a single morphology [Hall and Kincaid,

2001]. Ethanol therefore makes an excellent next step towards increasing model complexity as the continuous supply of this buoyant fluid can form both diapir heads and conduits that do not merge or change shape. The formation of anhydrous ethanol diapirs begins with the development of a thin tube of fluid drawn axially downward from the injection point source. After detachment of the first diapir in an experiment this material is the severed tail of the previous diapir that has been pinched off at the distal end downward from the source. These thin tubes then fill rapidly and expand outward radially in the convergence normal directions, minimizing their aspect ratio to become spheroidal in shape. The combination of their larger size and smaller density contrast leads to these ethanol diapirs having a similar ideal Stokes rise velocity as the other materials tested ( $5.5 \text{ cm min}^{-1}$  for 1 cm radius, Figure 4). They also exhibit a larger surface area subjected to the viscous drag of the forced wedge flow.

Two experiments (Cases E\_13, E\_14) show typical examples of ethanol diapirs evolving from the VBL along the central section of the descending slab for cases of downward (Figure 15) and rollback (Figure 16) subduction. Beginning diapirs continue to expand as they are drawn downwards, while remaining connected to the buoyancy source through a thin conduit tail structure. Eventually the buoyancy and rise rate of the diapir allow it to escape the relatively rapid speeds in the VBL ( $.7 - 1 U_d$ ) and rise into the more sluggish mid-wedge ( $< 0.25 U_d$ ). Figures 15b and 16b,c show excellent examples of an ascending diapir head with a connected trailing conduit. The conduit becomes severed from the deep source and trails behind the diapir. Often the ethanol conduits are stretched to the breaking point (Figures 15b, 16c ) by competing upward (buoyancy) and downward (drag) forces (Figure 3b). Figure 16 highlights the arcuate

ascent trajectory that is commonly observed, generated by a) rapid downward drag in the VBL away from the trench, b) slow, near-vertical rise into and through the mid-wedge and c) deflection towards a sub-horizontal trajectory during entrainment into return flow towards the trench and base of the sub-arc plate, with different mixes of trench-normal and trench-parallel motion depending on parameters such as subduction mode and geometry (Figures 6,7).

In these along-centerline release cases, the diapir source and surfacing locations are roughly aligned vertically because they remain within the same trench-normal, cross-sectional plane (e.g., limited north-south offsets due to minimal trench-parallel flow). However, a number of key processes can occur at the base of the wedge within the VBL that displace surfacing locations either towards or away from the trench, relative to the deep diapir source region. Figure 17a shows a number of digitized ascent paths for ethanol case E\_7, with shallow downdip subduction. The paths are color coded to reflect the passage of diapirs through cooler and hotter regions of the wedge. They also highlight three distinct modes of source dynamics leading to the different surfacing locations. The reference, or source/ascent Mode I involves evenly spaced diapirs (head and conduit) that separate from the VBL and rise free of any contact or interaction with other buoyancy sources ((Figure 17b, green ascent lines). These paths include greater deflections away from the trench in the VBL than they are returned by the shallow flow, resulting in vertically misaligned source and surfacing locations with a horizontal trench-normal offset of  $\sim 150$ km. A second mode (II), involves over-sized diapirs that develop in the source region due to flow of buoyant material both down-slab through the normal trailing conduit from the

injection source and up-slab from a severed tail (Figure 18). The up-slab flow can occur when an earlier diapir departs and the detached conduit flows up-slab into the next developing diapir (Figure 18a-c). The rapid expansion and departure of a Mode II diapir can also occur due to up-slab flow of another diapir (Figure 15b,c). Here the sudden increase in size/buoyancy causes these diapirs to detach earlier in its formation and surface closest to the trench. A third mode (III), where smaller groups or clusters of diapirs form down-slab to produce an increase in rise rate, is very repeatable in cases both with ethanol and rigid diapirs. Figure 19 illustrates the time evolution of a clump of smaller diapirs. Smaller diapirs have slower ascent rates, remain longer in the VBL and are dragged deeply into the wedge. They tend to separate and stall in the lower, mid-wedge where weaker buoyancy is balanced by weaker downward drag (Figure 19a). Once 2-3 small diapirs enter this region of diapir stagnation, a cluster forms with an integrated buoyancy that significantly exceeds downward drag (Figure 19b). These rapidly rising features, starting from deep in the wedge, produce near-vertical ascent trajectories and surfacing locations that are furthest out from the trench (~540 km) (Figures 17a, 19c).

### **3.3 Trench-parallel Flow and Diapir-Diapir Interactions**

A third set of experiments explores how distributed along-trench buoyancy sources combine with trench-parallel return flow to produce complex diapir-diapir mergers and interactions. An along-trench distribution of diapirs is expected to occur naturally from instabilities arising from the sheet of buoyant material believed to exist above the down-going plate. The work builds from experiments by Hall and Kincaid (2001) that utilized a water-bearing ethanol solution (vodka) that produces rheological

weakening in the wedge, diapir-diapir mixing and networked conduit features in the wedge. This is opposed to rigid spheres or dry ethanol diapirs that cluster, but do not coalesce into a single coherent body. The wet ethanol has a laboratory density contrast that is also closest to mantle values. A hydrous ethanol diapir with 1 cm radius has an ideal Stokes ascent rate in glucose of 4.4 cm/min, neglecting the effect of water on the matrix viscosity (Figure 4). Diapirs of this type tend to exhibit less trench-normal deflection than their dry counterparts because water at the diapir-mantle interface reduces the viscosity at that boundary, consequently reducing the drag by lubricating the surface.

The third experimental phase consisted of adding additional point sources along strike to better mimic a line source. The sources were configured either as a set of three or four sources centered on either the whole plate centerline (E\_13, E\_14, V\_5, V\_6) or on the southern plate segment (V\_7-10). The spacing between point sources can be set to represent the instability wavelength, often thought to control the regularity of volcanic vent spacing (~70km) along strike observed at many subduction zones [Marsh, 1979]. Employing multiple point sources along strike is motivated by the fact that we are trying to model a 3D layer with thickness and structure becoming unstable with point sources. When a buoyantly unstable layer intersects the instability initiation zone it is transformed into a line source of buoyancy [Marsh, 1979]. The technique of approximating continuous line sources or sinks with points has been used to study other types of subsurface flows of importance to hydrology and petroleum engineering [Weijermars and van Harmelen, 2016].

Hydrated ethanol diapirs in these experiments reproduce some of the behaviors observed by Hall and Kincaid (2001) in that they do produce rheologic weakening in the wedge creating preferential conduit paths and networks for subsequent diapirs to follow. The weak zones are passive features with minimal buoyancy so they are completely entrained in the creeping matrix flow and redistributed throughout the wedge. This not only reinforces the hypothesis that preferential weak zones can exist and provide a means of rapid ascent, but shows that those conduits are not fixed in space or time, adding complex small scale heterogeneity and nonlinearity to the structure and dynamics of flow and transport in the mantle wedge.

Figures 20 and 21 show map-view images from experiment V\_7, with downdip only subduction along a fixed 35° dip angle. Images, that focus on the left, or south side of the slab, from the slab edge to the centerline symmetry axis, show four injectors providing continuous supply of buoyant fluid. These are numbered 1-4 running from the centerline out towards the slab edge. Selected frames highlight a commonly observed progression. In contrast to work of Hall and Kincaid (2001) and section 3.2 experiments, where a single source was considered residing along the centerline of the slab, the along-trench distribution of sources shows that trench-oblique drift (Figures 20a, 21a) of ascending diapirs creates an extensive range in interaction behaviors. In Figure 20b, the diapir from source 4 (near edge) is passing outboard of and interacting with the deeper fluid from source 3. The diapir from source 2 is passing inboard of, and interacting with deeper fluid from source 1 (near slab centerline). By the time the image in Figure 20c is taken (a 5 second / 167 kyr interval) both interactions are complete. The deeper fluid has risen into and merged

with the overlying diapirs, impulsively increasing their volumes and hence their Stokes ascent rates and altering their surfacing trajectories. For scale, these both involve an order 2-3cm rise in less than 5 seconds or ~60-90 km in less than the 150 kyr time steps resolved here.

Another dramatic, repeatable style of diapir-diapir interaction involves rapid upward merger of three diapirs, from three different source regions. Figure 21a shows how diapirs from sources 3 and 4 have drifted under a shallower diapir. After 5 seconds (Figure 21b) the two deeper features have merged, causing them to rise upwards into the shallower diapir (Figure 21c). This swollen diapir rises rapidly to impact the base of the overriding plate, illustrating how such mergers can cause material to surface in much different locations than if they were free to rise and translate in background flow, without outside interference. Figures 22 and 23 show in cross-sectional side-view, examples of vertical stacking of diapirs from different sources in the along-trench direction and rapid upward migration of diapir fluid through such mergers.

In some cases these swollen surfacing diapirs can begin deforming within the stronger return flow below the overriding plate to produce an extensive under-plating feature that tends to elongate into the direction of flow. Figure 24 shows such a progression for experiment V\_9, which is similar to V\_7 but with 40° dip angle, downdip only subduction. One difference is that this case has a no-slip (zero horizontal velocity) surface boundary under the back-arc plate, which enhances return flow beneath the arc portion of the plate. During this experiment a similar vertical stacking of diapirs (Figure 24a) occurs, leading to rapid upward motion and

assimilation into a single sub-surface morphology. As this feature moves along a trench-oblique return flow path towards the wedge apex, other diapirs similarly feel and rise into this reservoir, creating a much larger sub-plate expression, slightly elongated into the prevailing flow direction (Figure 24b).

Diapir interactions and rapid vertical ascent was observed in the experiments of Hall and Kincaid (2001). New observations seen in these experiments are related to off-centerline sources interacting with the trench-parallel component of mid- and shallow-wedge return flow, and the addition of rollback subduction. Figures 25-27 show map-view and side-view images from wet ethanol experiments employing the same four distinct buoyancy sources but with rollback subduction instead of simple downdip slab motion. The basic result is the same, that rising diapirs from sources nearer the slab edge drift over and interact with sources closer in towards the slab centerline. One distinction comes from the subtle difference in return flow to the wedge apex related to rollback. In the downdip cases, return flow towards the trench/wedge apex is trench-normal through the central 3<sup>rd</sup> of the wedge and trench-oblique elsewhere, from beneath the arc plate, extending out under the back-arc plate (Figure 9). Rollback produces a different pattern. Under all of the back-arc plate and a portion of the arc plate, there is a greater trench-parallel component to the flow, abruptly transitioning to trench-normal right at the centerline. Away from the centerline, flow turns trench-oblique closer in towards the wedge apex than in downdip cases. This difference is reflected in the transport paths shown in map-view in Figure 25. Sources from near the slab edge tend to travel outboard of the source locations, along an arcuate path that makes it more difficult to vertically stack diapirs

above subsequent inner sources. As seen in the figure, a series of spaced out diapirs moves along such a path towards the wedge apex, with only minimal input from other, deeper sources. However, this is an oversimplification of a very complex set of processes. As shown in section 3.2, diapirs evolving within a single trench-normal cross-section through the wedge can experience a range of near-source processes that lead to escape and early ascent at different distances from the trench (Figure 17). Even the more arcuate map-view paths observed in rollback cases lead to strong interactions and rapid vertical ascent between distinct diapirs. Figures 26 and 27 show a number of examples for the cycle: 1) trench-parallel diapir drift towards the wedge centerline, 2) vertical alignment of buoyancy sources and rapid upward assimilation. An interesting process seen in experiment V\_10 that has a no-slip condition beneath the back-arc plate, and therefore slightly enhanced vertical flow within the wedge (Figure 27c), is that drifting over-thickened tails remnant from prior upward diapir assimilation events, may capture smaller diapirs that are otherwise stalled deeper in the wedge, allowing them an access path to the surface.

### **3.4 Special Cases**

#### **3.4.1 Slab Steepening – Experiment D\_14**

During the course of this phase of experiments we ran into a few special and noteworthy cases that warrant reporting. The first of these, experiment D\_14, used a complex subduction geometry with active slab steepening employed for the southern plate segment only. This could be viewed as a slab tearing with the northern piece continuing on the initial shallow path while the southern half drapes back into the

mantle. This is not reflective of any particular subduction zone on Earth but rather an exercise in experiment design that the apparatus is able to produce.

Both plate segments initially dipped to the east at 37 degrees. The initial arrangement of diapirs was the same on each plate segment, one trench-parallel row of 4 diapirs. The diapirs were subducted and convergence briefly paused to allow for detachment from the viscous boundary layer. When subduction resumed, active steepening of the southern plate segment at a rate of  $\sim 1$  degree of steepening for every 333 kyr was also started contemporaneously and ceased when the southern slab had reached a dip of 65 degrees at experiment time 12.6 Myr.

Three-quarters of diapirs originating on the northern plate segment were unsuccessful in overcoming the strong trench-normal wedge flow induced by the shallow plate and were subducted deeply into the mantle exiting the ROI. Only the diapir originating closest to the center of the northern slab segment was successful in ascending to the LAB. The steepening of the southern plate served to accentuate the detachment process and left the southern diapirs out in the middle of the mantle wedge far from the forced plate velocities. This group of diapirs was then drawn in laterally along-strike toward the center of the shallow northern plate segment as discussed in section 3.1.

The diapir from the southern group that originated closest the southern edge and hence farthest from the shallow plate segment had a much different trajectory (magenta circles, Figure 28). The other three diapirs from this side were advected nearly horizontally along strike toward the shallower fixed dip northern plate segment. The southern-most diapir, however, was not advected close enough to the edge of the

shallower plate before a bulge of material was extruded out of the newly formed gap between the two plate segments. This extrusion of material at depth pushed back against the lateral forces pulling in toward the shallower plate and caused this diapir to become nearly motionless at depth for a long time (Figure 28).

The residence time of that specific diapir was 18.33 minutes (36.7 Myr) , nearly twice as long as the average of all of the other successful diapirs from that experiment (Table 2). This kind of stochastic behavior is not predicted by conventional mass transport models in subduction zones where continuous material input results in continuous melt generation and volcanic output, but would clearly have an effect on mantle wedge heterogeneity, melting and depletion history of both the wedge and the diapir materials, and spatial and temporal distribution of melts and material arriving at the LAB sourced from the same region. The along strike displacement of this specific diapir was the greatest observed in all experiments. This diapir moved from the southern edge of the southern slab segment to the center of the northern plate segment. This corresponds to ~70% of the total trench width, or 525 km of lateral along strike transport.

### **3.4.2 Linear volcanic tracks – experiment D\_17**

The second notable experimental run was experiment D\_17 ( Figures 12, 29). This experiment produced an evenly spaced linear track of LAB surfacing locations at the centerline of the total slab perpendicular to the strike of the trench. Although the spacing between diapirs at the LAB was regular (~130 km), the source regions for subsequent surfacing diapirs were not characteristic of this surfacing order. That is to say material was arriving at the base of the lithosphere at regularly spaced intervals

but was not diagnostic in predicting where a subsequent or preceding diapir would have been sourced from. A diapir originating from the slab edge could arrive at the LAB following one from the middle of the slab or vice versa. This has consequences for any petrogenetic relationship along a linear volcanic track because the vents are not sampling material from the same region of the slab-wedge interface, and any magmatic lineage would not be completely obvious.

### **3.4.3 Up-dip subduction channel flow – experiment V\_3**

In this experiment diapir material was observed migrating back up dip along the SWI, which is another proposed route for buoyant material to travel, especially if the SWI is weak [Gerya *et al.*, 2002; Marschall and Schumacher, 2012; Harlow *et al.*, 2016]. In this case a diapir burst at the surface of the working fluid and spilled into the trench (a behavior produced only by wet ethanol) before being evacuated with the vacuum. The hydrous ethanol was actually drawn down and subducted creating a thin film along the SWI partially lubricating the interface and partially decoupling the wedge fluid from the slab. When this film intercepted the injection source any fluid emanating from the source immediately preferentially flowed up this weak zone instead of contributing to the formation of a new diapir. This same effect could work in nature, but it has to be relatively localized, as flow in the wedge would cease if the slab and wedge asthenosphere were not viscously coupled.

### **3.5 Unsuccessful diapirs**

Diapirs in the laboratory setting can fail to reach the LAB for a few different reasons. Unsuccessful diapirs in the solid sphere experiments were generally those that did not lift off or detach from the viscous boundary layer at the slab surface

substantially during the brief pause in plate convergence. Inconsistencies in detachment are an unfortunate reality of this method, but mostly mitigated by the use of multiple diapir tracking targets and regularly spaced arrays. If one diapir is strongly embedded in the viscous boundary layer and fails to detach, the neighbors provide us with some of the same information. Not all material that enters a subduction zone is expected to successfully resurface as diapirs so this does not negate our conclusions.

Solid diapirs were also sometimes unsuccessful for experimental configurations that had a greater vertical velocity component in the wedge caused by steeper slabs or faster convergence rates. Since the rigid spheres have fixed buoyancy (they do not change size or density), the primary adjustments must be made to the subduction side of the force balance acting on a diapir. In the fluid diapir experiments we had the ability if needed to alter the buoyancy flux to create successful diapirs while maintaining a desired model configuration. We also experimented with populating the underside of the plate with solid spheres as well to see if they would be brought into the wedge through a slab gap or around the edge by toroidal rollback flow. None of these sub-slab diapirs were successful, so we do not expect any sub-slab material to enter or influence the wedge. In general for all the cases, diapirs that detach farther down dip have less of a chance of successful ascent. Unsuccessful fluid diapirs were those that were small relative to the average size for a given experiment. They failed to develop fully and detached from the buoyancy source prematurely before becoming entrained in the matrix flow and being subducted to depth and exiting the ROI.

#### 4. Implications

The primary method of investigation is physical tectonic-fluid dynamic analogue laboratory modeling of the asthenospheric upper mantle. The primary variables explored are the style and geometry of subduction, the density contrast between the working and injected fluids, and the volumetric flux emanating from the source. This volumetric buoyancy flux can be correlated to a thickness of the unstable layer entering the subduction zone (see Figure 8 in Marsh (1979)). Analogue modeling has a long and rich history and has been used extensively in both geology and fluid dynamics [Hall, 1815; Hubbert, 1937; Riehl and Fultz, 1958]. See [Schellart and Strak, 2016] for a comprehensive review of geodynamic applications of analogue modeling approaches. Scaled lab modeling provides an elegant, insightful, and intuitive way of visualizing complex multi-scale processes, and allows for the examination of the fundamental dynamics in question. In contrast, computational numerical modeling requires the discretization of continuous fields onto a grid while analogue modeling maintains the inherent continuity. Modeling in the lab eliminates the need for parameterization of sub-grid scale processes as all the intrinsic length scales (encompassing six orders of magnitude) are present. This property of analogue modeling can be helpful in identifying anomalous or non-realistic behavior within and better constraining numerical geodynamic simulations.

The solid diapir experiments provided the ability to verify our fluid results. We do not want our external injection pressure to be too great and actually forcefully pump the diapir fluid vertically. This over-pressurization of the injected fluid is thought to produce more vertical paths because 1) it would maintain a connection with

the source longer, allowing for diapirs to grow to be too large, and 2) we would be adding an upward vertical component to the diapir in addition to its own buoyancy. Because the fixed-buoyancy solid and flux-buoyancy fluid diapir pathways look similar we assert that we are not forcing fluid into the system in an unphysical manner and looking at different physical processes. The desire is for our fluid injection to be as passive as possible and have the injection process itself minimally disturb the flow. Essentially the goal is to push the fluid just hard enough to flow out from the source and immediately become entrained in the flow like dye being released and drawn passively into a stream. We are modeling solid state creep deformation processes of the mantle using a viscous fluid. Approximating the asthenosphere as a viscous fluid is acceptable over geologic time scales. It is then also appropriate to model the less viscous, buoyant diapirs with a fluid as well to better encapsulate the interactions we are seeking to explore. As discussed in our findings near-vertical ascent was not observed even with excessively buoyant material for the entire suite of subduction geometries, convergence rates, and buoyancy fluxes tested. Again, the density contrasts explored here are somewhat larger than expected for mantle wedge diapirs, which would be something on the order of 25%. However, if vertical source-vent pathways cannot be produced with the buoyancy that arises from our experimental density contrasts, it is unlikely that a smaller density contrast would result in diapirs experiencing less deflection. Therefore, we explored a range of possible density contrasts required to create near vertical ascent through the mantle wedge.

One of the buoyant fluids also contained water, which can have a strong effect on local matrix viscosity, and consequently diapir behavior in the analogue setting.

Water is thought to play a similar role in the natural mantle wedge prototype, lowering viscosity at the slab-wedge interface and within the actively convecting wedge facilitating rapid transport [*van Keken, 2003; Grove et al., 2006; Wada and Wang, 2009; Jadamec, 2016*]. Glucose rheology is heavily dependent on water content; there is roughly a 30% reduction in viscosity for each 1 wt% water added at 20 °C [*Schellart, 2011*]. The water in the wet ethanol diapirs can weaken the ambient matrix viscosity locally by up to two orders of magnitude. These localized weak zones are small features that become entrained in and advected by wedge flow, constantly redistributing heterogeneous features in space and time. Large scale chemical diffusion of this added water is negligible on experimental timescales, and the large volume of the tank relative to the ROI (ROI is less than 3.6% of the total tank volume) compensates for this effect. Hydrated ethanol diapirs are able to fully coalesce and reorganize into single bodies. This is thought to be attributable to water and its effect on bubble and droplet surface tension and viscosity at the material interface.

Natural diapirs themselves may melt by any of the three primary mechanisms: 1) external heating, 2) pressure release, 3) H<sub>2</sub>O flux altering the solidus. Sea-floor sediments and altered oceanic crust descend into the subduction zone at the surface of the cold lithospheric slab. The slab and accompanying material is cold relative to the surrounding mantle and as such diapirs are heated externally by the wedge throughout their ascent. The subducted diapir protomaterial may also be hydrated, resulting in a lower melting point than the surrounding wedge material. As the buoyant diapir material ascends, decompression and pressure release melting occur. All three of these are viable mechanisms supporting melt generation of and by diapirs as they traverse

the mantle wedge, see Appendix 2. Water plays a key role in melt generation processes in subduction zones at and above the slab-wedge interface [Davies and Stevenson, 1992; Schmidt and Poli, 1998; van Keken, 2003; Grove et al., 2006; Hirschmann, 2006; Kelley et al., 2010]. Dehydration of hydrous phases at depth releases water that locally depresses the solidus initiating partial melting of the peridotitic mantle wedge. If diapirs carry water with them into the wedge they will leave behind a trail of wet heterogeneity with enhanced melt potential. These trails are also weak allowing for subsequent diapirs to follow in these channels and ascend rapidly [Hall and Kincaid, 2001].

There is also some variance in constraining the rheologic flow law for olivine and bulk mantle compositions [Karato, 2010; King, 2016]. There are certainly many unknown or poorly constrained parameters that are of great importance to the overall dynamics of subduction zones and the mantle wedge. However the past and present plate rates that are supplying material into modern subduction zones are well known, and we leverage this as a starting point to investigate how the geologic protomaterial for rocks we observe at the surface interacts with the large-scale wedge flow. Resolving all of the complexities of the subduction system is computationally expensive and complex. There are many dynamic feedbacks to the subduction system that are poorly constrained due to lack of directly measurable evidence. Until experimental and remote sensing efforts improve our ability to probe subduction zones and better constrain the system we must rely on theoretical, numerical, and analog models to gain insight. Altering some of the most basic assumptions commonly made about the subduction system can have drastic effects on model results and ultimate

interpretation and understanding. The composition of the mantle wedge is not known with great certainty and is often assumed to be homogeneous with a bulk peridotite mineralogy dominated by olivine. Actual mantle xenoliths and ophiolite sections provide evidence that the sublithospheric mantle and wedge is not well mixed and can be highly heterogeneous in the compositional, thermal, and stress fields in both space and time [*Behn and Kelemen, 2006; Behn et al., 2007; Le Voyer et al., 2017*]. Global Rayleigh numbers for mantle convection are  $5e5$  and  $5e7$  for layered and whole mantle convection respectively [*Turcotte and Schubert, 2014*], indicating time dependent nature of mantle convection systems. The creeping wedge flow was minimally disturbed by the presence and ascent of diapirs. Flow in the shallow upper corner near the trench (wedge apex) is not cut off as might be predicted if only two spacial dimensions are considered. Flow in the wedge apex does not become separated from the rest of the wedge. This is a consequence of the 3D nature of the flow and the accommodation of material in the third dimension not included in 2D corner flow models [*Gerya and Yuen, 2003; Hasenclever et al., 2011*]. Three space dimensions and time evolution are necessary to evaluate this complex system, especially if we wish to evaluate trench-parallel transport along strike.

## 5. Conclusions

A suite of analogue models was used to examine the interactions between compositionally buoyant diapiric upwellings and a large scale three-dimensional time evolving viscous mantle wedge flow. We produced Lagrangian position vectors for individual diapirs for a range of experimental parameters. These experiments have shown that it is very difficult to produce vertical wedge transit pathways, even for extremely buoyant diapir materials and large volume fluxes. This confirms that material transiting the wedge from the melt generation zone at the slab-wedge interface interacts with and is deflected by the large-scale forced mantle wedge flow en route to the base of the lithosphere. For the full range of buoyancy fluxes and subduction geometries investigated, buoyant material is advected by the forced wedge flow away from the trench in arcuate paths by the lower branch of the wedge flow into the hottest core of the mantle wedge. We have shown that even with extreme density contrasts not typical of the mantle, direct vertical connectivity between the vent and source region is unlikely. Unless vertical transport velocities are much greater than the dominant wedge forcing, the two must interact. It is unreasonable to separate the two modes of flow or assume that they are independent of each other. When three spatial dimensions are considered, along-strike transport of material is present and complicates spatial and temporal petrogenetic relationships between arc rocks observed at the surface and the implied source region directly beneath the arc.

The first set of experiments (arrays of rigid spherical diapirs) demonstrated that initial diapir source / detachment location markedly effects diapir success, residence time, and surfacing location. Additionally the style of subduction (downdip, rollback,

variable dip) and surface boundary condition modulate diapir transit pathways and surfacing patterns, producing voluminous volcanic output under the central 3<sup>rd</sup> of the sub-arc plate as well as linear trench-normal trends of surfacing locations. These experiments mapped flow near ROI boundaries and establish the significance of 3-D time-evolving flow influences.

The second phase of experiments presented (single dry ethanol source at slab centerline) most closely reproduced the results of Hall and Kincaid (2001) but removed the complexity of introducing rheologic weakening and heterogeneity into the wedge. We discussed 3 modes of diapir surfacing styles effected by interactions with three cross-sectional wedge flow regimes (deep VBL (1), central quiescent region (2), moderate shallow return flow (3)) and some diapir-diapir interactions. These experiments showed that with constant subduction parameters and constant buoyancy flux predicting diapir paths and surfacing locations is not straight forward. Small diapirs can cluster down-dip from the source and alter their collective path, and material can migrate back up-dip to rapidly fill a smaller newly developing diapir drastically altering its detachment process and subsequent ascent path.

The third experimental phase built upon prior work by adding the complexities of multiple sources spaced along the strike of the trench and incorporating a fluid which alters the rheology of the wedge. These experiments produced results in line with previous findings of Hall and Kincaid (2001) by producing preferential weak zones and conduit tail networks but also adds rollback style subduction, variable surface boundary condition, and modeling of a continuous line source of buoyant instability along strike instead of a single point. These results show diapir material

arising from different source locations mixing and interacting to produce rapid ascent and voluminous output in the presence of toroidal flow induced by rollback style subduction. These were the most complex experiments, including all of the variables tested.

The observed variability in path-length, residence time, and ultimate diapir success highlights the complexities which must be considered when investigating relationships between subducted material input, interactions with the mantle wedge, and surface observable output. When advective transport dominates, diapirs are dragged to depth with the slab before buoyant detachment from the viscous boundary layer and fast velocity layer can occur. When buoyant transport dominates, diapirs detach and ascend rapidly having limited interaction with the wedge, but are still deflected by it. Even with the largest density contrast and buoyancy flux considered no diapir was ever observed to make a purely vertical transit. It is when the scales of the competing advective and buoyant forcings are similar that small perturbations and heterogeneities become important in determining diapir success.

## References

- Behn, M. D., and P. B. Kelemen (2006), Stability of arc lower crust: Insights from the Talkeetna arc section, south central Alaska, and the seismic structure of modern arcs, *J. Geophys. Res. Solid Earth*, *111*(B11), doi:10.1029/2006JB004327.
- Behn, M. D., G. Hirth, and P. B. Kelemen (2007), Trench-Parallel Anisotropy Produced by Foundering of Arc Lower Crust, *Science* (80-. ), *317*(5834).
- Bellahsen, N., C. Faccenna, and F. Funiciello (2005), Dynamics of subduction and plate motion in laboratory experiments: Insights into the “plate tectonics” behavior of the Earth, *J. Geophys. Res. B Solid Earth*, *110*, 1–15, doi:10.1029/2004JB002999.
- Berner, H., H. Ramberg, and O. Stephansson (1972), Diapirism theory and experiment, *Tectonophysics*, *15*(3), 197–218, doi:10.1016/0040-1951(72)90085-6.
- Davies, J. H., and D. J. Stevenson (1992), Physical model of source region of subduction zone volcanics, *J. Geophys. Res. Solid Earth*, *97*(B2), 2037–2070, doi:10.1029/91JB02571.
- Druken, K. A., C. Kincaid, R. W. Griffiths, D. R. Stegman, and S. R. Hart (2014), Plume–slab interaction: The Samoa–Tonga system, *Phys. Earth Planet. Inter.*, *232*, 1–14, doi:10.1016/j.pepi.2014.03.003.
- Funiciello, F., M. Moroni, C. Piromallo, C. Faccenna, A. Cenedese, and H. a. Bui (2006), Mapping mantle flow during retreating subduction: Laboratory models analyzed by feature tracking, *J. Geophys. Res.*, *111*(B3), B03402, doi:10.1029/2005JB003792.
- Gerya, T. V, and D. A. Yuen (2003), Rayleigh–Taylor instabilities from hydration and melting propel “cold plumes” at subduction zones, *Earth Planet. Sci. Lett.*, *212*(1), 47–62, doi:10.1016/S0012-821X(03)00265-6.
- Gerya, T. V., B. Stöckhert, and A. L. Perchuk (2002), Exhumation of high-pressure metamorphic rocks in a subduction channel: A numerical simulation, *Tectonics*, *21*(6), 6-1-6–19, doi:10.1029/2002TC001406.
- Grove, T. L., N. Chatterjee, S. W. Parman, and E. Médard (2006), *The influence of H<sub>2</sub>O on mantle wedge melting*.
- Hall, J. (1815), II. On the Vertical Position and Convolutions of certain Strata, and their relation with Granite, *Trans. R. Soc. Edinburgh*, *7*(1), 79–108, doi:10.1017/S0080456800019268.

- Hall, P. S., and C. Kincaid (2001), Diapiric Flow at Subduction Zones: A Recipe for Rapid Transport, *Science* (80-. ), 292(5526).
- Harlow, G. E., K. E. Flores, and H. R. Marschall (2016), Fluid-mediated mass transfer from a paleosubduction channel to its mantle wedge: Evidence from jadeitite and related rocks from the Guatemala Suture Zone, *Lithos*, 258, 15–36, doi:10.1016/j.lithos.2016.04.010.
- Hasenclever, J., J. P. Morgan, M. Hort, and L. H. Rüpke (2011), *2D and 3D numerical models on compositionally buoyant diapirs in the mantle wedge*.
- Hirschmann, M. M. (2006), WATER, MELTING, AND THE DEEP EARTH H<sub>2</sub>O CYCLE, *Annu. Rev. Earth Planet. Sci.*, 34(1), 629–653, doi:10.1146/annurev.earth.34.031405.125211.
- Hubbert, M. K. (1937), Theory of scale models as applied to the study of geologic structures, *Geol. Soc. Am. Bull.*, 48(10), 1459–1520, doi:10.1130/GSAB-48-1459.
- Jadamec, M. A. (2016), Insights on slab-driven mantle flow from advances in three-dimensional modelling, *J. Geodyn.*, 100, 51–70, doi:10.1016/j.jog.2016.07.004.
- Karato, S. (2010), Rheology of the Earth's mantle: A historical review, *Gondwana Res.*, 18(1), 17–45, doi:10.1016/j.gr.2010.03.004.
- van Keken, P. E. (2003), The structure and dynamics of the mantle wedge, *Earth Planet. Sci. Lett.*, 215(3), 323–338, doi:10.1016/S0012-821X(03)00460-6.
- Kelley, K. A., T. Plank, S. Newman, E. M. Stolper, T. L. Grove, S. Parman, and E. H. Hauri (2010), Mantle Melting as a Function of Water Content beneath the Mariana Arc, *J. Petrol.*, 51(8), 1711–1738, doi:10.1093/petrology/egq036.
- Kelly, A., D. Bercovici, A. Kelly, and D. Bercovici (1997), The clustering of rising diapirs and plume heads, *Geophys. Res. Lett.*, 24(2), 201–204, doi:10.1029/96GL03904.
- Kincaid, C., and R. W. Griffiths (2003), Laboratory models of the thermal evolution of the mantle during rollback subduction, *Nature*, 425(6953), 58–62, doi:10.1038/nature01923.
- Kincaid, C., and P. Olson (1987), An experimental study of subduction and slab migration, *J. Geophys. Res.*, 92(7), 13832, doi:10.1029/JB092iB13p13832.
- Kincaid, C., and I. S. Sacks (1997), Thermal and dynamical evolution of the upper mantle in subduction zones, *J. Geophys. Res.*, 102(B6), 12295, doi:10.1029/96JB03553.

- Kincaid, C., K. A. Druken, R. W. Griffiths, and D. R. Stegman (2013), Bifurcation of the Yellowstone plume driven by subduction-induced mantle flow, *Nat. Geosci.*, 6(5), 395–399, doi:10.1038/ngeo1774.
- King, S. D. (2016), Reconciling laboratory and observational models of mantle rheology in geodynamic modelling, *J. Geodyn.*, 100, 33–50, doi:10.1016/j.jog.2016.03.005.
- MacDougall, J. G., C. Kincaid, S. Szwaja, and K. M. Fischer (2014), The impact of slab dip variations, gaps and rollback on mantle wedge flow: insights from fluids experiments, *Geophys. J. Int.*, 197(2), 705–730, doi:10.1093/gji/ggu053.
- Manga, M. (1997), Interactions between mantle diapirs, *Geophys. Res. Lett.*, 24(15), 1871–1874, doi:10.1029/97GL01889.
- Marschall, H. R., and J. C. Schumacher (2012), Arc magmas sourced from mélange diapirs in subduction zones, *Nat. Geosci.*, 5(12), 862–867, doi:10.1038/ngeo1634.
- Marsh, B. D. (1979), Island Arc Development : Some Observations , Experiments , and Speculations, *J. Geol.*, 87(6), 687–713, doi:0022-1376/79/8706-0002.
- Miller, N. C., and M. D. Behn (2012), Timescales for the growth of sediment diapirs in subduction zones, *Geophys. J. Int.*, 190(3), 1361–1377, doi:10.1111/j.1365-246X.2012.05565.x.
- Nettleton, L. L. (1934), Fluid Mechanics of Salt Domes, *Am. Assoc. Pet. Geol. Bull.*, 18(9), 1175–1204.
- Olson, P., and I. S. Nam (1986), Formation of seafloor swells by mantle plumes, *J. Geophys. Res. Solid Earth*, 91(B7), 7181–7191, doi:10.1029/JB091iB07p07181.
- Olson, P., and H. Singer (1985), Creeping plumes, *J. Fluid Mech.*, 158(1), 511, doi:10.1017/S0022112085002749.
- Oxburgh, E. R., E. M. Parmentier, C. Froidevaux, and B. Harte (1978), Thermal Processes in the Formation of Continental Lithosphere [and Discussion], *Philos. Trans. R. Soc. London A Math. Phys. Eng. Sci.*, 288(1355).
- Piomallo, C., T. W. Becker, F. Funiciello, and C. Faccenna (2006), Three-dimensional instantaneous mantle flow induced by subduction, *Geophys. J. Int.*, 33(8), L08304, doi:10.1029/2005GL025390.
- Rayleigh (1882), Investigation of the Character of the Equilibrium of an Incompressible Heavy Fluid of Variable Density, *Proc. London Math. Soc.*, s1-14(1), 170–177, doi:10.1112/plms/s1-14.1.170.

- Richards, M. A., and R. W. Griffiths (1988), Deflection of plumes by mantle shear flow: experimental results and a simple theory, *Geophys. J. Int.*, *94*(3), 367–376, doi:10.1111/j.1365-246X.1988.tb02260.x.
- Riehl, H., and D. Fultz (1958), The general circulation in a steady rotating-dishpan experiment, *Q. J. R. Meteorol. Soc.*, *84*(362), 389–417, doi:10.1002/qj.49708436207.
- Rosen, J. (2016), The Subduction Zone Observatory takes shape, *Science* (80-. ), *353*(6306), 1347–1348, doi:10.1126/science.353.6306.1347.
- Schellart, W. P. (2011), Rheology and density of glucose syrup and honey: Determining their suitability for usage in analogue and fluid dynamic models of geological processes, *J. Struct. Geol.*, *33*(6), 1079–1088, doi:10.1016/j.jsg.2011.03.013.
- Schellart, W. P., and V. Strak (2016), A review of analogue modelling of geodynamic processes: Approaches, scaling, materials and quantification, with an application to subduction experiments, *J. Geodyn.*, *100*, 7–32, doi:10.1016/j.jog.2016.03.009.
- Schmidt, M. W., and S. Poli (1998), Experimentally based water budgets for dehydrating slabs and consequences for arc magma generation, *Earth Planet. Sci. Lett.*, *163*(1), 361–379, doi:10.1016/S0012-821X(98)00142-3.
- Stern, R. J. (2002), Subduction zones, *Rev. Geophys.*, *40*(4), 1012, doi:10.1029/2001RG000108.
- Szwaja, S. A., and C. Kincaid (2015), The Role of Mantle Residuum in Subduction-Driven Circulation: Implications for the Cascades System, *Open Access Master's Theses*.
- Tamura, Y. et al. (2011), Two Primary Basalt Magma Types from Northwest Rota-1 Volcano, Mariana Arc and its Mantle Diapir or Mantle Wedge Plume, *J. Petrol.*, *52*(6), 1143–1183, doi:10.1093/petrology/egr022.
- Taylor, G. (1950), The Instability of Liquid Surfaces when Accelerated in a Direction Perpendicular to their Planes. I, *Proc. R. Soc. London A Math. Phys. Eng. Sci.*, *201*(1065).
- Thielicke, W., E. Stamhuis, T. William, and J. S. Eize (2010), Pivlab-time-resolved digital particle image velocimetry tool for matlab, ... *under BSD Licens. Program. with MATLAB*, 1–4, doi:doi:10.6084/m9.figshare.1092508.
- Turcotte, D., and G. Schubert (2014), *Geodynamics*, Cambridge University Press.

- Le Voyer, M. et al. (2017), Heterogeneity in mantle carbon content from CO<sub>2</sub>-undersaturated basalts, *Nat. Commun.*, *8*, 14062, doi:10.1038/ncomms14062.
- Wada, I., and K. Wang (2009), Common depth of slab-mantle decoupling: Reconciling diversity and uniformity of subduction zones, *Geochemistry, Geophys. Geosystems*, *10*(10), n/a-n/a, doi:10.1029/2009GC002570.
- Weijermars, R., and A. van Harmelen (2016), Breakdown of doublet recirculation and direct line drives by far-field flow in reservoirs: implications for geothermal and hydrocarbon well placement, *Geophys. J. Int.*, *206*(1), 19–47, doi:10.1093/gji/ggw135.
- Weinberg, R. F., and Y. Y. Podladchikov (1995), The rise of solid-state diapirs, *J. Struct. Geol.*, *17*(8), 1183–1195, doi:10.1016/0191-8141(95)00004-w.
- Whitehead, J. A., and D. S. Luther (1975), Dynamics of laboratory diapir and plume models, *J. Geophys. Res.*, *80*(5), 705–717, doi:10.1029/JB080i005p00705.

## FIGURES

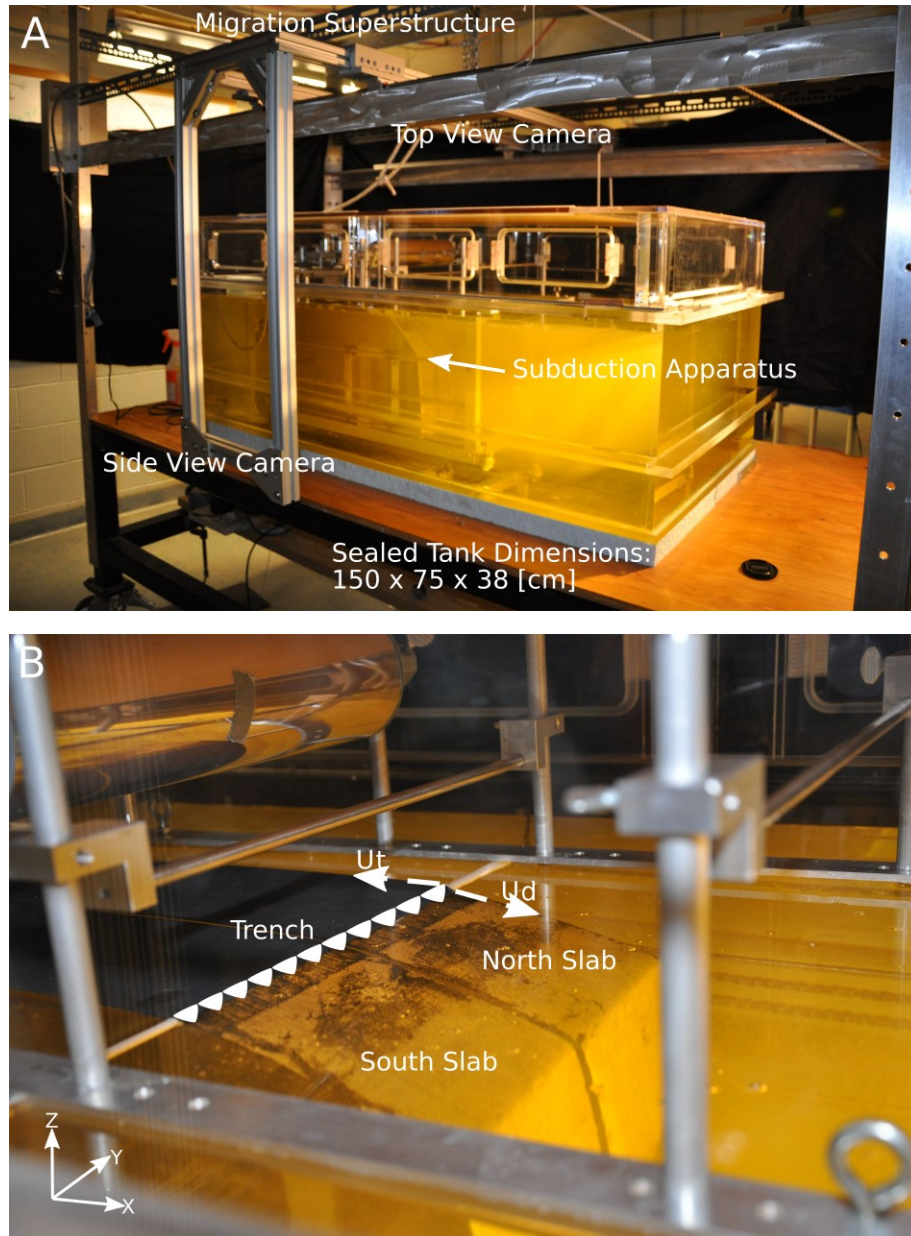


**Figure 1.** a) Photograph of laboratory setup. The tank sits on a table with the subduction apparatus fully submerged within the analogue working fluid. The subduction apparatus and camera systems translate together along the migration superstructure. b) Oblique view of the region of interest (ROI) showing fluid surface relative to the subduction apparatus, trench, and slab segments.  $U_t$  is trench migration vector and  $U_d$  is down-dip convergence vector. Cartesian coordinate axes denoted in bottom left.

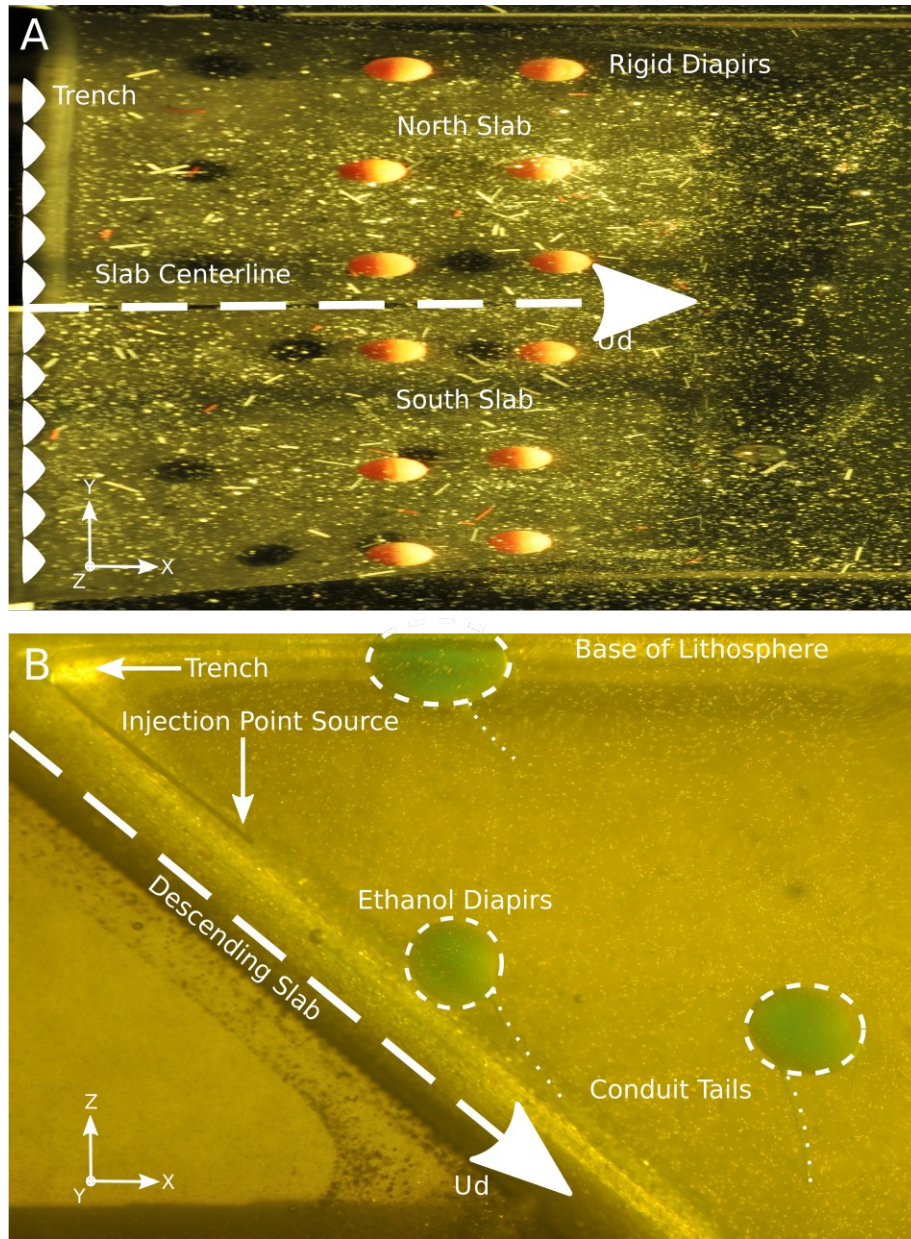


**Figure 2.** a) Annotated top-view from a rigid sphere experiment showing initial distribution of diapirs at depth embedded in viscous boundary layer of slab-wedge interface (SWI).  $U_d$  is down-dip convergence vector. Coordinate axes in bottom left. b) Annotated side-view from a dry ethanol experiment taken from the south looking north through the ROI. Diapirs and tails highlighted. Injection point sources is at  $\sim 100$  km depth. Coordinate axes in bottom left.

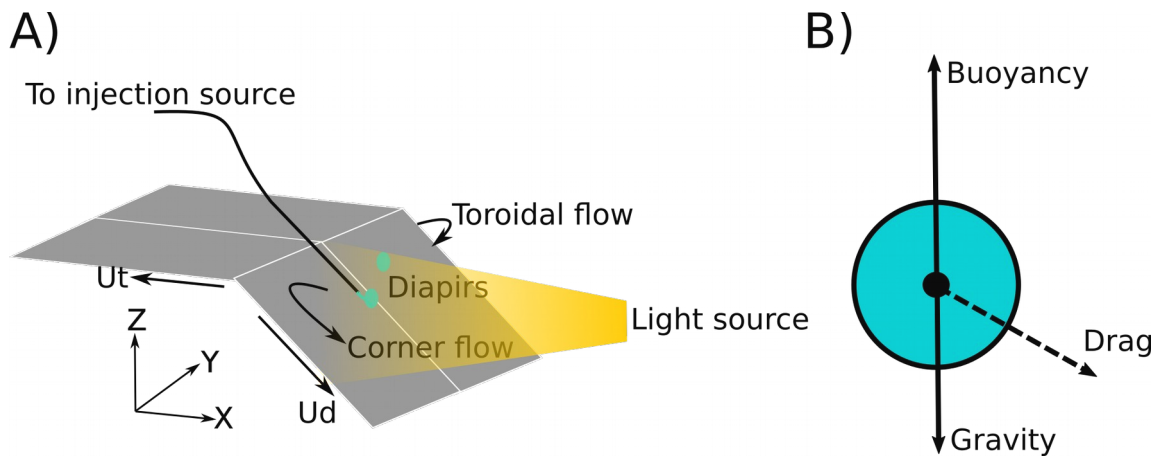


**Figure 3.** a) Simplified schematic diagram of the subduction apparatus ROI. Trench migration and convergence vectors are indicated by  $U_t$  and  $U_d$  respectively. Curved arrows are simplified representations of major modes of flow, corner flow forced by viscous coupling of the analogue fluid to the slab surface and a toroidal flow component forced by trench migration. b) Free-body diagram of forces acting upon a diapir. Drag force is dashed because it is variable in both magnitude and direction, while buoyancy force maintains vertical orientation.

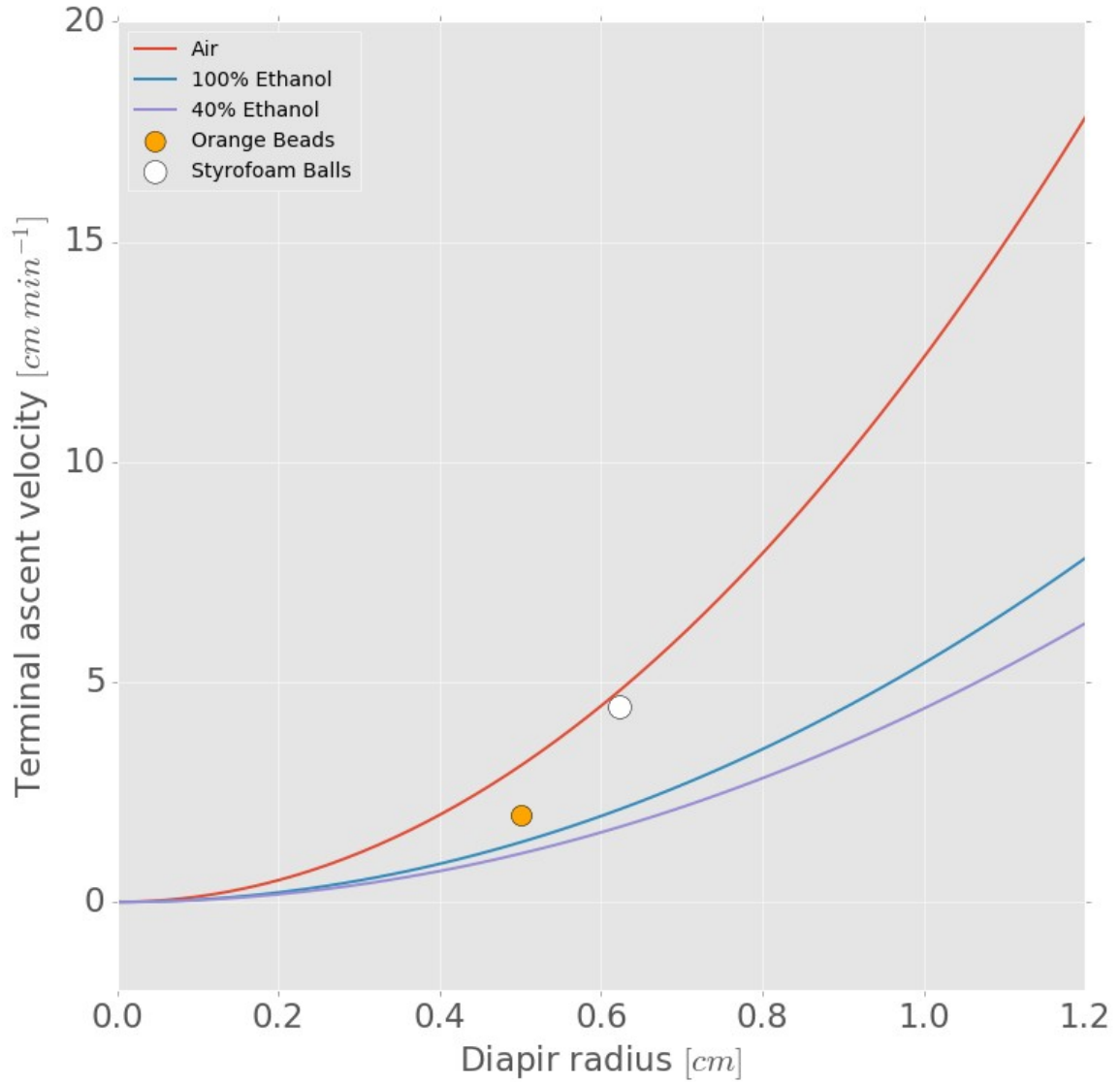


**Figure 4.** Ideal Stoke's terminal ascent velocity curves for the buoyant diapir fluids utilized in this study and single markers for rigid spheres tested. Largest diapirs observed experimentally had radii of approximately 1 cm. Range of free ascent velocities shown are on same order as convergence and migration velocities tested, meaning none are negligible and strong interaction is expected.

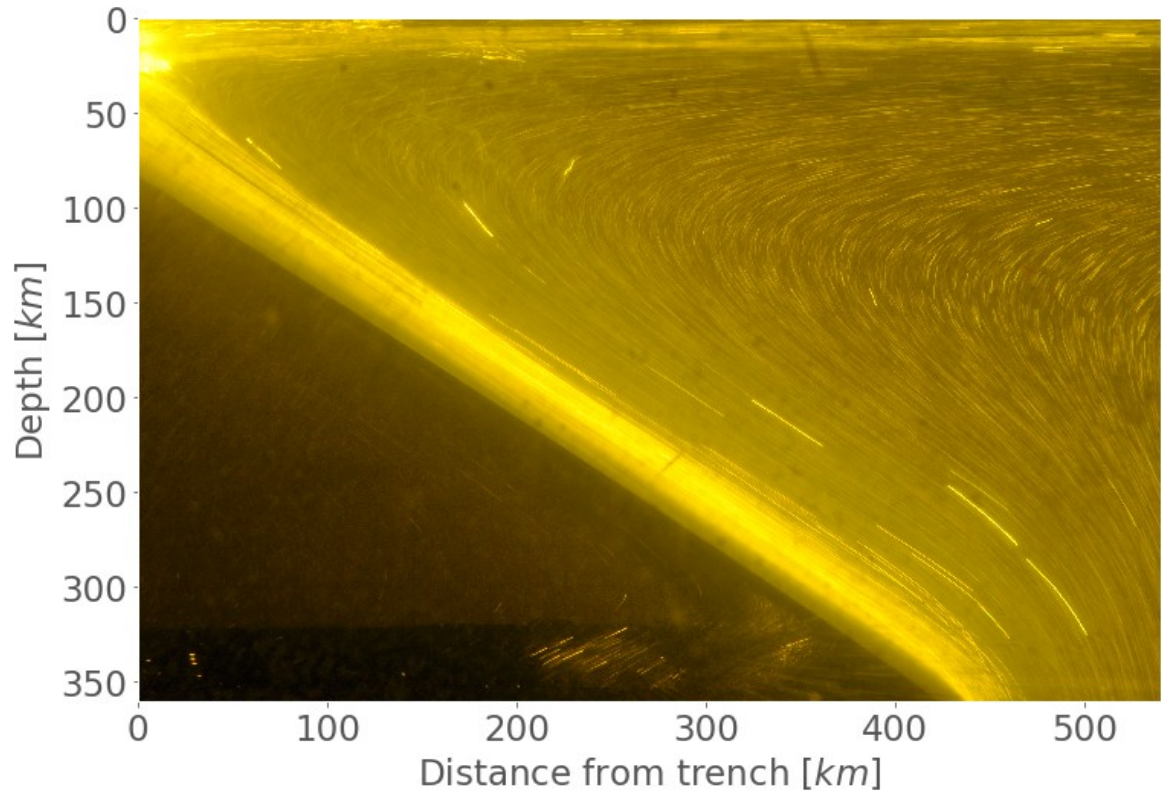


**Figure 5.** Side-view long exposure image showing flow stream lines in cross section. Long white features are finite-strain markers (whiskers) that align with flow.

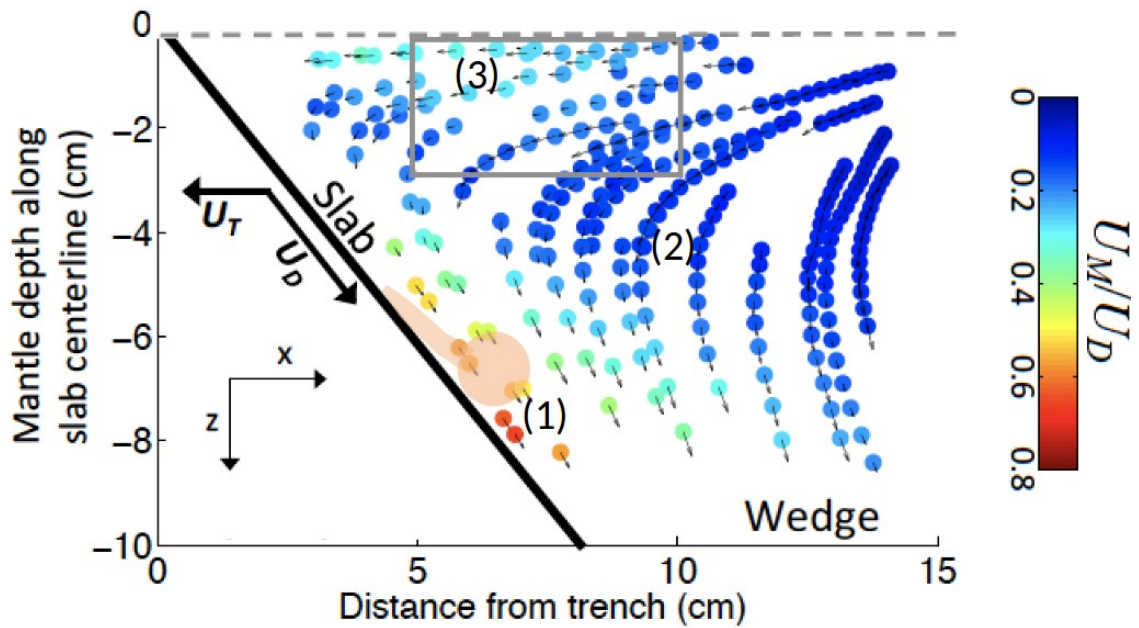


**Figure 6.** Side-view plot from Szwaja, 2015 showing velocity magnitude of Lagrangian parcels moving into the shallow wedge and downward above subducting plate with rollback. Velocity magnitude ( $U_M$ ) (color bar) is given as a dimensionless percentage of the downdip plate speed ( $U_D$ ). Warmer colors show the velocity boundary layer (VBL) above the slab into which diapir material is released. Diapirs encounter three flow regimes: 1: The rapid downward VBL, 2: Sluggish descending flow through central wedge, 3: Intermediate speed flow towards the sub-arc and trench. Shallow flow rate varies between 30-50% of  $U_D$  depending on diapir release/source location above slab (e.g., Figure 9). Hypothetical fluid diapir shown in red being drawn down within VBL.

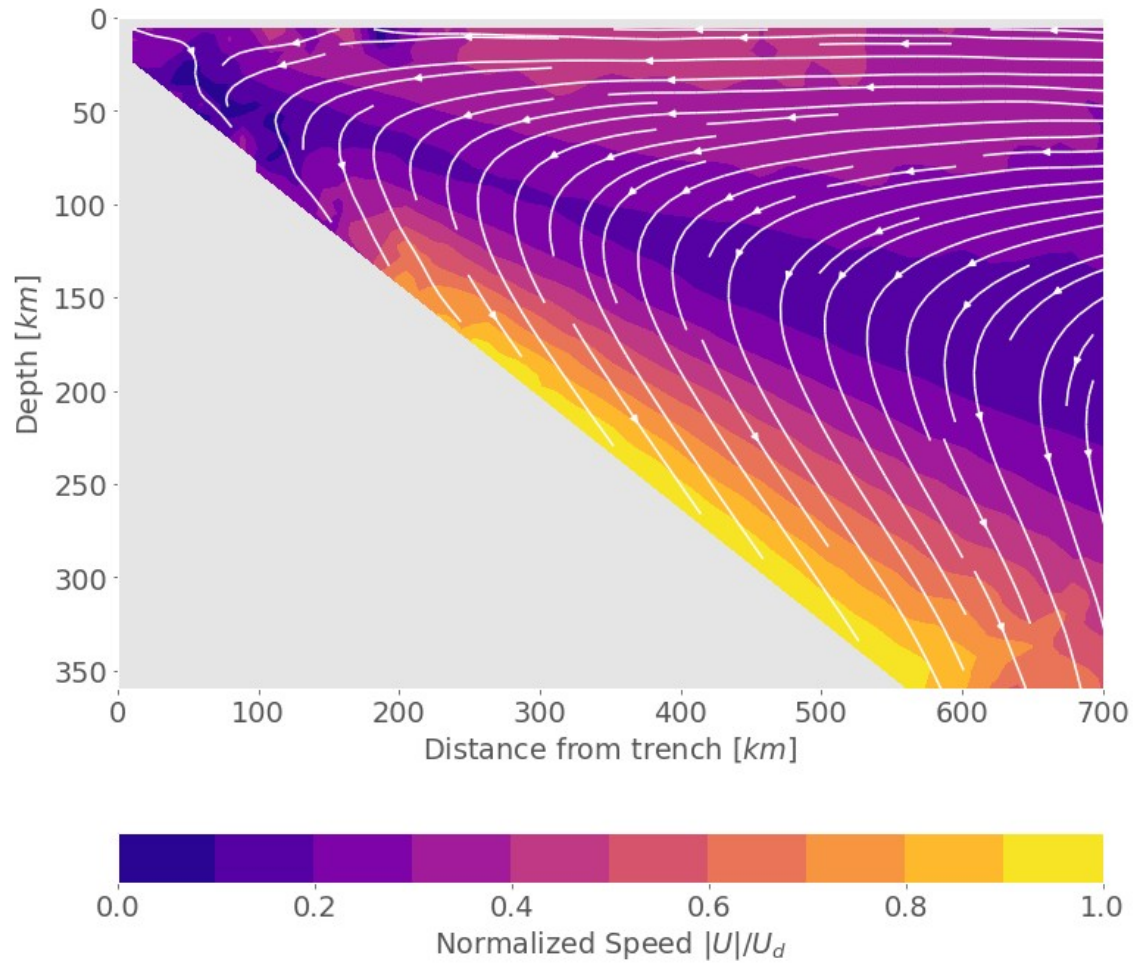


**Figure 7.** Cross section of average velocity magnitude with streamlines plotted for experiment ED\_7. In the time averaged flow vertical perturbations from diapir ascent are eliminated and the flow resembles the sparsely measured standard corner flow reported by previous authors.

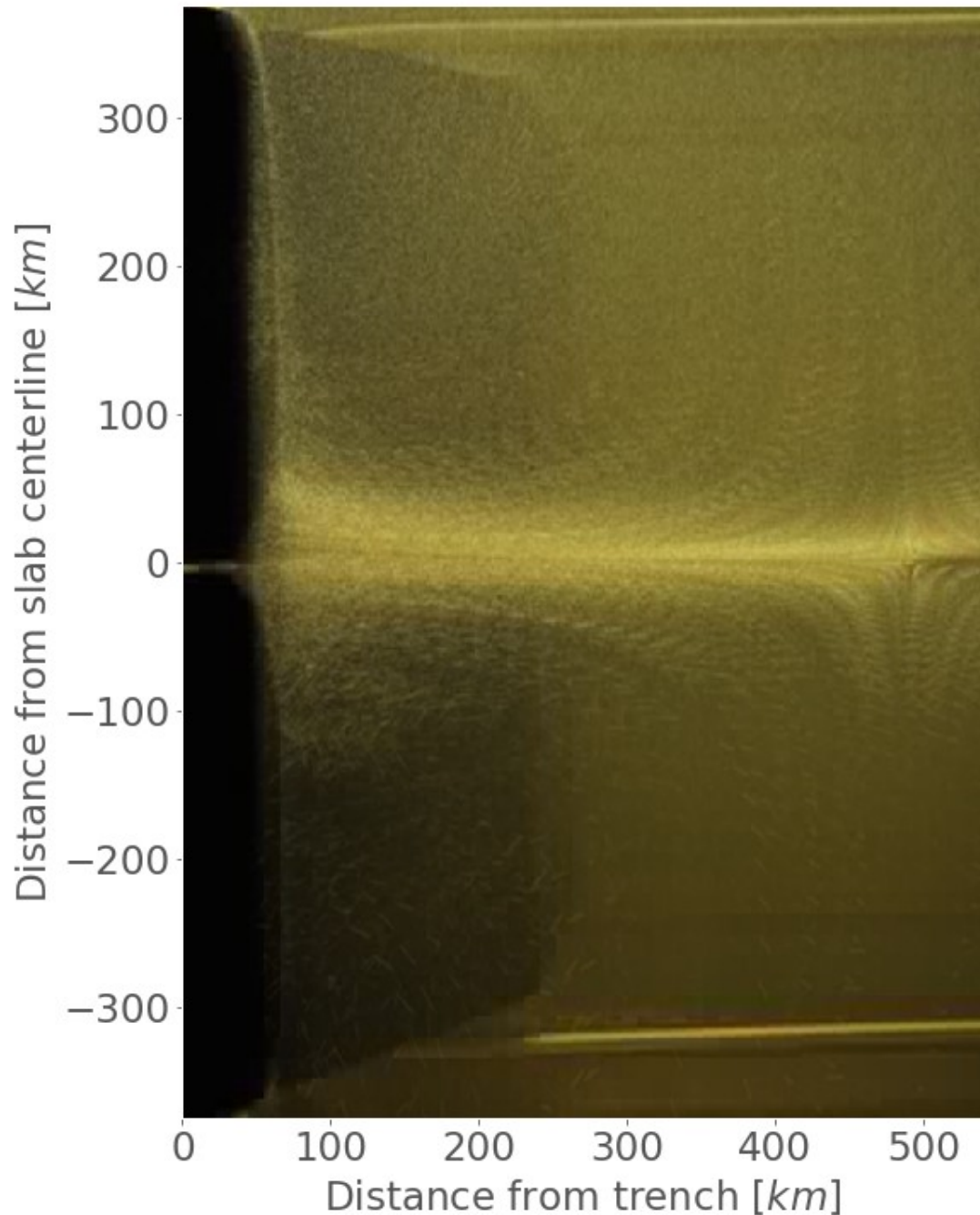


**Figure 8.** Top-view faux long-exposure image produced by image stacking and averaging across  $\sim 15$  frames. Streamlines show material being drawn inward from the sides toward the slab centerline. The saddle point with no apparent motion relative to the trench is very clear at the right of the image (star shape). This point migrates with the trench and demonstrates why frame of reference is so important when considering rollback style subduction. Material that appears to be translating to the left is actually still moving to the right slower than the trench migration rate.

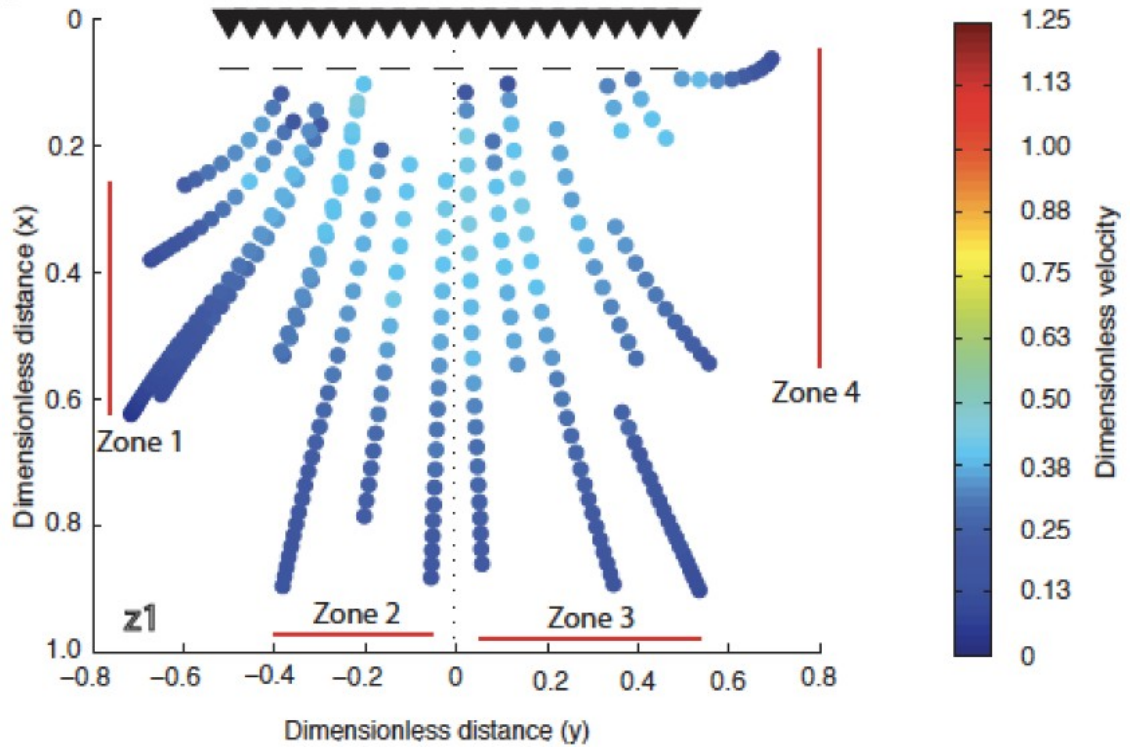


**Figure 9.** Map-view plot from MacDougall et al., 2014 showing velocity magnitude of Lagrangian parcels moving in the shallow wedge for the same belt drive subduction apparatus for a case of simple downdip-only subduction ( $50^\circ$  dip). The trench location is represented with black triangles. Velocity magnitude (color bar) is given as a dimensionless percentage of the downdip plate speed. Zones are marked that highlight spatial variability in source regions supplying sub-arc region of subduction zone.

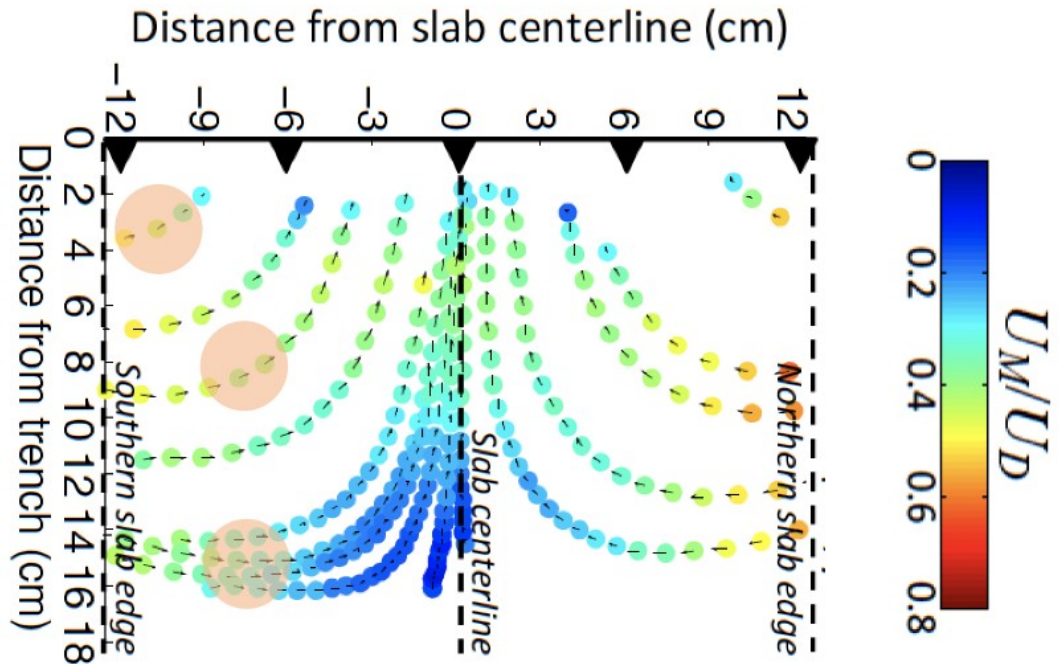


**Figure 10.** Map-view plot from Szwaja, 2015 showing velocity magnitude of Lagrangian parcels moving in the shallow wedge for the same belt drive subduction apparatus for a case of rollback subduction. The trench location is represented with black triangles. Velocity magnitude ( $U_M$ ) (colorbar) is given as a dimensionless percentage of the downdip plate speed ( $U_D$ ). Plots show how toroidal flow around retreating slab brings material along trench-parallel paths towards the wedge centerline far from the trench, before turning trench-normal. Shallow flow to the subarc is along curved paths, roughly similar to downdip only cases. Diapirs rising from different parts of the slab will experience different shallow return flow speeds and magnitudes (highlighted by hypothetical red diapirs).

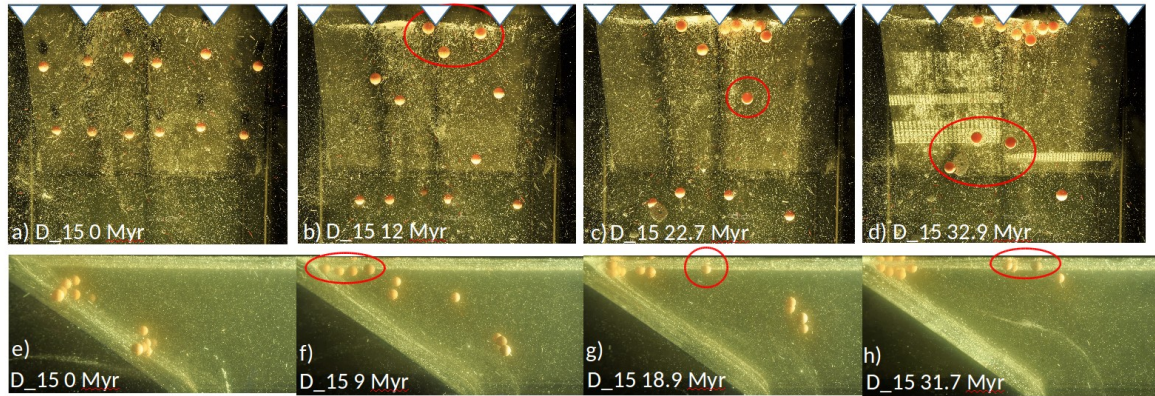


**Figure 11.** Map-view (a-d) and side-view (e-h) images of rigid diapirs (Case D\_15, Tables 1, 2) rising into the most simple plate-flow scenario, or downdip-only slab motion. a) and e): Initial conditions for two rows of 6 diapirs distributed in a trench-parallel orientation within the velocity boundary layer (VBL) above the sinking plate. The use of two rows roughly represents the buoyancy input proposed for different fluid-release mineral phase changes, a sub-arc and a rear-arc output (Ringwood, 1982). Red circles in frames b-d, f-h highlight surfacing diapirs and locations of expected melt delivery to the base of the plate. Near-surface, plate-driven 3-D return flow towards the trench has a significant trench-parallel component, producing a clump of diapirs in the central 3<sup>rd</sup> of trench, in the sub-arc region. The second rank of diapirs surfaces in the back-arc, as an arcuate shaped, trench-parallel feature. Trench location indicated by white triangles in upper panels.

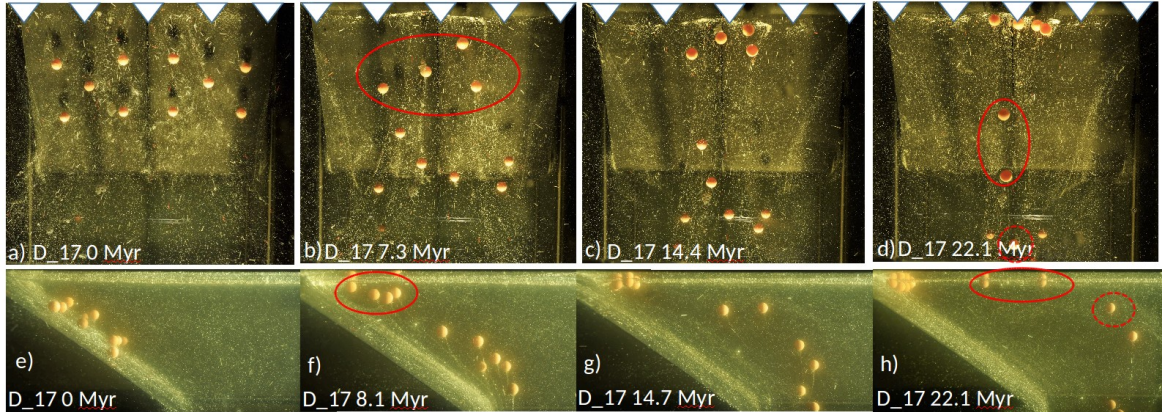


**Figure 12.** Map-view (a-d) and side-view (e-h) images of rigid diapirs (Case D\_17, Tables 1,2) rising into a mantle wedge flow responding to rollback subduction. Circulation now involves toroidal flow around the slab, from the ocean-side to wedge-side of the system (left to right). a) and e): Initial conditions for three rows of diapirs distributed in a trench-parallel orientation, in the velocity boundary layer above the sinking plate. Red circles in frames b-d, f-h highlight surfacing diapirs and locations of expected melt delivery to the base of the plate. Sub-arc patterns are similar to downdip-only cases, whereas rollback flow delivers rising diapirs towards the central, symmetry axis of the wedge. Surface melt delivery is linear in a trench-normal orientation near the end of the experiment (d and h).

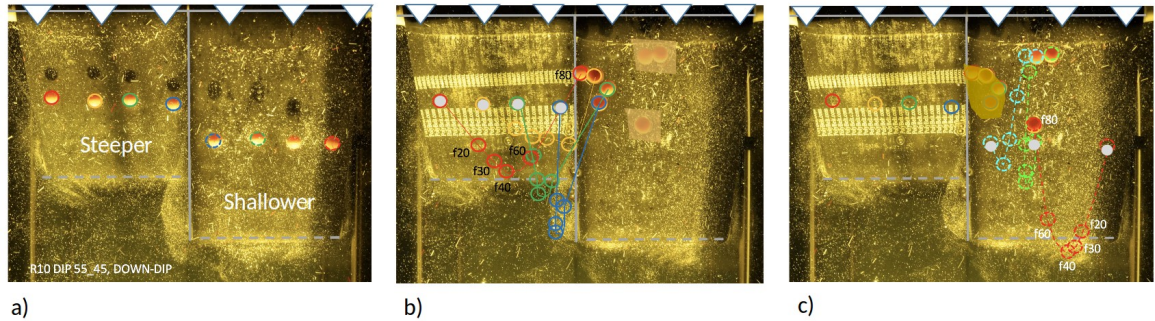
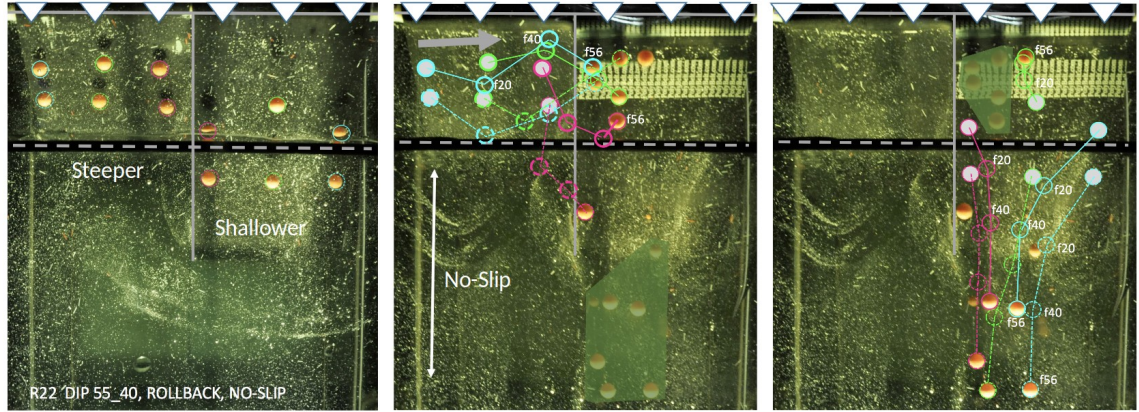


**Figure 13.** Sequence of map-view images from an experiment with downdip subduction with a gap between slab segments of  $55^\circ$  dip (left belt) and  $45^\circ$  (right belt) (Case D\_10, Tables 1,2) . a) The initial placement of rigid sphere diapirs is shown, where 4 diapirs are distributed in a trench-parallel orientation along each slab segment. As in prior cases, diapirs are initially placed in the VBL above the subducting plate. Colored circles are used to construct distinct diapir pathlines for those initiating above the steep belt (b) and shallow belt (c). (b) Patterns clearly show that flow/diapir transport is from the deep wedge above the steep slab segment to the sub-arc region above the inner edge of the shallow slab segment. c) Without rollback, diapirs sourced from the shallower slab also return to the sub-arc of this plate through curved ascent paths (1. slightly up and away from the trench, 2. near-vertical through mid-wedge, 3. strongly deflected sub-horizontal and toward the trench in shallow wedge). Grey shaded circles represent starting points along diapir particle paths. Trench location represented with white triangles. Frame numbers noted are 0, 20, 40, 60, and 80 corresponding to times of 0, 7.7, 15.5, 23.2, and 30.9 Myr respectively.



a) b) c)

**Figure 14.** Map-view images from experiment D\_22 including rollback subduction, a no-slip surface under the back-arc plate, and a gap between slab segments of  $55^\circ$  dip (left belt) and  $40^\circ$  (right belt). a) The initial placement of rigid sphere diapirs distributed in two rows in a trench-parallel orientation along each slab segment. (b) Patterns showing extreme trench-parallel focusing of steep plate diapirs toward the sub-arc region of the shallower plate. Start locations shown as shaded circles. Sense of strong trench-parallel flow is highlighted with gray arrow. c) With rollback, diapirs from the shallow slab are left behind by migrating trench/slab, and combine with toroidal flow to surface in a linear (trench-normal) pattern. Trench location represented with white triangles. Black line with white dashes shows location of back-arc ridge where Mylar is laid down at the trench migration rate to create a no-slip condition on horizontal surface velocity (on plot, region below the line, or beneath the back-arc section of plate). Frame numbers referenced are 0, 20, 40, 56 corresponding to times of 0, 7.5, 14.9, 20.9 Myr respectively.

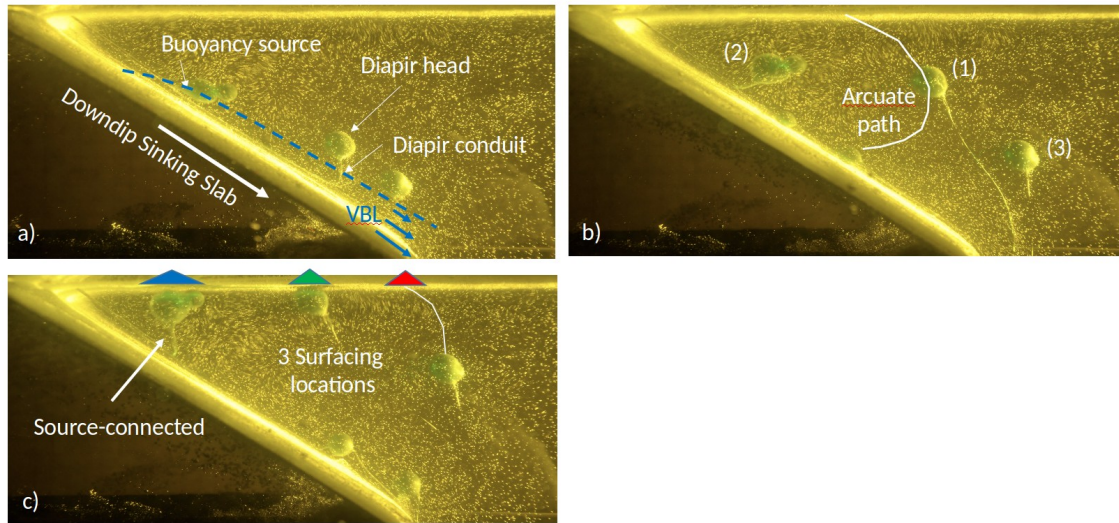


**Figure 15.** Cross-sectional image through wedge for case E\_13, with downdip-only subduction and diapirs of (dry) ethanol. a) (time 10 Myr) This frame shows typical examples of distinct diapirs evolving within the velocity boundary layer (VBL) above the slab. A single buoyancy source feeds a growing diapir head as it moves down-slab, trailing a narrow conduit structure that connects back to the source. b) (time 15.8 Myr) The diapirs exit the VBL and rise upward through the sluggish mid-wedge, along arcuate paths (first away from the trench, and then back towards the trench). Conduits trail behind the diapirs and can (1) be long and distended, (2) remain connected to the source or (3) be short and severed. c) (time 20 Myr) Despite constant buoyancy flux and simple downdip-only subduction, three different paths occur, with three different trench-normal surfacing distances ranging from sub-arc (blue triangle) to back-arc (red triangle).

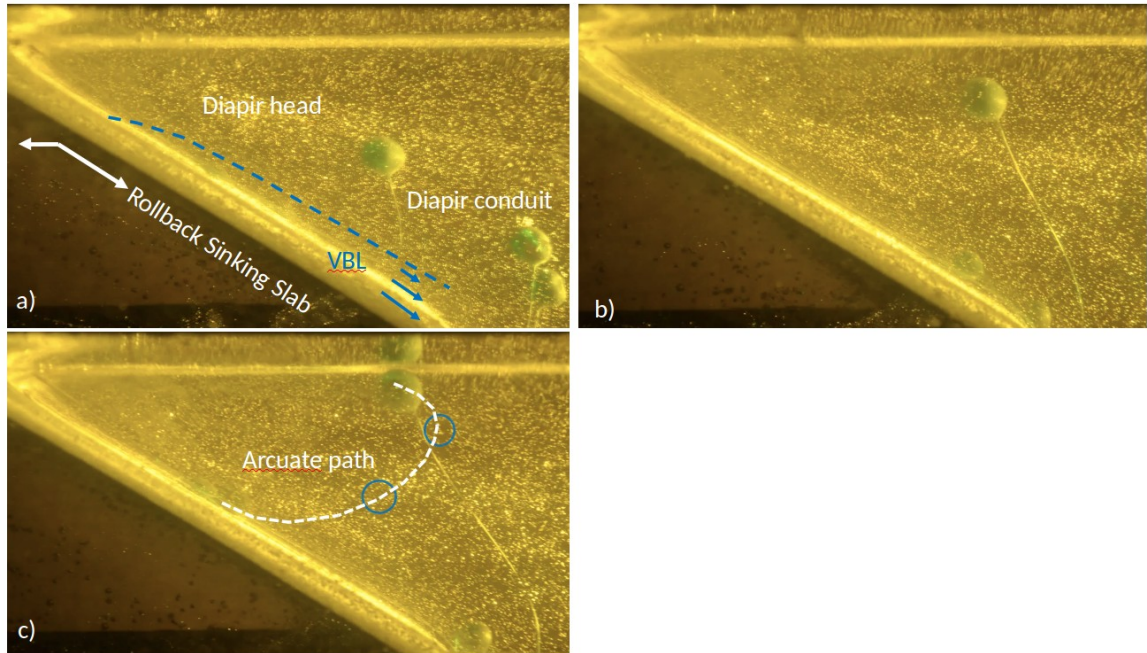


**Figure 16.** Similar cross-sectional image through wedge as Figure 15, but for case E\_14, with rollback subduction and diapirs of (dry) ethanol. a) Frame shows a diapir that has risen from VBL into the mid-wedge, with a trailing conduit that has severed from source region and two smaller unsuccessful diapirs being entrained out of the ROI. b) As the diapir rises through the mid-wedge, the tail is drawn downward with background flow and is severed from the source. c) The diapir head impacts the base of plate at an intermediate trench-normal distance. Times are a) 12.8 Myr, b) 16 Myr, c) 17.9 Myr.

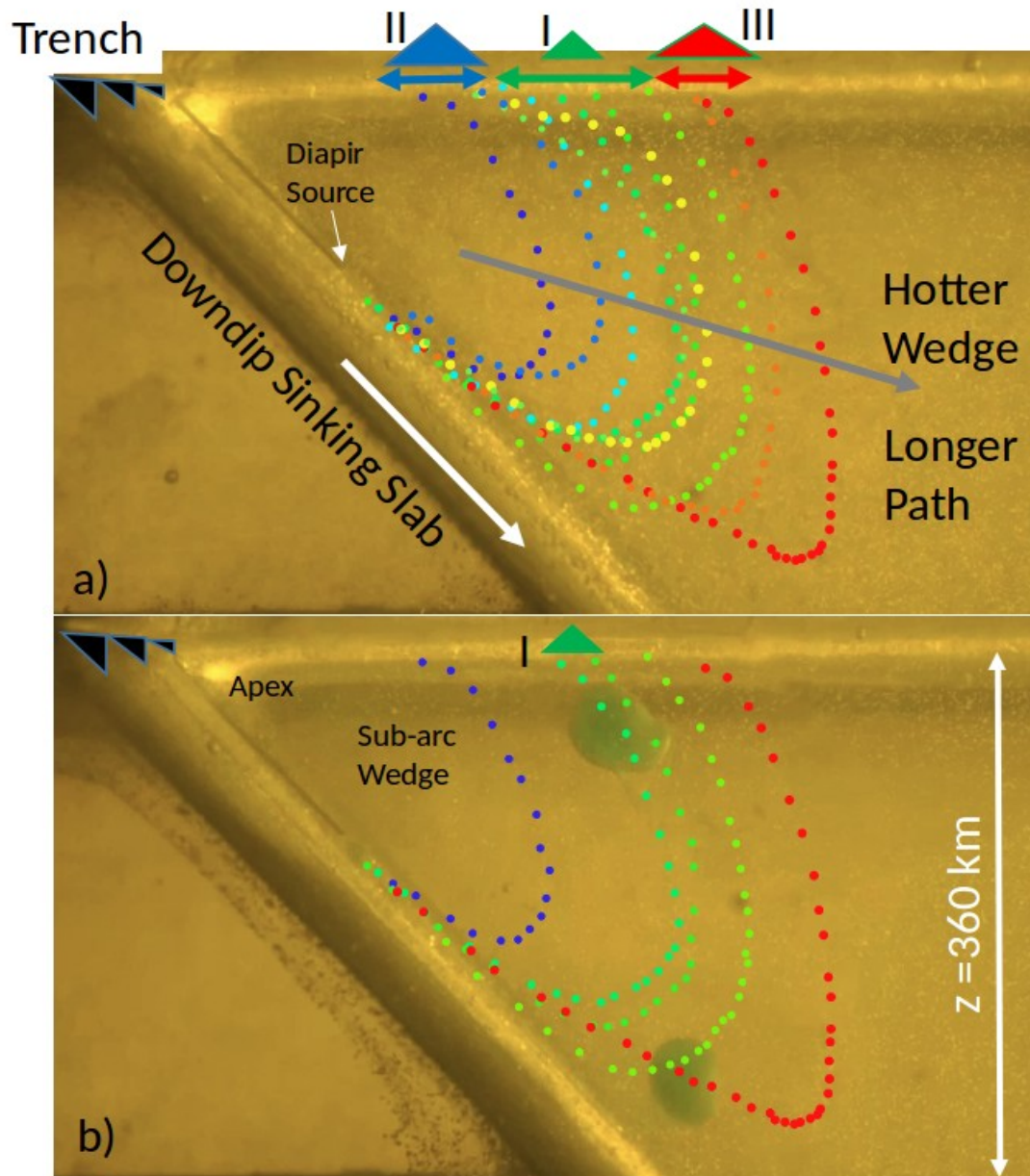


**Figure 17.** a) Cross-section through wedge for case E\_7 (ethanol-dry diapir, downdip-only slab, 45° dip, 1 diapir source). Lines marked by colored circles show digitized paths of diapirs sourced from the same location. Paths highlight the extreme range in path shapes/lengths through the wedge (heating) and surfacing locations (volcanic output), discussed as three ascent modes (I, II, III). b) Green paths represent spaced out diapirs lacking interaction with other buoyancy sources in the VBL or central wedge (Mode I). These intermediate surfacing locations range are ~350 km from trench. Mode II (blue) and Mode III type diapir paths are shown in subsequent figures.

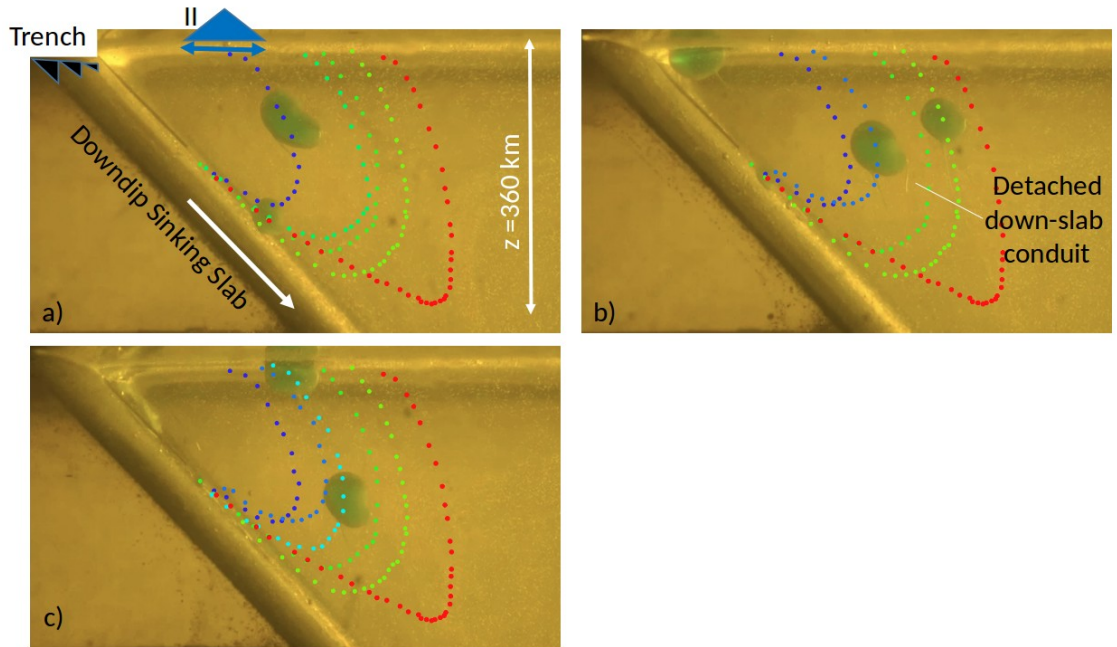


**Figure 18.** Cross-sections with diapir paths for case E\_7 as in Figure 14. (ethanol-dry diapir, downdip-only slab,  $45^\circ$  dip, 1 diapir source) highlighting a second mode of evolution/ascent. Paths are shown in blue for three distinct Mode II diapirs. These upwellings have received buoyant fluid from both up-slab and down-slab conduits while in the VBL, achieving a larger volume and rise velocity. Surfacing locations are  $\sim 150$  km closer to the trench than Mode I (green paths shown for reference). A remnant down-slab conduit is seen as a bright tail in (b), trailing the second high volume (Mode II) diapir to surface in this E7 experiment.

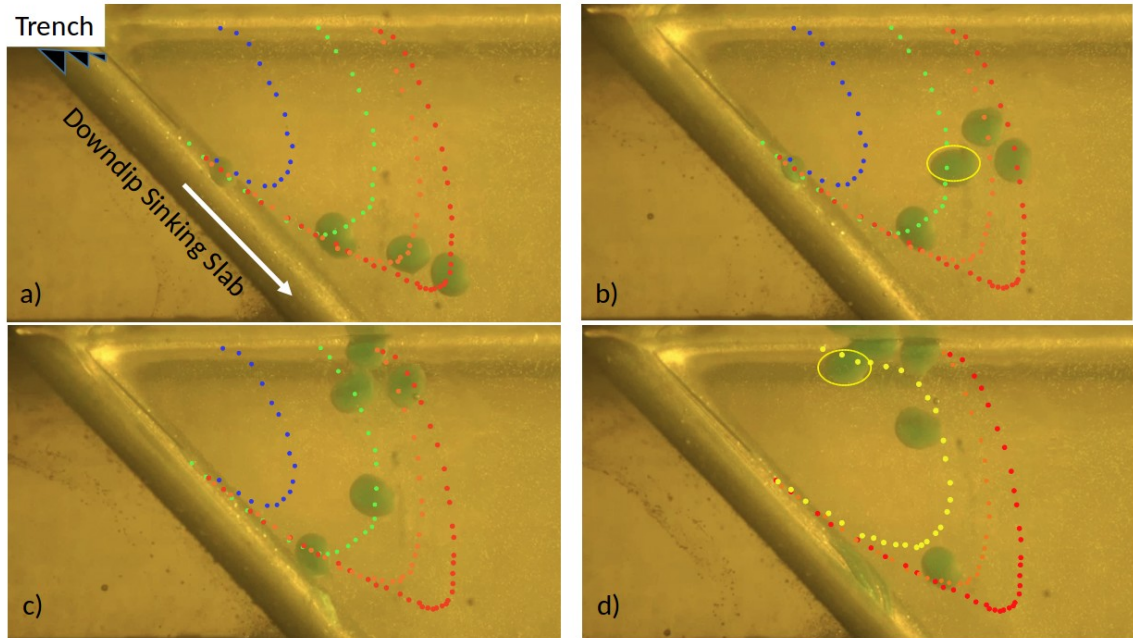


**Figure 19.** a) Cross-section through wedge for case E7 as in figures 17 and 18 highlighting the third mode of diapir interaction/ascent from slab to surface (shown as red circle paths). a) A repeatable pattern in these cases is that small diapirs separate more slowly from the VBL, and are dragged deeper into the system. Single diapirs stall here, where upward buoyancy balances downward drag. b) Accumulated smaller diapirs rise together at a greater ascent rate, along nearly vertical paths. c) Diapir clumps surface at the greatest distance from the trench,  $\sim 75$  km further from the trench than reference (green Mode I) non-interacting diapirs. d) An interesting (repeatable) result is that inner diapirs in the clump can be delayed in surfacing (yellow path) by being held beneath their partners.

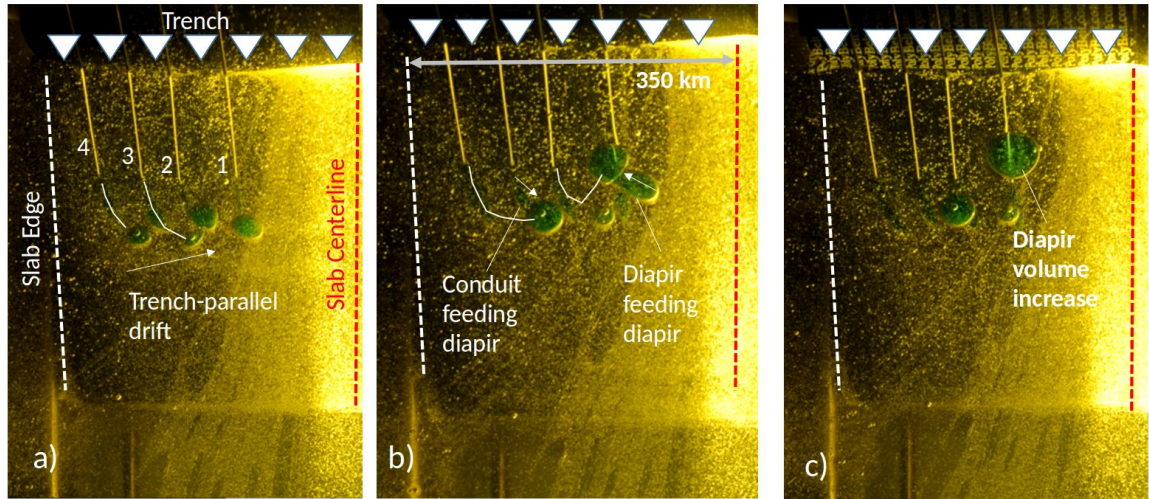


**Figure 20.** Map-view images from experiment V\_7 (downdip-only subduction), using vodka as the diapir fluid, that allows for merging of distinct flow structures. Four diapir sources are modeled, with identical constant buoyancy fluxes, and are labeled in panel (a) (1: mid-slab – 4. slab-edge). Frames cropped to focus on the southern slab segment. a) In 3-D experiment, even simple downdip-only subduction generates wedge flow (above the VBL) with a trench-parallel component that carries material from the slab edge towards the wedge centerline (see Figure 9). b) Diapirs moving in the trench-parallel direction interact with new buoyancy sources. c) In the 5 second (167 kyr) interval between frames the deeper diapir from source 4 merges upward into the shallower diapir from source 3. Volume and rise rate increase markedly and ascent becomes near vertical.

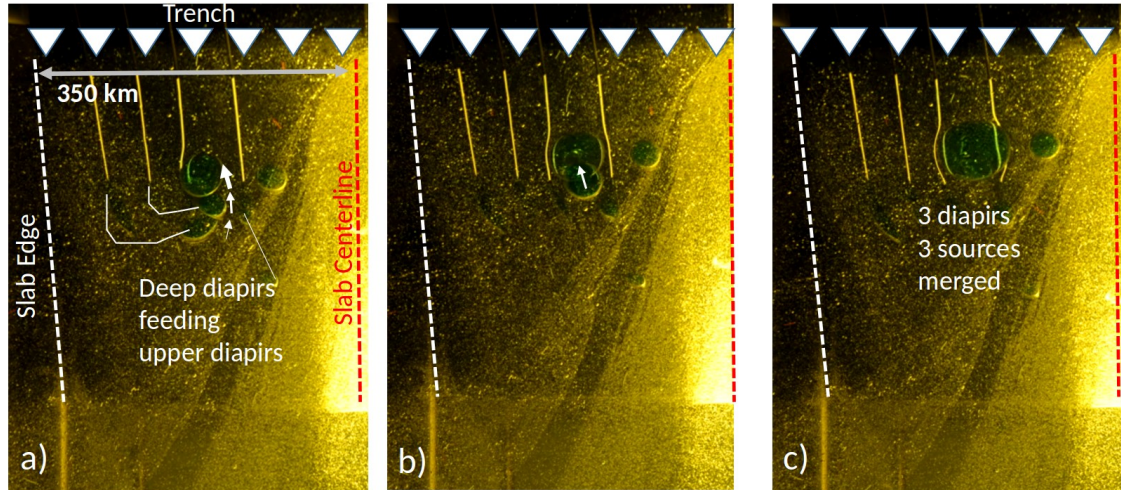


**Figure 21.** Map-view images from experiment V\_7 (downdip-only subduction), using vodka as the diapir fluid, that allows for merging of distinct flow structures. a) Trench-parallel drift of diapirs from different source locations produces a vertically aligned column of diapirs originating from three different source locations. b) In the 5 seconds (167 kyr) between images, the deepest diapir from source 4 has merged upwards into the mid-level diapir from source 3. c) In the 5 second (167 kyr) interval between subsequent frames the newly enlarged combined mid-level diapir accelerates and merges upward into the diapir from source 2 making one high-volume near-surface diapir containing material from sources 4, 3, and 2.

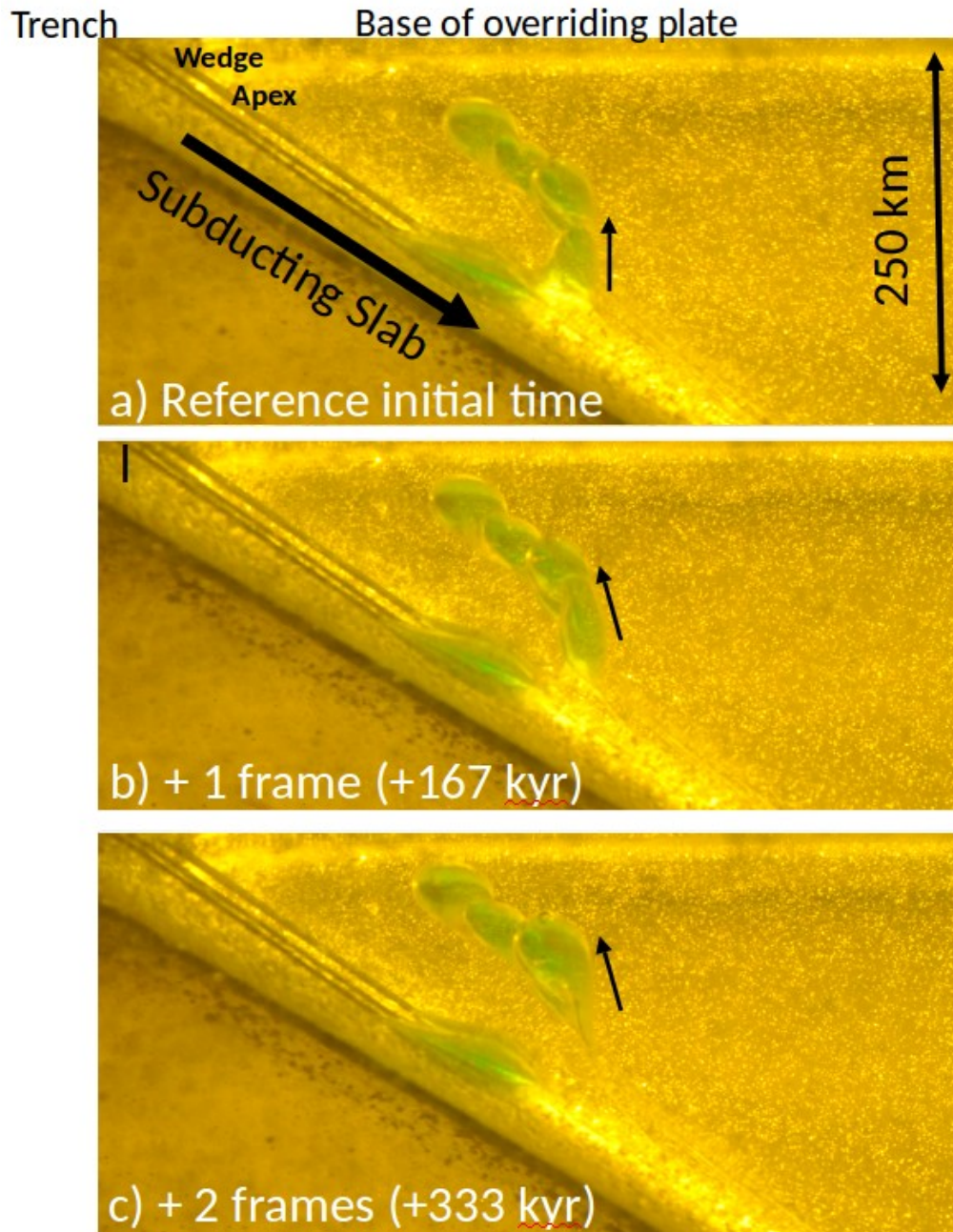


**Figure 22.** Side-view, trench-normal cross-sections through the wedge for experiment V\_7 (downdip subduction, 4 vodka sources). a) Three distinct diapirs have moved into the mid-wedge, where they drift with a trench-parallel component of motion (into the page). b) One time-step later a deeper diapir from a different source is moving upward and into the page through the tail of the overriding diapir. c) Five seconds further in time the two diapirs have fully merged.

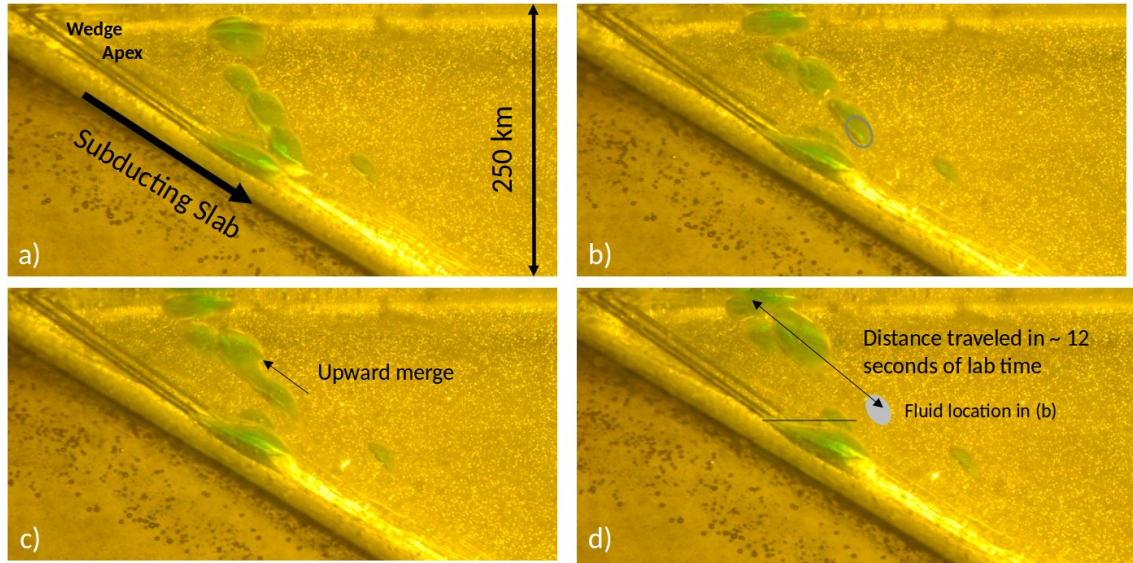


**Figure 23.** Side-view, trench-normal cross-sections through the wedge for experiment V\_7 (down-dip subduction, 4 vodka sources). a) An array of diapirs are evolving at different trench-parallel locations (into the page). b) Deep diapir fluid encounters a conduit structure and begins rapid ascent. c) Five seconds (167 kyr) further in experiment time, the deeper is merging upward into the shallower diapir originating from one source closer to the centerline. c) After another five second (167 kyr) time-step, the newly merged diapir is beginning to merge upwards into the stalled diapir above. The deeper diapir fluid from (b) transits ~200km in 0.4 Ma, 12 seconds of lab time, yielding an average rise rate of 50 km / 100 kyr.

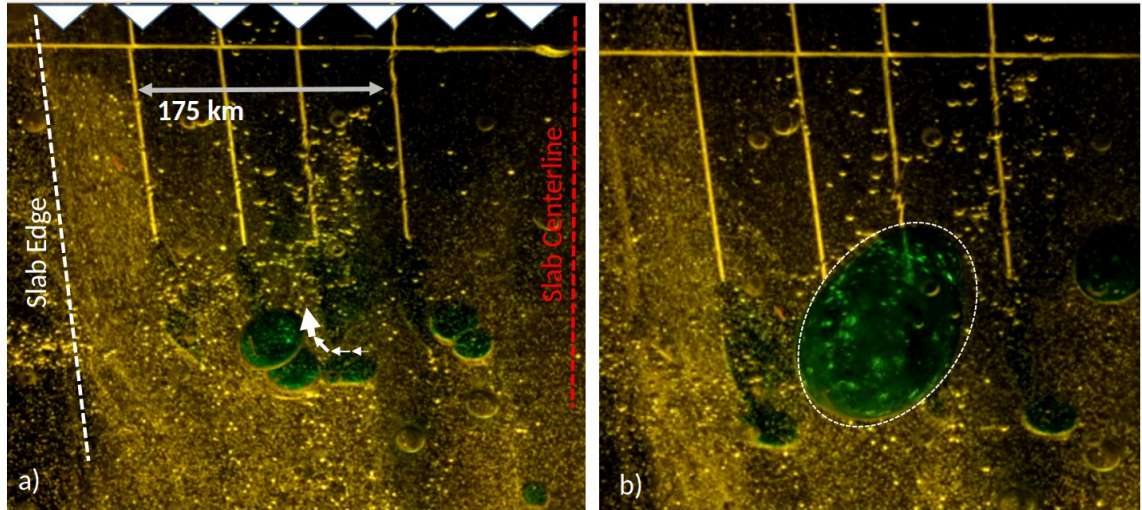


**Figure 24.** Map-view images from experiment V\_9 (downdip subduction,  $35^\circ$  dip, 4 vodka diapir fluid sources, fixed upper surface). a) Dramatic example of rapid vertical transport due to 3-D vertical shear in wedge combining with vertically rising diapirs to produce vertical columns of buoyant morphologies that are able to merge and nearly connect source to surface. Here fluid at the base of the wedge in the VBL is feeling diapirs passing overhead and about to merge upwards. b) In 25 seconds of elapsed experiment time (1.7 Myr), the fluid from all depths in the wedge is merged into a near-surface patch of diapir fluid trapped beneath the overriding plate.

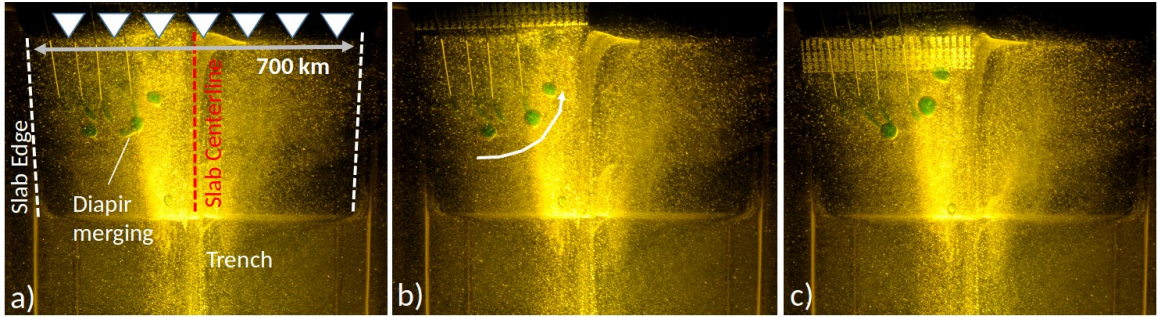


**Figure 25.** Map-view images from experiment V\_8 (rollback subduction,  $35^\circ$  dip, 4 vodka diapir fluid sources, free surface boundary). The interaction scenarios are a complex balance of downward entrainment in the VBL and advection with the slab, vertical rise due to buoyancy flux and trench-parallel drift due to three-dimensionality of mid- to shallow-wedge return flow towards the sub-arc wedge apex and slab centerline. a) The middle of the three established diapirs is still connected to source 1, growing and taking in fluid from below. b-c) Three distinct diapirs are fully detached from their respective sources and are advected towards the wedge apex without further interacting with deeper diapir fluid.

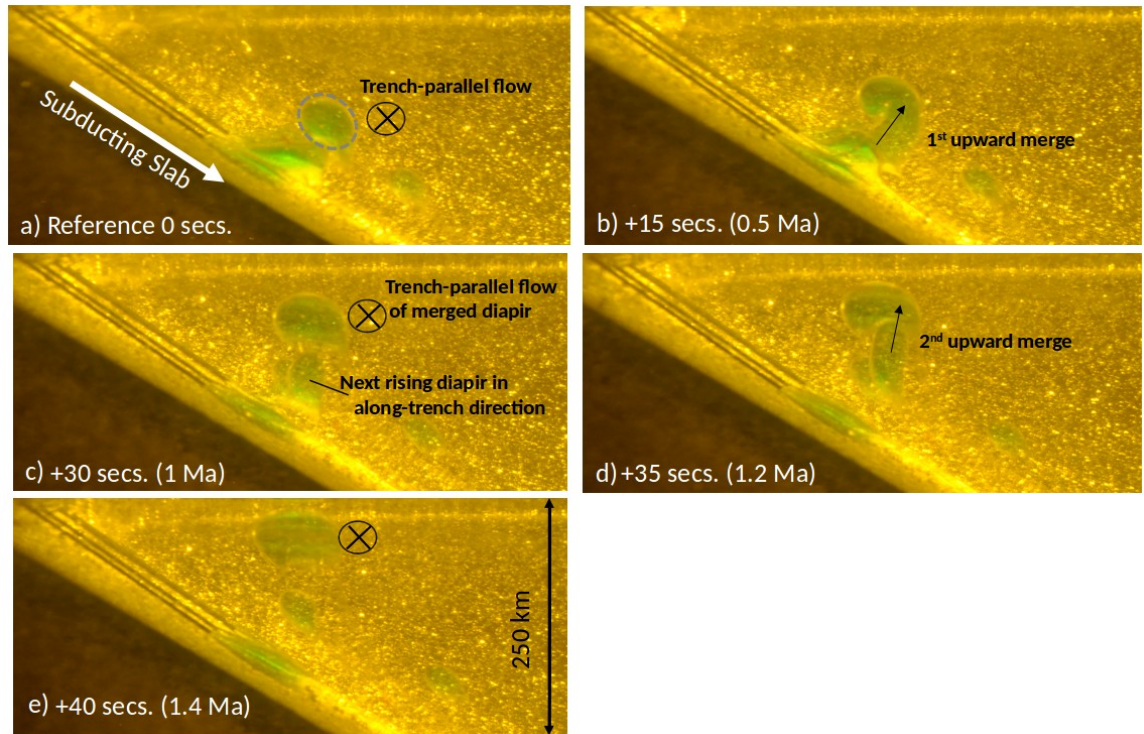


**Figure 26.** Side-view, trench-normal cross-sections through the wedge for experiment V\_8 (rollback subduction, 4 vodka sources, free surface). Example of shallower diapir moving with strong trench-parallel motion and interacting with multiple, deeper diapirs arrayed along-strike. a) Mid-level diapir (outlined) is moving into page. b) (15 seconds elapsed from frame a) Deeper, growing diapir in VBL moves rapidly upward into overlying diapir. c) (15 seconds elapsed from frame b) The mid-level feature has moved in a trench-parallel direction over the next deep growing diapir (outlined). d) (5 seconds elapsed from frame c) Deeper buoyant fluid has begun rapid upward assimilation into overlying feature. e) Large volume diapir is impacting underside of plate after accumulating deep fluid from multiple sources in ~200 km of along-trench motion.

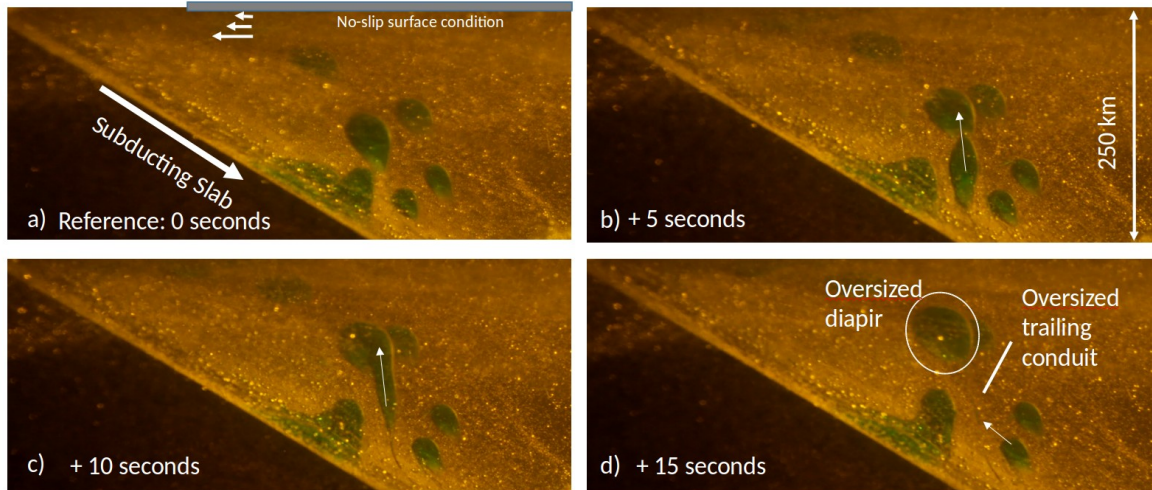


**Figure 27.** Side-view, trench-normal cross-sections through the wedge for experiment V\_10 (rollback subduction, 4 vodka sources, no-slip overriding, back-arc plate). a) An array of diapirs are evolving at different trench-parallel locations. The presence of a no-slip condition under the back-arc plate causes return flow pathways to deepen in the wedge. b-c) Deep diapir fluid encounters a conduit structure and begins ascent, assimilating into overlying diapir. d) The large volume diapir develops a larger ascent velocity. An enhanced trailing conduit provides a drifting pathway for much deeper fluid to ascend to the surface rapidly (~200 km in ~0.3 Ma (5-10 seconds)).

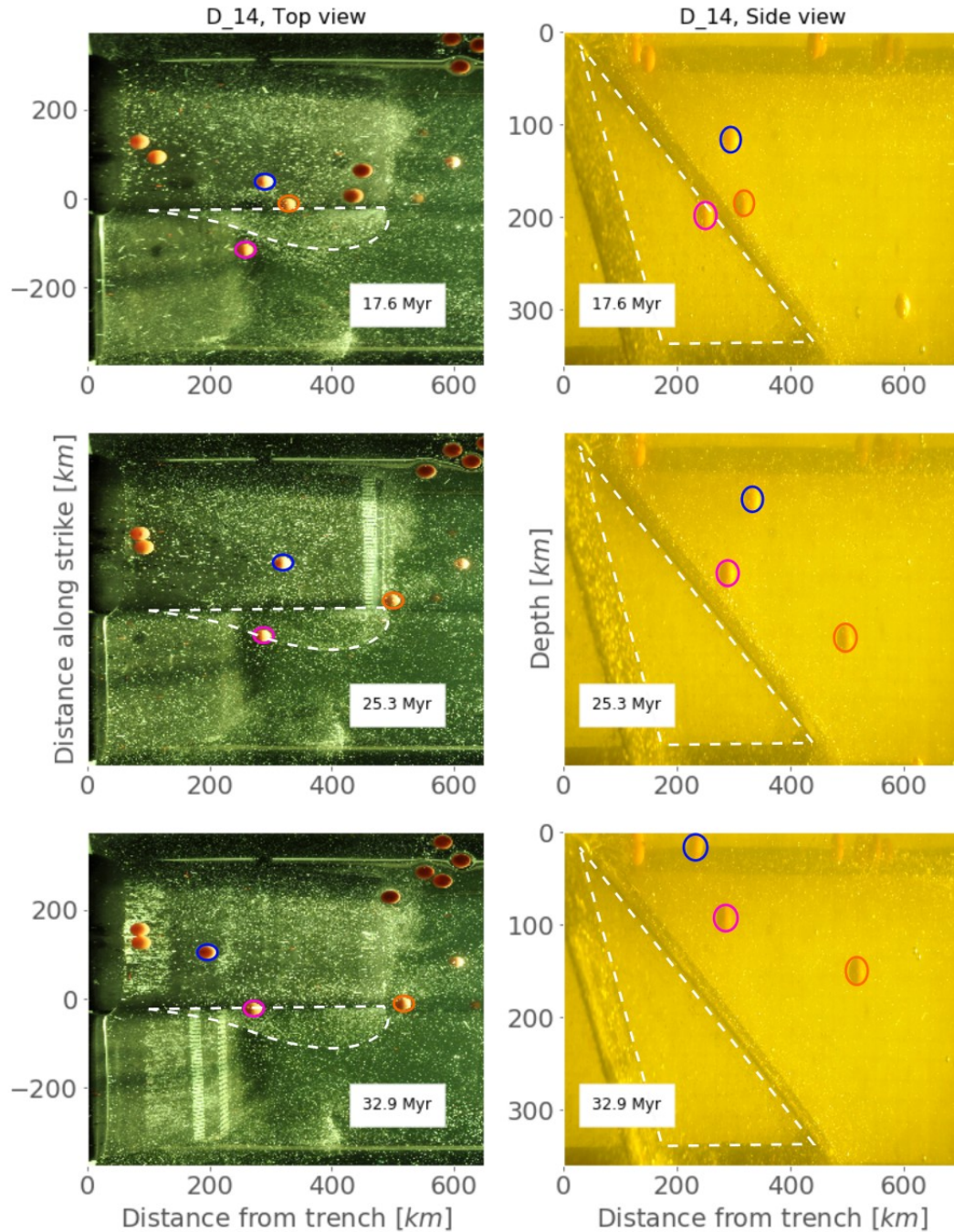


**Figure 28.** Multiple still frames from experiment D\_14, left panels are top view and right panels are side view. The diapir highlighted in magenta moved very slowly during this part of the experiment translating and rising only  $\sim 100$  km over 15.3 Myr shown here, while its neighbors highlighted in blue and orange were advected much farther. This is because of the interaction of the magenta diapir and the pocket of material being extruded from between the opening slab tear (white dashed region).

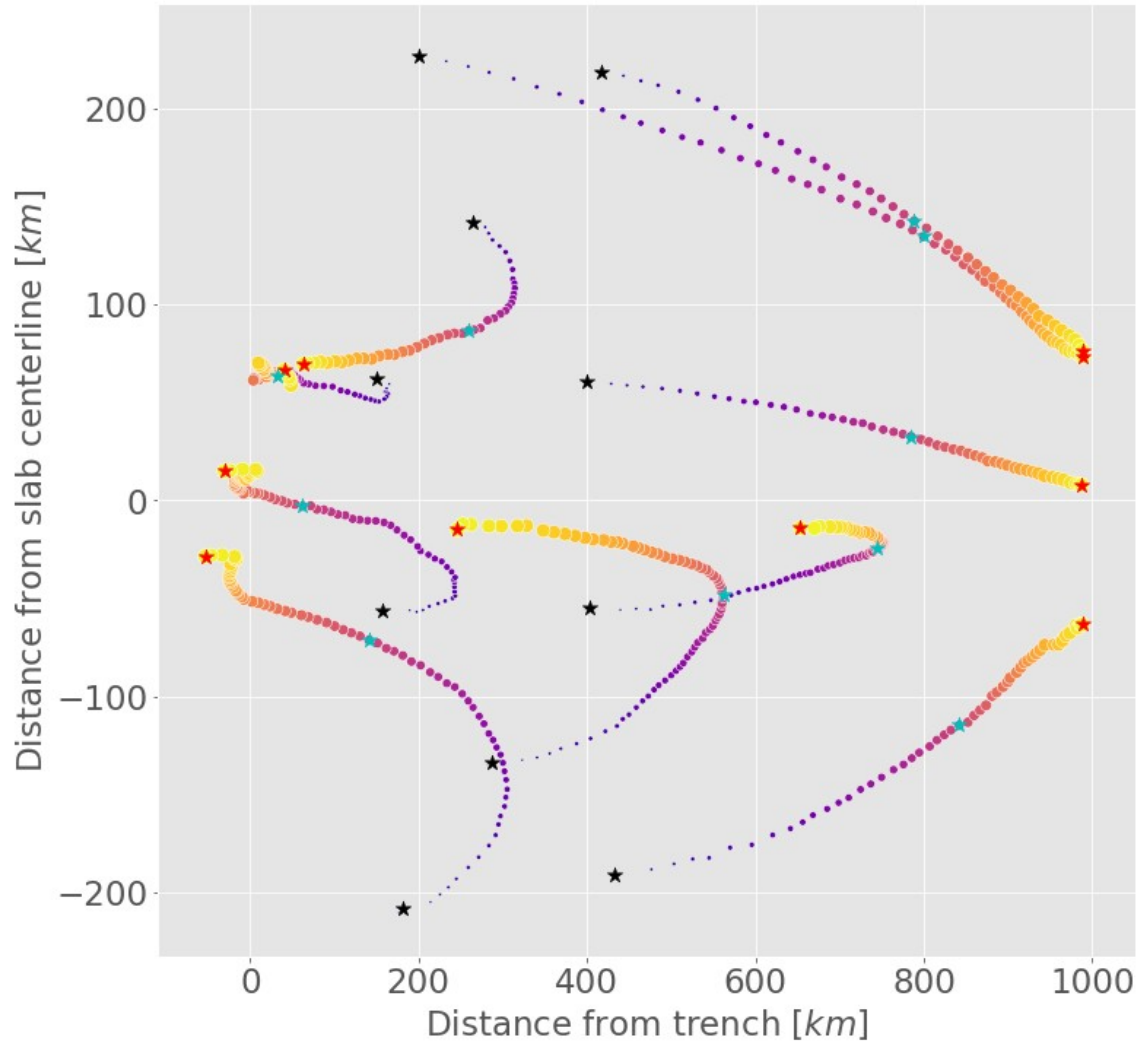


**Figure 29.** Map-view plot of along-strike transport paths and diapir positions relative to the trench. Markers are colored and sized by time. Spacing between markers is indicative of translational velocity (farther = faster). Black stars mark initial positions of rigid spheres at the slab-wedge interface, cyan stars mark position halfway along path, and red stars indicate final surfacing position. Note greater velocities at depth while diapirs are proximal to the kinematic forcing of the slab, and increased along-strike displacements for diapirs originating farther from the slab centerline. 4 diapirs surfaced along the centerline but took very different paths to get there.

**Table 1** – Listing of experimental parameters

Experiment phase and diapir type	Exp. Name	Duration min (Myr)	Covergence rate, Ud cm/min (km/Myr), North / South	Slab Dip degrees, North / South	Subduction zone thermal model	Surface Boundary	
1.) Arrays of rigid spheres	D_10	17 (34)	7 (105) / 7(105)	45 / 54	North / South	free	
	D_11	14 (28)	7 (105) / 7(105)	37 / 37	Central Honshu	free	
	D_14	22 (44)	7 (105) / 8 (120)	37 / 37-65	antral Honshu / North Philippines	free	
	D_15	17 (34)	6 (90) / 6 (90)	37 / 37	Central Honshu	free	
	D_16	15 (30)	6 (90) / 6 (90)	37 / 37	Central Honshu	free	
	D_17	14 (28)	6 (90) / 6 (90)	37 / 37	Central Honshu	free	
	D_18	10 (20)	6 (90) / 6 (90)	37 / 49	Central Honshu / South Kurile	free	
	D_19	12 (24)	6 (90) / 6 (90)	37 / 49	Central Honshu / South Kurile	free	
	D_20	15 (30)	6 (90) / 6 (90)	56 / 56	North Philippines	free	
	D_21	14 (28)	6 (90) / 6 (90)	56 / 56	North Philippines	fixed	
	D_22	11 (22)	6 (90) / 6 (90)	39 / 56	antral Honshu / North Philippines	fixed	
	D_29	8 (16)	7 (105) / 7(105)	32 / 32	Central Honshu	free	
	D_30	7 (14)	7 (105) / 7(105)	32 / 32	Central Honshu	free	
	2.) Single injection point source	A_5	9 (18)	7 (105) / 7(105)	35 / 35	Central Honshu	free
		A_8	7 (14)	7 (105) / 7(105)	35 / 35	Central Honshu	free
	3.) Multiple injection point sources	E_6	15 (30)	6 (90) / 6 (90)	45 / 45	South Kurile	free
		E_7	37 (74)	6 (90) / 6 (90)	45 / 45	South Kurile	free
		E_9	13 (26)	6 (90) / 6 (90)	45 / 45	South Kurile	free
		E_10	13 (26)	6 (90) / 6 (90)	45 / 45	South Kurile	free
		V_3	15 (30)	7 (105) / 7(105)	35 / 35	Central Honshu	free
V_4		14 (28)	7 (105) / 7(105)	35 / 35	Central Honshu	free	
E_13		10 (20)	6 (90) / 6 (90)	35 / 35	Central Honshu	free	
E_14		20 (40)	6 (90) / 6 (90)	35 / 35	Central Honshu	free	
V_5		15 (30)	6 (90) / 6 (90)	35 / 35	Central Honshu	free	
V_6		17 (34)	6 (90) / 6 (90)	35 / 35	Central Honshu	free	
V_7	17 (34)	6 (90) / 6 (90)	35 / 35	Central Honshu	free		
V_8	17 (34)	6 (90) / 6 (90)	35 / 35	Central Honshu	free		
V_9	32 (64)	6 (90) / 6 (90)	35 / 35	Central Honshu	fixed		
V_10	20 (40)	6 (90) / 6 (90)	35 / 35	Central Honshu	fixed		

**Table 2 – Summary of measured experimental outcomes**

Experiment phase and diapir type	Exp. Name	Diapir Radius cm (km)	Diapir Density km/m <sup>3</sup> (normalized to matrix)	Diapir Success Ratio N successful / N total	Avg. Path length cm (km)	Residence time min (Myr)	Trench migration rate, Ut cm/min (km/Myr)	Ut/ Ud	Trench displacement cm (km)
1.) Arrays of rigid spheres									
Solid	D_10	0.5 (15)	508 (0.64)	7/8	6.17 (185.1)	11.69 (23.4)			
Solid	D_11	0.5 (15)	508 (0.64)	7/8	6.37 (191.1)	10.27 (20.5)			
Solid	D_14	0.5 (15)	508 (0.64)	5/8	5.99 (179.6)	10.39 (20.8)			
Solid	D_15	0.5 (15)	508 (0.64)	12/12	5.23 (156.9)	9.67 (19.3)			
Solid	D_16	0.5 (15)	508 (0.64)	11/12	5.11 (153.4)	8.58 (17.2)			
Solid	D_17	0.5 (15)	508 (0.64)	8/10	6.03 (180.9)	7.88 (15.8)	1.76 (26.4)	3.40	17.6 (528)
Solid	D_18	0.5 (15)	508 (0.64)	9/12	5.17 (155.2)	7.56 (15.1)	1.76 (26.4)	3.40	15.6 (468)
Solid	D_19	0.5 (15)	508 (0.64)	12/12	5.72 (171.6)	8.39 (16.8)	1.76 (26.4)	3.40	17.5 (525)
Solid	D_20	0.5 (15)	508 (0.64)	9/12	4.41 (132.4)	9.40 (18.8)	1.76 (26.4)	3.40	22.7 (681)
Solid	D_21	0.5 (15)	508 (0.64)	11/12	5.49 (164.6)	9.72 (19.4)	1.76 (26.4)	3.40	23.5 (705)
Solid	D_22	0.5 (15)	508 (0.64)	11/12	5.52 (165.6)	7.38 (14.8)	1.76 (26.4)	3.40	18.4 (552)
Solid	D_29	0.62 (18.6)	103 (0.93)	4/4	5.09 (152.8)	5.83 (11.7)			
Solid	D_30	0.62 (18.6)	103 (0.93)	4/4	6.71 (201.2)	5.50 (11.0)	2.35 (35.25)	2.98	13.5 (405)
2.) Single injection point source									
Air	A_5	0.40 (12)	1.18 (0.99)	19/19	3.98 (119.5)	4.92 (9.8)			
Air	A_8	0.45 (13.5)	1.18 (0.99)	27/27	3.76 (112.7)	4.68 (9.4)			
Ethanol (dry)	E_6	0.75 (22.5)	798 (0.44)	3/4	9.76 (292.7)	7.67 (15.3)			
Ethanol (dry)	E_7	0.87 (26.25)	798 (0.44)	12/12	10.06 (301.9)	7.00 (14.0)			
Ethanol (dry)	E_9	1.00 (30)	798 (0.44)	3/3	2.53 (75.9)	4.17 (8.3)	2.35 (35.25)	2.55	13.6 (408)
Ethanol (dry)	E_10	0.75 (22.5)	798 (0.44)	3/3	3.76 (112.6)	4.47 (8.9)	2.35 (35.25)	2.55	26 (780)
Ethanol (wet)	V_3	1.03 (30.9)	916 (0.36)	6/6	6.73 (201.9)	4.28 (8.6)			
Ethanol (wet)	V_4	0.80 (24)	916 (0.36)	8/9	5.57 (167.2)	2.65 (5.3)			
3.) Multiple injection point sources									
Ethanol (dry)	E_13	0.88 (26.4)	798 (0.44)	3/5	4.82 (144.7)	3.49 (7.0)			N injectors 3
Ethanol (dry)	E_14	0.72 (21.6)	798 (0.44)	5/11	4.06 (121.8)	2.82 (5.6)	2.35 (35.25)	3.40	27.5 (825)
Ethanol (wet)	V_5	0.58 (17.8)	916 (0.36)	9/11	4.77 (143.2)	4.94 (9.9)			4
Ethanol (wet)	V_6	0.55 (16.5)	916 (0.36)	21/21	4.56 (136.8)	4.62 (9.3)	2.35 (35.25)	2.55	24 (720)
Ethanol (wet)	V_7	0.68 (20.4)	916 (0.36)	16/18	4.67 (140.2)	4.99 (10.0)			4
Ethanol (wet)	V_8	0.70 (21.0)	916 (0.36)	15/16	4.17 (125.4)	3.87 (7.7)	2.35 (35.25)	2.55	31 (930)
Ethanol (wet)	V_9	0.79 (23.6)	916 (0.36)	13/13	8.16 (244.8)	7.26 (14.5)			4
Ethanol (wet)	V_10	0.59 (17.8)	916 (0.36)	32/37	5.46 (163.8)	4.44 (8.9)	1.76 (26.4)	3.40	24.5 (735)

## APPENDIX 1

### Air Diapirs

Another buoyant diapir fluid was tested but not reported in the main text, air (Figure 4). Air was chosen as an extremely buoyant end-member in an attempt to produce vertical ascent paths. We injected air using the same single syringe pump application as in phase two of the single point source dry ethanol cases. Because the density contrast between air and the working fluid is nearly 100% it was thought to be able to facilitate rapid vertical ascent through the wedge and interact minimally with the creeping flow. This was not the case, as presented in the subsequent figures, and air diapirs were also highly deflected away from the trench downdip within the VBL (Figure A1.1). Air diapirs also exhibited coalescing behavior where multiple individuals would merge and the collective buoyancy would increase dramatically (Figure A1.2). This fluid did however produce the most consistent paths, forming nearly continuous chains of diapirs ascending from the source to the surface occupying all three regimes of wedge flow contemporaneously and spaced with a regularity in space and time not observed in any of the other experiments (Figure A1.3). These experiments were successful in demonstrating that even for extreme buoyancy fluxes vertical ascent is difficult to produce without incorporating some rheological weakening mechanism of the ambient fluid through which the diapirs ascend.

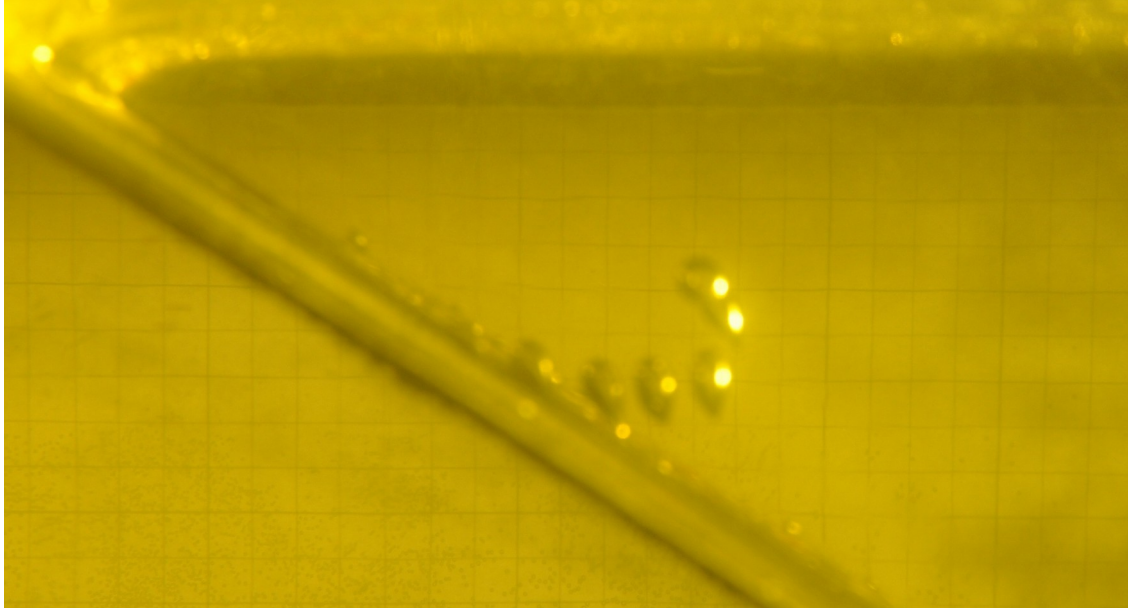


**Figure A1.1.** Cross-sectional side-view from experiment A\_5 (Tables 1 and 2) at time 9.9 Myr showcasing the entrainment of these highly buoyant diapirs within the VBL above the subducting slab before detaching downdip of the injection point source. This frame also demonstrates the highly regular timing and spacing of air diapirs compared with other fluids tested.

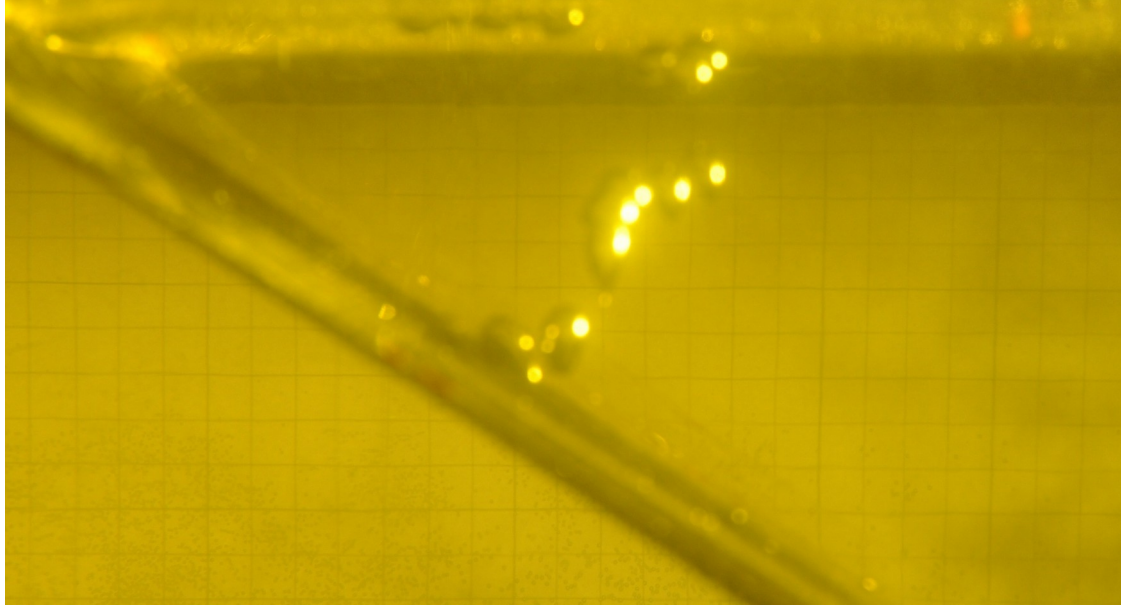


**Figure A1.2.** Cross-sectional side-view frame from experiment A\_5 at time 14.8 Myr showing a group of three subsequent air diapirs merging, accelerating, and straightening their path making the ascent more vertical.

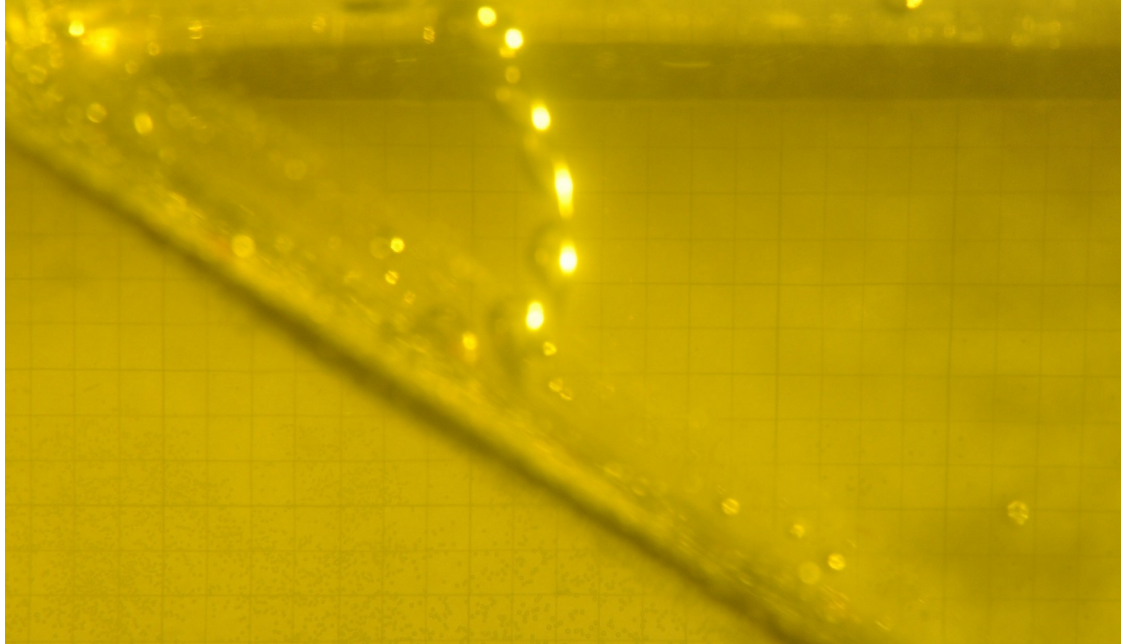


**Figure A1.3.** Cross-sectional side-view image from experiment A\_8 at time 4.9 Myr highlighting the regularity in air diapir timing and spacing. These diapirs form a nearly continuous chain from source to surface occupying the entire mantle wedge, giving a sense for the displacement these diapirs experience in each of the three wedge flow regimes. Diapirs in this experiment surfaced nearly vertically above the source, but were still deflected ~70 km away from the trench before entering the wedge apex return flow.

## APPENDIX 2

### Diapir Thermal Model

A key aspect to mass transfer through subduction zones is the thermal evolution of the material as it moves from the slab surface to the Earth's surface. In our experiments the positions of all buoyant features are recorded through space and time. Laboratory-derived diapir transit paths are then superimposed onto the 2D wedge thermal fields from the global compilation of [van Keken *et al.*, 2011] that most closely match the geometry and convergence rates from our experiments (Figures A2.1 and A2.2). These thermal diapir paths are then used as forcing for a 2D axisymmetric advection-diffusion model of an idealized spherical diapir with and without internal diapir flow to examine the thermal evolution of individual diapirs.

We chose a subset of observed laboratory diapir paths to force the boundaries of a 2D diapir heat model. The results from two end-member modeling runs are presented and compared, a short fast diapir path and a long slow diapir path. Final states for the two diapir end members are shown in Figure A2.5 with their accompanying temperature-time curves in Figure A2.3. All modeling runs are initialized with matrix and diapir temperatures equal to the slab surface temperature. When internal flow is included heat is mixed around the inside of the diapir and the central temperature changes faster than for conduction only cases (Figure A2.6). Regardless of whether internal flow is included both the short-fast and long-slow diapirs achieve internal temperatures in excess of 1200 degrees, hotter than the wet peridotite solidus and melting is expected to initiate before arriving at the LAB.

A 2D advection-diffusion model of a spherical diapir with axial symmetry is forced at the boundaries by the lab-derived vertical velocity-temperature-time pathways to inspect the internal thermal evolution of an initially cold chemically buoyant diapir. This modeling is evaluated using 2D thermal models because 3D wedge temperature fields for experimental subduction geometries and convergence rates are not known to this author. This numerical model solves a dimensional temperature equation (eq. A1) for the thermal field using an explicit forward Euler finite difference formulation.

$$\text{eq. A1} - \frac{DT}{Dt} + U_x \frac{dT}{dx} + U_y \frac{dT}{dy} = \kappa \left( \frac{dT}{dx^2} + \frac{dT}{dy^2} \right)$$

<i>Variable</i>	<i>T</i>	<i>t</i>	<i>U<sub>x</sub></i>	<i>U<sub>y</sub></i>	<i>κ</i>
<i>Definition</i>	<i>Temperature</i>	<i>Time</i>	<i>Horizontal velocity component</i>	<i>Vertical velocity component</i>	<i>Thermal conductivity</i>

An internal diapir flow field is computed after the analytical modified Stoke's flow solutions of [Hadamard, 1911] and [Rybczyński, 1911]. The model domain is 20 [km] x 20 [km] with 165 x 165 standard A-grid nodes [Arakawa and Lamb, 1977] that solve for temperature after operator splitting is employed to first advect and then diffuse the temperature field at each time step. The internal flow is driven solely by the coupling of the internal and external fluids at the material interface and scales linearly with the external free stream velocity, so is scaled by the known vertical velocity from the lab trajectories. Numerical experiments were computed in two ways: 1) with internal flow and advection of heat included and 2) with conductive heat transfer only and no internal circulation.

This modeling effort helped gain further understanding at first order of the internal temperature structure and thermal evolution of a diapir and its potential for melting along the observed trajectories. Diapirs traversing the wedge gain enough heat from the surrounding mantle to raise their internal temperature above the wet peridotite solidus for both solid conductive heating and internal flow calculations. We employed a novel approach to modeling the thermal evolution of compositionally buoyant diapirs numerically. This effort shows that even large or fast diapirs absorb an appreciable amount of heat as they transit the wedge and internal temperatures surpass the wet peridotite solidus before arriving at the LAB.

### References

- Arakawa, A., and V. R. Lamb (1977), Computational design of the basic dynamical processes of the UCLA general circulation model, *Methods Comput. Phys.*, *17*, 173–265.
- Hadamard, J. S. (1911), Motion of liquid drops (viscous), *Comp. Rend. Acad. Sci. Paris*, *154*, 1735–1755.
- van Keken, P. E., B. R. Hacker, E. M. Syracuse, and G. A. Abers (2011), Subduction factory: 4. Depth-dependent flux of H<sub>2</sub>O from subducting slabs worldwide, *J. Geophys. Res.*, *116*(B1), B01401, doi:10.1029/2010JB007922.
- Rybczyński, W. (1911), *Über die fortschreitende Bewegung einer flüssigen Kugel in einem zähen Medium*, Akademia Umiejętności.

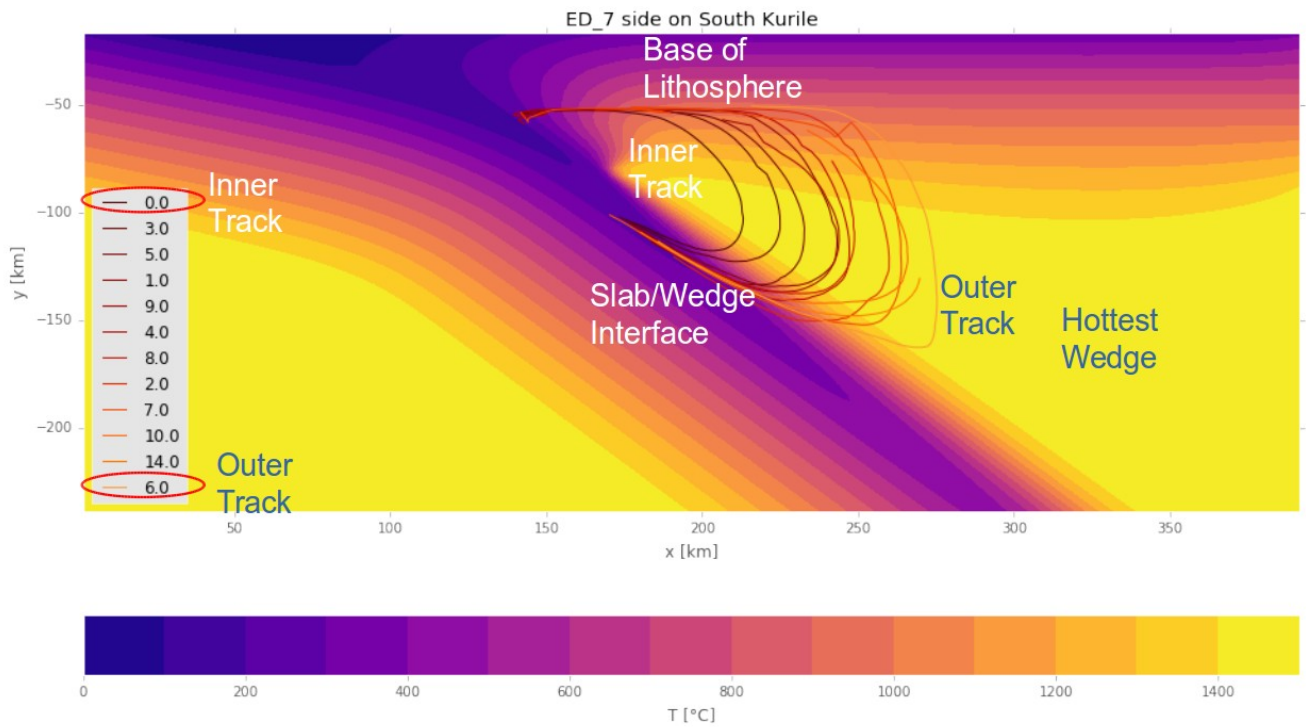


**Figure A2.1.** Laboratory diapir paths from experiment E\_7 superimposed on thermal model of South Kurile subduction zone from global compilation of subduction zone thermal models from van Keken et al. (2011). The two cases for demonstrating diapir thermal evolution are the inner and outer track from this experiment, labeled in the figure along with the SWI and LAB for orientation.

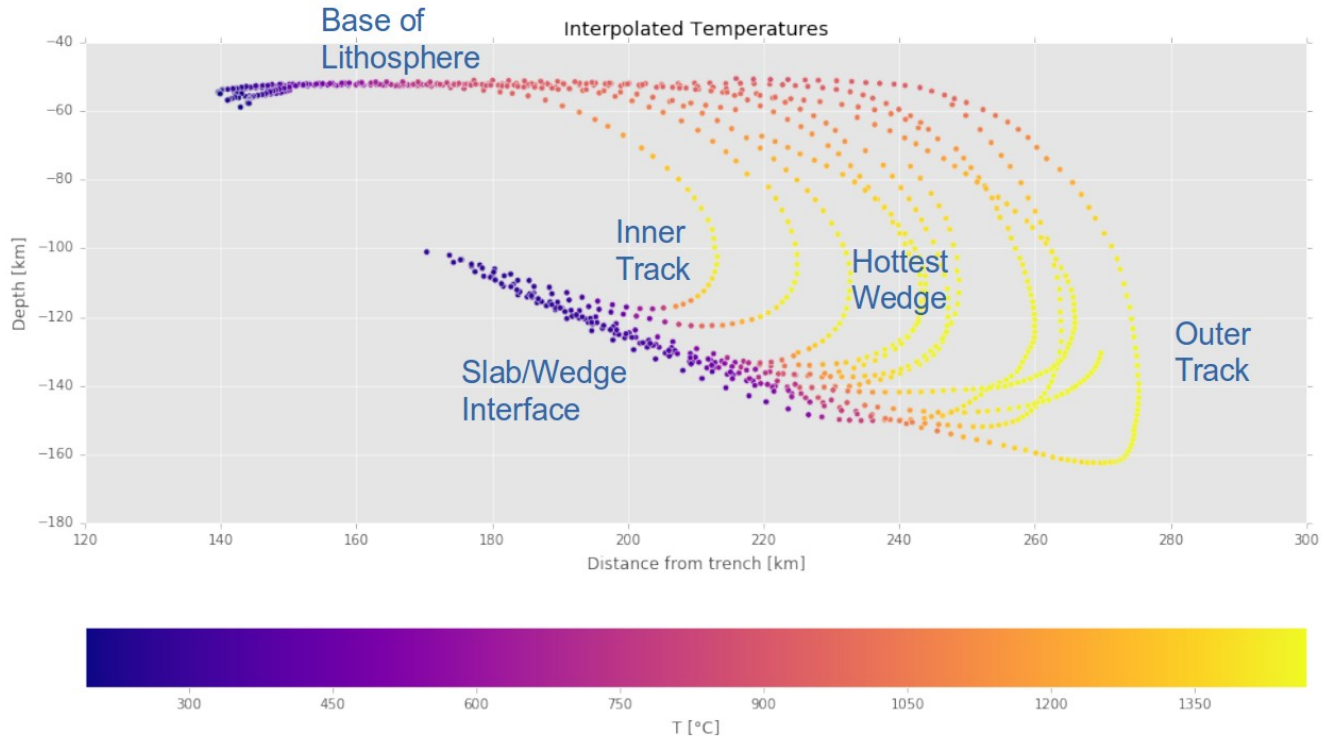


**Figure A2.2.** Interpolated temperatures from the thermal field for each recorded time-step of diapir transit used to construct temperature-time boundary forcings.

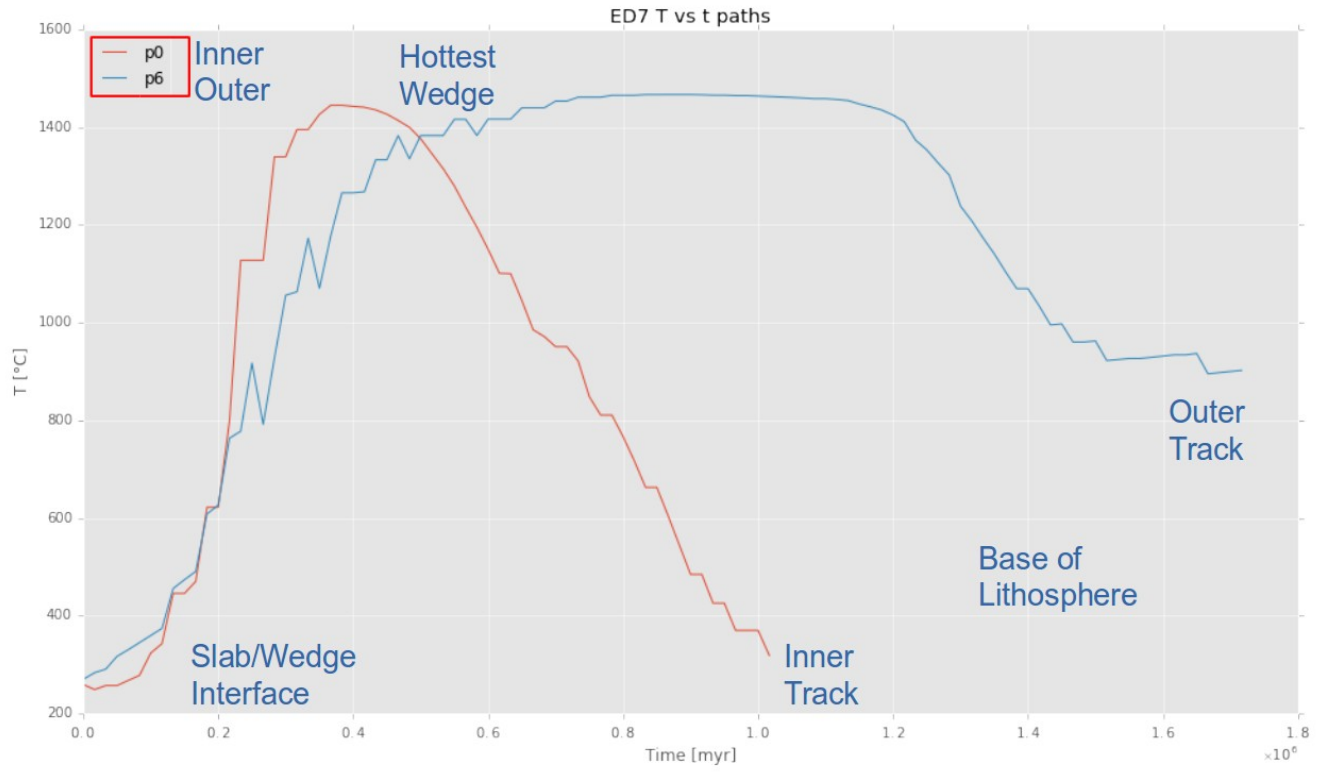


**Figure A2.3.** Temperature-time paths for the two (inner and outer) cases examined here with the SWI, LAB, and central wedge labeled for orientation.

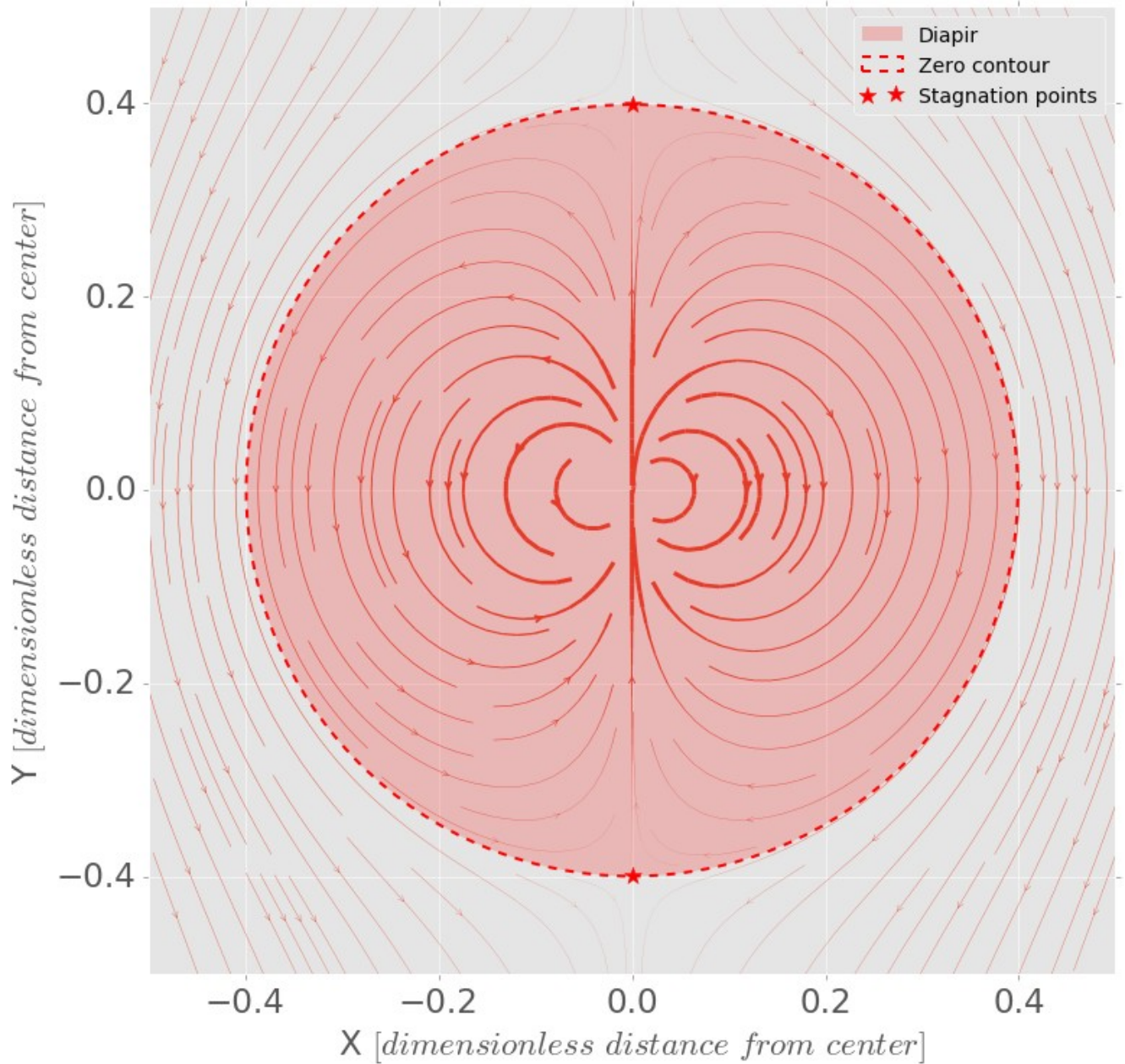


**Figure A2.4.** Velocity streamlines weighted by velocity magnitude for the flow field used in the heat model. Red shaded region is the diapir. Internal circulation within this region is set to zero for conduction only experiments.

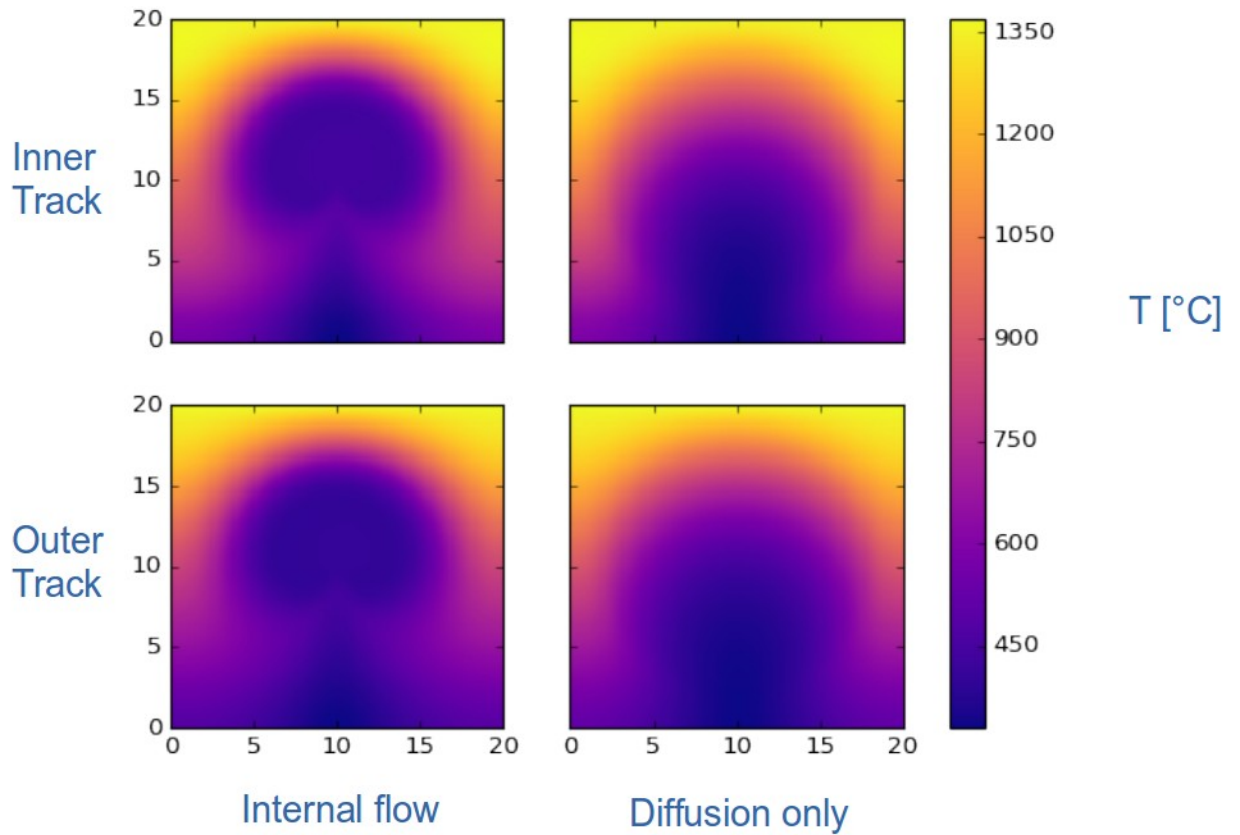


**Figure A2.5.** Model output at 500 kyr when diapirs occupy hottest part of the mantle wedge for the two cases presented. Internal circulation sweeps heat in from the edges and up the center of a diapir (left panels). When internal circulation is not applied heat is absorbed uniformly through the diapir/mantle interface.

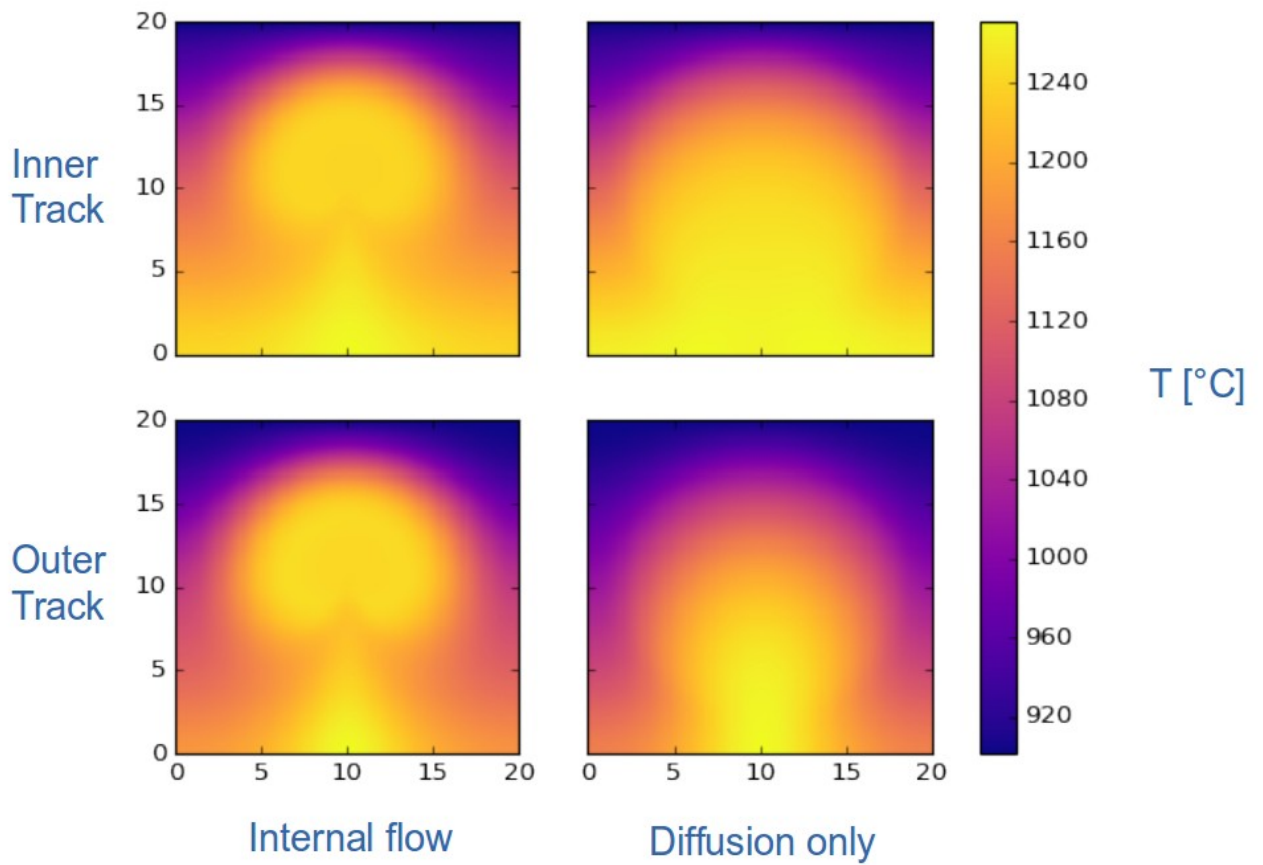


**Figure A2.6.** Model output at final time-step for the two cases presented. Internal flow case highlights plume structure generated by the internal circulation, concentrating heat at the diapir head. At this point both diapirs have internal temperatures well past the melting point of peridotite.

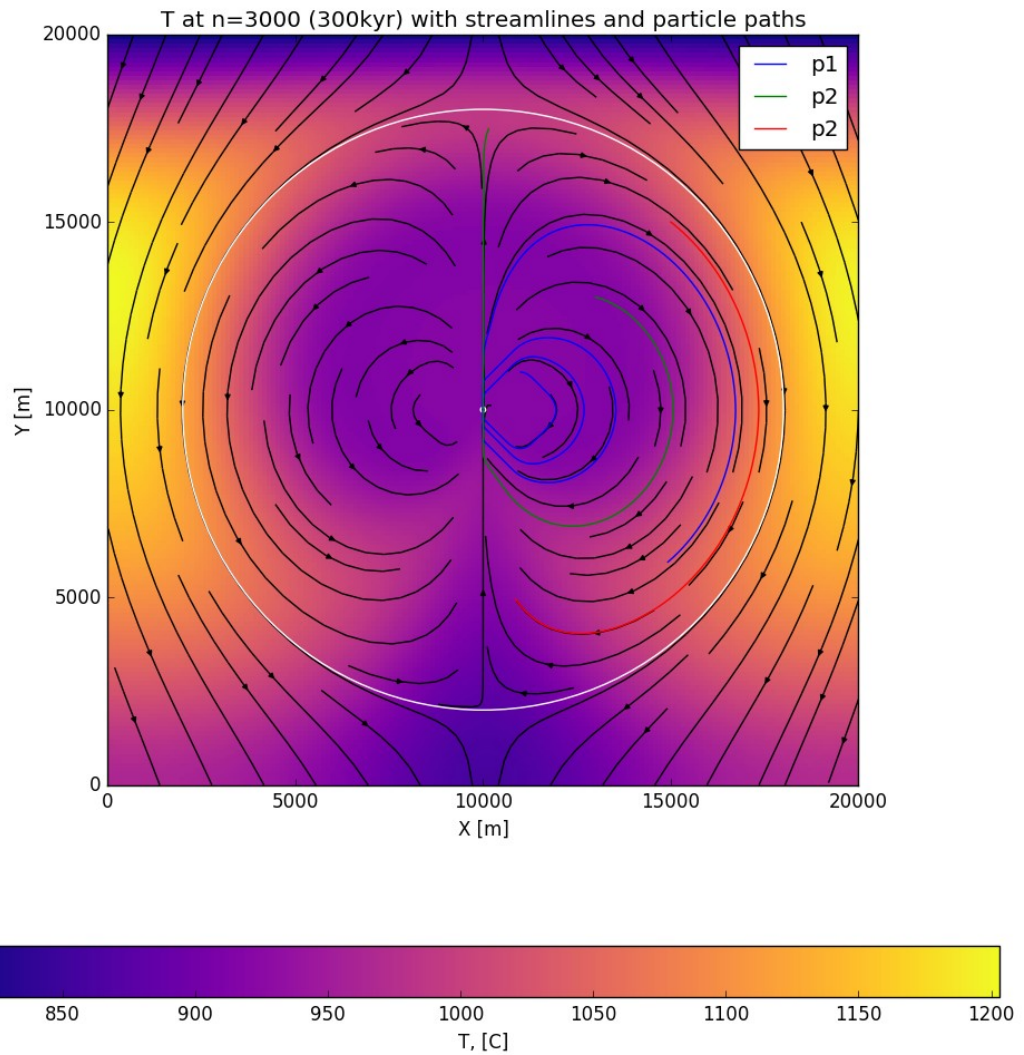


**Figure A2.7.** Diapir (outlined in white) temperature field (color) overlain with streamlines (black) and tracks of passive tracers (colored lines and legend) introduced at 3 different internal positions to track flow of heated parcels within the flow field. This image highlights the nature of the internal circulation to transport heat from the diapir/mantle interface into the diapir.

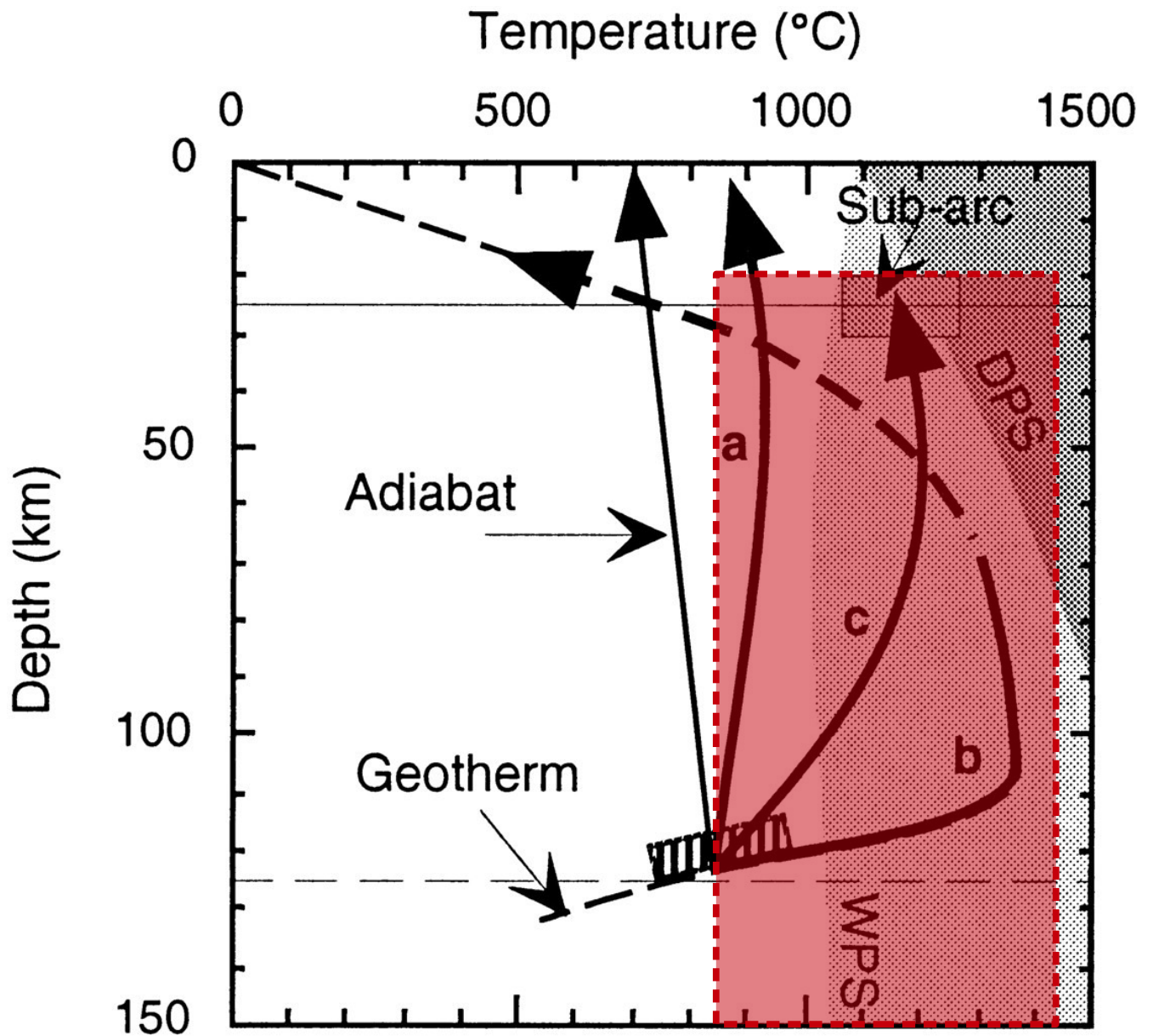


**Figure A2.8.** Figure 3 from Hall and Kincaid (2001) with their three regimes for diapiric ascent (a, b, c), and wet and dry peridotite solidi (shaded regions WPS and DPS), and diapir initial and detachment region (hatched). Red shading is the experimental observations for diapir transit paths and occupied mantle locations from this study, clearly encompassing the WPS, DPS, and sub-arc regions.